INSTITUTE OF PHYSICS PUBLISHING REPORTS ON PROGRESS IN PHYSICS

Rep. Prog. Phys. **66** (2003) 1463–1545 PII: S0034-4885(03)79242-2

Recoil-ion and electron momentum spectroscopy: reaction-microscopes

J Ullrich[1], R Moshammer[1], A Dorn[1], R Dörner[2], L Ph H Schmidt[2] and H Schmidt-Böcking[2]

[1] Max-Planck-Institut für Kernphysik, Saupfercheckweg 1, D-67119 Heidelberg, Germany
[2] Institut für Kernphysik, Universität Frankfurt, August Euler Str. 6, D-60486, Germany

Received 29 May 2003
Published 13 August 2003
Online at stacks.iop.org/RoPP/66/1463

Abstract

Recoil-ion and electron momentum spectroscopy is a rapidly developing technique that allows one to measure the vector momenta of several ions and electrons resulting from atomic or molecular fragmentation. In a unique combination, large solid angles close to 4π and superior momentum resolutions around a few per cent of an atomic unit (a.u.) are typically reached in state-of-the art machines, so-called reaction-microscopes. Evolving from recoil-ion and cold target recoil-ion momentum spectroscopy (COLTRIMS), reaction-microscopes—the 'bubble chambers of atomic physics'—mark the decisive step forward to investigate many-particle quantum-dynamics occurring when atomic and molecular systems or even surfaces and solids are exposed to time-dependent external electromagnetic fields.

This paper concentrates on just these latest technical developments and on at least four new classes of fragmentation experiments that have emerged within about the last five years. First, multi-dimensional images in momentum space brought unprecedented information on the dynamics of single-photon induced fragmentation of fixed-in-space molecules and on their structure. Second, a break-through in the investigation of high-intensity short-pulse laser induced fragmentation of atoms and molecules has been achieved by using reaction-microscopes. Third, for electron and ion-impact, the investigation of two-electron reactions has matured to a state such that the first fully differential cross sections (FDCSs) are reported. Fourth, comprehensive sets of FDCSs for single ionization of atoms by ion-impact, the most basic atomic fragmentation reaction, brought new insight, a couple of surprises and unexpected challenges to theory at keV to GeV collision energies. In addition, a brief summary on the kinematics is provided at the beginning. Finally, the rich future potential of the method is briefly envisaged.

 © 2003 IOP Publishing Ltd Printed in the UK

Contents

	Page
1. Introduction	1465
2. Kinematics: a brief summary	1467
2.1. General considerations	1467
2.2. Fast ion–atom collisions	1468
2.3. Collisions with photons	1469
3. Imaging techniques	1472
3.1. Reaction-microscopes	1472
3.1.1. Imaging of ions	1473
3.1.2. Imaging of electrons	1475
3.2. Target preparation	1478
3.2.1. Supersonic gas-jets	1478
3.2.2. Magneto optical traps (MOTRIMS)	1478
3.3. New developments	1479
4. Results	1480
4.1. Photons	1480
4.1.1. Double ionization of atoms: a brief summary	1480
4.1.2. Photoionization of fixed-in-space molecules	1483
4.2. Single and multiple ionization in intense laser fields	1487
4.2.1. Single ionization: recollision in the tunnelling regime	1488
4.2.2. Double ionization: non-sequential and sequential	1490
4.2.3. Correlated motion of electrons in the sequential and NS regimes	1492
4.2.4. Final state Coulomb repulsion and sub-threshold recollision at low intensity	1494
4.2.5. Transverse momentum exchange	1496
4.3. Electron impact ionization	1497
4.3.1. Single and double ionization	1498
4.3.2. Ionization-excitation	1504
4.3.3. Laser-assisted collisions	1504
4.4. Ion collisions	1506
4.4.1. Electron capture: dynamics and spectroscopy	1507
4.4.2. Projectile ionization: a novel approach to (e,2e)-experiments on ions	1514
4.4.3. Ionization by slow projectiles: saddle point electrons	1518
4.4.4. Ionization by fast projectiles: attosecond pulses	1521
4.4.4.1. Single ionization at small and large perturbations	1521
4.4.4.2. Double ionization at small and large perturbations	1529
4.4.4.3. Multiple ionization at large perturbations	1533
4.4.5. A short summary	1536
5. A view into the future	1536
Acknowledgments	1538
References	1538

1. Introduction

This paper tries to give an experimentally biased overview on the present state of understanding and research of a tremendously fast developing field, namely the investigation of the quantum-dynamics of fragmenting atoms and molecules. In striking contrast to the profound theoretical knowledge based on very precise experimental data that has been achieved in the investigation of the static structure of atoms and molecules, even the most simple and, thus, fundamental dynamical problems still pose severe challenges to theory.

Only three years ago, it was reported that single ionization of the hydrogen atom by electron impact, the most basic fragmentation reaction, has been solved in a mathematically consistent way (Rescigno *et al* (1999) and references therein, Bray (2002)). The method employed, a large scale partial wave expansion, made use of massively parallel supercomputers. Until now, however, it has not been demonstrated to be practicable for ion encounters or electron impact at lower or even higher energies. More recently, three-dimensional imaging of the electron emission for single ionization of helium by fast bare ionic projectiles brought to light severe discrepancies with existing theoretical descriptions in the perturbative (Schulz *et al* 2003) as well as in the non-perturbative regime (Moshammer *et al* 2001). At low collision velocities, where 'saddle point (SP) electrons' were once predicted to be emitted by Olson (1983, 1986), rich structures in the impact parameter dependent electron momentum distributions (Dörner *et al* 1996, Abdallah *et al* 1997, 1998, Afaneh *et al* 2002, Edgü-Fry *et al* 2002) are still not quantitatively explained by theory (Macek and Ovchinnikov 1998, Sidky *et al* 2000, Sidky and Lin 2001).

Until now, the more 'complicated' complete disintegration of a helium atom, the simplest many-electron system where correlation has to be taken into account (see, e.g. McGuire (1995, 1997), Ford and Reading (1988, 1990), Bronk *et al* (1998)), has been successfully described theoretically on the level of fully differential cross sections (FDCSs) only for fragmentation by single photons (for a recent review see, e.g. Briggs and Schmidt (2000)) or a fast electron impact (Kheifets *et al* 1999, Dorn *et al* 2001, 2002, 2002a). Helium double ionization in the non-perturbative regime induced by intense femtosecond laser fields or by strong, ion-generated attosecond pulses seems to be far from being solved theoretically. Multiple ionization finally, poses insurmountable problems to quantum theory on the level of FDCSs and available data must be compared to predictions of classical many-particle calculations (Schulz *et al* 2000).

In the recent past, essentially since less than a decade ago, the field was revolutionized from the experimental point of view by the invention of advanced, innovative many-particle momentum imaging and projection techniques based on large area position- and time-sensitive multi-hit electron and ion detectors. The integration of target preparation, projection techniques and detector development (Martin *et al* 1981, Sobottka and Williams 1988, Jagutzki *et al* 1998) leads to today's reaction-microscopes—the 'bubble chambers of atomic and molecular physics'—developed by Moshammer *et al* (1994, 1996) and Ullrich *et al* (1995). They enable to measure the vector momenta of several fragments (ions, electrons, molecular ions) with unprecedented large solid angles, often reaching one hundred per cent of 4π, at extreme precision: energy resolutions below 1 meV are achieved for slow electrons while ion momenta are routinely recorded at the 1 μeV level, corresponding to a temperature of a few milli-Kelvin (for the detection of low-energy electrons (<5 eV) in coincidence with recoil-ions see also Kravis *et al* (1996), Dörner *et al* (1996a, b) and Abdallah *et al* (1998)). Additional technical progress in the projectile beam preparation, namely the availability of nanosecond pulsed electron or ion beams as well as intense pulsed photon beams from third generation light sources or kilohertz, ultra-fast strong laser systems, accelerated the data-taking efficiency

decisively. Now, not only 'kinematically complete' measurements have become feasible but moreover, FDCSs can be projected out of huge data sets.

In parallel, despite of general problems, substantial progress has been achieved in the theoretical treatment of fragmenting Coulomb systems, driven by conceptual innovations as well as by the dramatic growth of computational capabilities in recent years. For example, the exterior complex scaling method mentioned above, even if not easily to be generalized, nevertheless did solve the fundamental three-particle Coulomb problem in excellent agreement with experimental results. Moreover, convergent close coupling (CCC) calculations as well as hyper-spherical R-matrix methods combined with semi-classical outgoing waves are nowadays able to reliably predict fully differential fragmentation patterns for photo double ionization of helium. Meanwhile, within the last three years, the close coupling technique has been successfully applied to describe double ionization by charged particle impact at high velocities and first successful attempts have been undertaken to implement higher-order contributions at lower energies. In addition, S-matrix approaches to describing the interaction of strong laser fields with atoms, numerical grid methods to directly integrate the Schrödinger equation, hidden crossing techniques for ion impact at low collision energies, time-dependent density functional theory to approach 'true' many-electron problems and many more have been successfully developed or applied in the recent past (see, e.g. Ullrich and Shevelko (2003)).

Historically, reaction-microscopes have emerged from 'recoil-ion momentum spectroscopy' (RIMS) and cold target recoil-ion momentum spectroscopy (COLTRIMS), continuously developed since the first recoil-ion momentum measurements by Ullrich and Schmidt-Böcking in Frankfurt (Ullrich 1987, Ullrich and Schmidt-Böcking 1987, Ullrich *et al* 1988, 1988a). Few groups world wide, the one at Kansas State University with Cocke and Ali, of Grandin and Cassimi at the GANIL in Caen, the group at the University of Frankfurt with Schmidt-Böcking, Dörner, Mergel, Schmidt, Jagutzki and others, those of Ullrich, Moshammer and Dorn at GSI, Freiburg University and now at the Max-Planck-Institute in Heidelberg made decisive contributions over 15 years to arrive at the present state of sophistication. The historical development as well as the wealth of results obtained with RIMS, the earlier recoil-ion momentum spectrometers and COLTRIMS, the high-resolution 4π-detection of the recoil-ion alone (sometimes COLTRIMS is also used as a synonym for simultaneous ion and electron momentum spectroscopy) were summarized in detail in several previous reviews on the field (Ullrich 1994, Ullrich *et al* 1997, Dörner *et al* 2000).

Therefore, and in the light of explosion-like progress within the last five years, this paper exclusively reports on the most recent experimental results and technical developments which are not or rarely covered in the previous reviews. After a brief summary of the kinematics in section 2, the latest technical developments are described in section 3. In section 4, single photon, intense laser, electron and fast ion impact induced fragmentation processes are reported within four sections. Compared with the early work with single photons at synchrotrons using reaction-microscopes, research has been strongly evolving towards molecular physics, exploring the fragmentation dynamics of fixed-in-space molecules which is described in section 4.1. Since the last review we have witnessed the first successful recoil-ion momentum measurement on intense laser induced break-up reactions of atoms performed by Moshammer *et al* (2000) and Weber *et al* (2000). Due to the rapid development in laser technology producing shorter and shorter pulses down to two optical cycles, achieving phase stabilization within the pulse envelope, producing attosecond higher harmonic photon pulses, etc, this topic progresses extremely fast. Reaction-microscopes start to play a key-role in the field and the whole section 4.2 is devoted to it. Furthermore, electron impact induced two-electron processes 'just under way' as reported by Dörner *et al* (2000) have seen a break-through since then with a set of kinematically complete (e,3e) or ionization-plus-excitation measurements and

first successful attempts to investigate laser-assisted (e,2e) reactions, described in section 4.3. Finally, as reviewed in section 4.4, even in the traditional field of RIMS, i.e. in ion–atom collision physics, tremendous progress has been achieved within the last five years: three-dimensional imaging of the electron emission in single ionization at very low (quasi-molecular regime) and quite large velocities (perturbative regime) as well as for fast highly charged ion impact (non-perturbative regime) revealed a couple of surprises testing theory in regimes that are not accessible for electron impact. Electron capture measurements have been performed in a storage ring for the first time, identifying higher order Thomas mechanisms (Schmidt *et al* 2002), as well as at an electron beam ion trap (EBIT) obtaining spectroscopic resolution for highly excited ionic states. A fully differential measurement for He double ionization was reported and compared to (e,3e) results, and projectile ionization was explored for the first time in a kinematically complete experiment. Finally, in section 5, we will briefly envisage the rich future for the physics to be explored with reaction-microscopes.

2. Kinematics: a brief summary

In this section a short summary on the non-relativistic kinematics of atomic fragmentation processes, induced by electron, ion, photon or laser-pulse impact will be provided with some emphasis given to the role of the recoiling target ion and the information which is contained in its recoil-momentum. The main purpose is to help the reader understanding the results presented in section 4 without having to search for equations in other articles. Derivations of the equations, relativistic kinematics, and a wealth of examples as well as molecular fragmentation kinematics can be found in the former reviews on the topic (Ullrich *et al* 1994, 1997, Dörner *et al* 2000) and in a recent book (Ullrich and Shevelko 2003). Throughout this paper, atomic units (a.u.) are used, where the electron mass m_e and charge e as well as Planck's constant $\hbar = h/2\pi$ are set to unity ($m_e \equiv e \equiv \hbar \equiv 1$) and the velocity of light $c = 137$.

2.1. General considerations

The general scheme of an impact induced fragmentation reaction is sketched in figure 1: a projectile with an incoming momentum $\vec{P}_P^i = (P_{Px}^i, P_{Py}^i, P_{Pz}^i) = (0, 0, P_{P\|}^i)$ (laboratory frame) is scattered to a final state $\vec{P}_P^f = (P_{Px}^f, P_{Py}^f, P_{Pz}^f)$ (for photon absorption $\vec{P}_P^f = 0$) transferring a momentum $\vec{q} = -\Delta\vec{P}_P = \vec{P}_P^i - \vec{P}_P^f$ to the target, where $\Delta\vec{P}_P$ is the momentum change of the projectile. All charged particle induced reactions are symmetric with respect to the projectile propagation direction along the z-axis (azimuthal symmetry) making it convenient to introduce the transverse and longitudinal momenta $(P_\perp, P_\|) = (\sqrt{(P_x + P_y)^2}, P_z)$ as well as

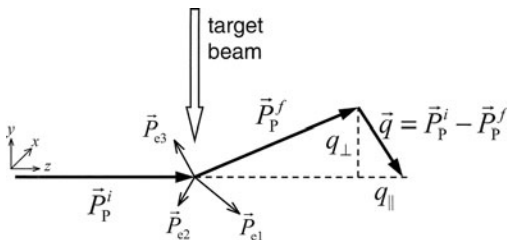

Figure 1. Illustration of the momenta occurring in atomic fragmentation by projectile impact (see text) (from Ullrich and Shevelko (2003)).

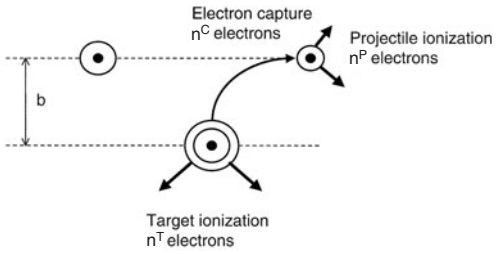

Figure 2. Different reaction channels that can occur in an ion–atom collision (see text) (from Ullrich and Shevelko (2003)).

the momentum transfer $\vec{q} = (q_\perp, q_\parallel) = (q_\perp, \Delta E_\mathrm{p}/v_\mathrm{p})$, respectively ($\Delta E_\mathrm{p}$, v_p: energy change and velocity of the projectile; $v_\mathrm{p} = c$ for photon impact).

A possible result of the energy and momentum transfer is the fragmentation of the target atom into n^T electrons with momenta $\vec{P}^\mathrm{f}_{ei}$ (n^T-fold ionization) and one recoiling (excited) target ion with momentum $\vec{P}^\mathrm{f}_\mathrm{R} = (P^\mathrm{f}_{\mathrm{R}x}, P^\mathrm{f}_{\mathrm{R}y}, P^\mathrm{f}_{\mathrm{R}z}) = (P^\mathrm{f}_{\mathrm{R}\perp}, P^\mathrm{f}_{\mathrm{R}\parallel})$. As in the figure, the index 'f' for 'final' is often omitted later on for the target fragment momenta, since we have no measurable initial ones that would have to be distinguished. The total momentum of the target in the initial state $\vec{P}^\mathrm{i}_\mathrm{R} + \sum \vec{P}^\mathrm{i}_{ei} = \vec{P}^\mathrm{i}_\mathrm{atom}$ is zero or has a well-defined value in the ideal case and cooling techniques are applied (see section 3) to approach this limit. For ion impact as is sketched in figure 2, one often defines an impact parameter b and, in addition, the transfer of n^C electrons from the target to the projectile (electron capture) as well as projectile ionization (electron loss) becomes possible, where n^P electrons are released from an ionic projectile. Certainly, all these reaction channels might occur simultaneously within the same collision. As a result, there are N fragments in the final state with $N = n^\mathrm{T}+1$ for photon, $N = n^\mathrm{T}+2$ for electron and $N = n^\mathrm{T}+n^\mathrm{P}+2$ for ion impact and a total of $n = n^\mathrm{T}+n^\mathrm{P}$ electrons released to the continuum. Due to momentum and energy conservation

$$\Delta E_\mathrm{p} = E^\mathrm{i}_\mathrm{P} - E^\mathrm{f}_\mathrm{P} = Q + E^\mathrm{f}_\mathrm{R} + \sum_{i=1}^{n} E^\mathrm{f}_{ei}, \tag{1}$$

the collision kinematics is fully determined if $3N - 3$ linear independent (scalar) momentum components are measured in kinematically complete experiments (neglecting the spin). Then, FDCSs can be extracted. In equation (1), ΔE_p is the energy change of the projectile, E^f_R and E^f_{ei} are the final energies of the recoiling target ion and of the ith emitted electron, respectively and $Q = \sum E^\mathrm{f}_{ei_\mathrm{b}} - E^\mathrm{i}_{ei_\mathrm{b}}$ is the inelasticity of the reaction, i.e. the change in the total internal energies of the projectile and of the target ($E^\mathrm{i,f}_{ei_\mathrm{b}} < 0$: binding energy of the ith electron in the initial and final state, respectively).

Whereas the kinematical equations usually cannot be further simplified for electron induced reactions, considerable approximations can be made for fast ion collisions as well as for photon absorption and Compton scattering, such that physical insight is directly obtained from the recoil-ion or electron momentum distributions, as illustrated below.

2.2. Fast ion–atom collisions

For the overwhelming part of all atomic reactions in ion–atom collisions only little momentum, energy and mass compared to the initial momentum ($\vec{P}^\mathrm{i}_\mathrm{P}$), energy ($E^\mathrm{i}_\mathrm{P}$) and mass ($M^\mathrm{i}_\mathrm{P}$) of the incoming projectile is transferred during the encounter. This is true even for small projectile masses (protons and in many cases even for electrons) as well as for comparably violent

collisions, where the target atom is multiply ionized in an encounter with a highly charged ion. Under these conditions the longitudinal and transverse momentum balances are decoupled, contain different information on the collision and can be calculated separately on the basis of energy and momentum conservation.

Since the recoil-ion momentum is always measured in the here-described experiments and since it contains a wealth of information, yielding physical insight even for many-electron processes if the electrons are not detected, momentum balances are traditionally expressed within the recoil-ion perspective. Transversally one obtains (non-relativistic):

$$P^{\mathrm{f}}_{\mathrm{R}\perp} = -\left(P^{\mathrm{f}}_{\mathrm{P}\perp} + \sum_{i=1}^{n} P^{\mathrm{f}}_{\mathrm{e}i\perp}\right) = q_{\perp} - \sum_{i=1}^{n} P^{\mathrm{f}}_{\mathrm{e}i\perp}. \tag{2}$$

For pure electron capture (see, e.g. Ali *et al* (1992), Mergel *et al* (1995), Fischer *et al* (2002)) or for reactions where $\sum_{i=1}^{n} P^{\mathrm{f}}_{\mathrm{e}i\perp}$ is small compared to the heavy particle momenta (i.e. at small b or $E^{\mathrm{i}}_{\mathrm{P}}$) $P^{\mathrm{f}}_{\mathrm{R}\perp} \approx -P^{\mathrm{f}}_{\mathrm{P}\perp}$ and the recoil-ion momentum measurement alone yields direct information on the projectile deflection $\vartheta_{\mathrm{P}} \approx P^{\mathrm{f}}_{\mathrm{P}\perp}/P^{\mathrm{i}}_{\mathrm{P}}$ (see, e.g. Ullrich *et al* (1988a, 1989), Gensmantel *et al* (1992), Dörner *et al* (1996a)). If reaction-microscopes are used, the projectile scattering can be investigated in ionization or transfer ionization (TI) reactions as well, obtaining detailed information on the many-particle transverse momentum balance. Unprecedented micro or even nano-radian ϑ_{P}-resolution is achieved (see, e.g. Moshammer *et al* (1994, 1996a, 2001), Fischer *et al* (2003b)).

Expressing the total longitudinal recoil-ion momentum in terms of three different contributions, namely electron capture, loss and ionization one obtains:

$$P^{\mathrm{f}}_{\mathrm{R}\parallel} = P^{\mathrm{cap}}_{\mathrm{R}\parallel} + P^{\mathrm{loss}}_{\mathrm{R}\parallel} + P^{\mathrm{ion}}_{\mathrm{R}\parallel} \tag{3}$$

with

$$P^{\mathrm{cap}}_{\mathrm{R}\parallel} = \frac{Q}{v_{\mathrm{P}}} - n^{\mathrm{C}} \cdot \frac{v_{\mathrm{P}}}{2}, \tag{4}$$

$$P^{\mathrm{loss}}_{\mathrm{R}\parallel} = \frac{Q}{v_{\mathrm{P}}} + \sum_{i=1}^{n^{\mathrm{P}}} \frac{(E^{\mathrm{f}}_{\mathrm{e}i})_{\mathrm{PF}}}{v_{\mathrm{P}}}, \tag{5}$$

$$P^{\mathrm{ion}}_{\mathrm{R}\parallel} = \frac{Q}{v_{\mathrm{P}}} - \sum_{i=1}^{n^{\mathrm{T}}} P^{\mathrm{f}}_{\mathrm{e}i\parallel} + \sum_{i=1}^{n^{\mathrm{T}}} \frac{E^{\mathrm{f}}_{\mathrm{e}i}}{v_{\mathrm{P}}}. \tag{6}$$

Energies of electrons released from the projectile (5) are measured in the projectile frame (PF). Thus, apart from the many-particle momentum balance along the beam propagation, the longitudinal recoil-ion momentum contains information on the inelasticity of the reaction. Recently, this has been exploited to obtain structural information about the binding energies of high-lying singly or doubly excited electronic sates by studying single electron capture from He in collisions with Ne^{7+} at $v_{\mathrm{P}} = 0.35$ a.u. reaching a few meV energy resolution as illustrated in figure 3 (e.g. Fischer *et al* (2002) and references therein for earlier measurements).

2.3. Collisions with photons

A photon with the energy E_{γ}, absorbed by an atom essentially deposits all its energy into the target electron shell. If the photon momentum $P_{\gamma} = E_{\gamma}/c$ is small compared to the momenta of the atomic fragments, which is true as long as the total inelastic energy transfer is small

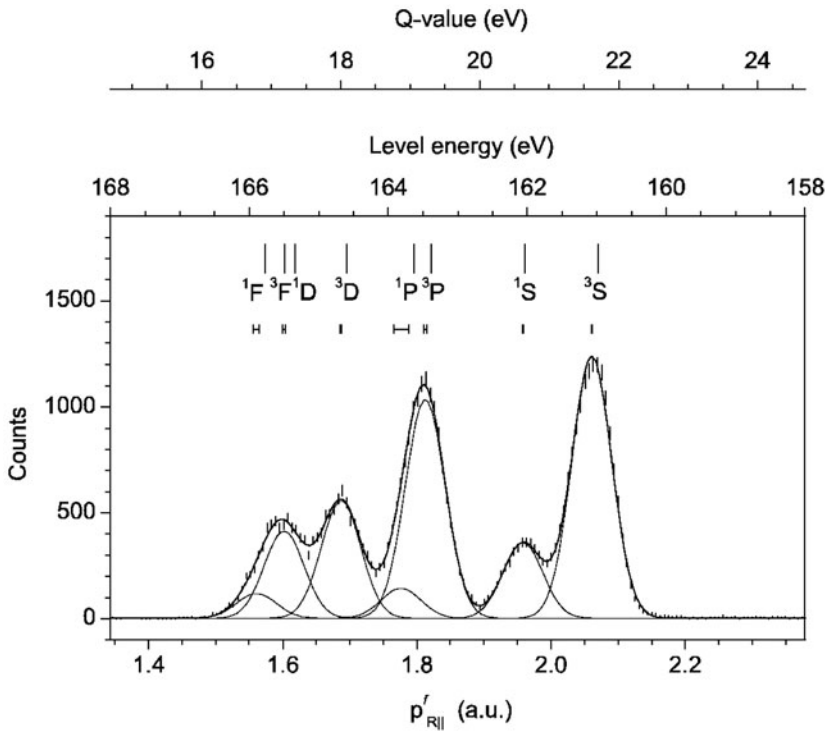

Figure 3. The Q-value or longitudinal recoil-ion momentum spectrum for Ne^{6+} measured for single capture in Ne^{7+} on He collisions at $v_p = 0.35$ a.u.. The resolution is 0.52 eV. The scale of the energy levels, counted from the ground state of Ne^{6+} is also shown together with the identification of the $2s4l\,^{1,3}L$ singlet and triplet states (L = S, P, D and F). Upper marks: multi-configuration Hartree–Fock calculations (Buchet-Poulizak *et al* 2001). Lower marks with error bars: experimental result by Fischer *et al* (2002).

compared to the sum-energy of emitted photo-electrons, then one obtains for single ionization:

$$|\vec{P}^{\,f}_R|^2 = (P^f_{Rx})^2 + (P^f_{Ry})^2 + (P^f_{Rz})^2 = R, \tag{7}$$

$$|\vec{P}^{\,f}_e|^2 = (P^f_{ex})^2 + (P^f_{ey})^2 + (P^f_{ez})^2 = R. \tag{8}$$

In this approximation, electron and recoil-ion emerge into opposite directions compensating their momenta with their momentum vectors ending on a sphere with radius

$$R = 2\frac{m_e M_R}{m_e + m_R}(E_\gamma - Q). \tag{9}$$

The recoil-ion energy is m_e/M_R times smaller than the electron energy and, thus, negligible in most cases. Taking the photon momentum into account results in a shift of the centre of the sphere by $P_\gamma = E_\gamma/c$ along the photon propagation direction for the recoil-ion and of $(m_e/M_R) \cdot (E_\gamma/c)$ for the electron, respectively. Moreover, the radii of the spheres shrink.

In figure 4, momentum distributions in the (x, y)-plane are shown for single ionization of helium by the absorption of one photon (a), for multi-photon above-threshold ionization (ATI) of argon (b), for tunnelling ionization of Ne in an intense photon pulse (c) and for Compton scattering (d). The circular shape is clearly visible in the recoil-ion momentum distribution for the absorption of an 80 eV photon by He (figure 4(a)), with different inner

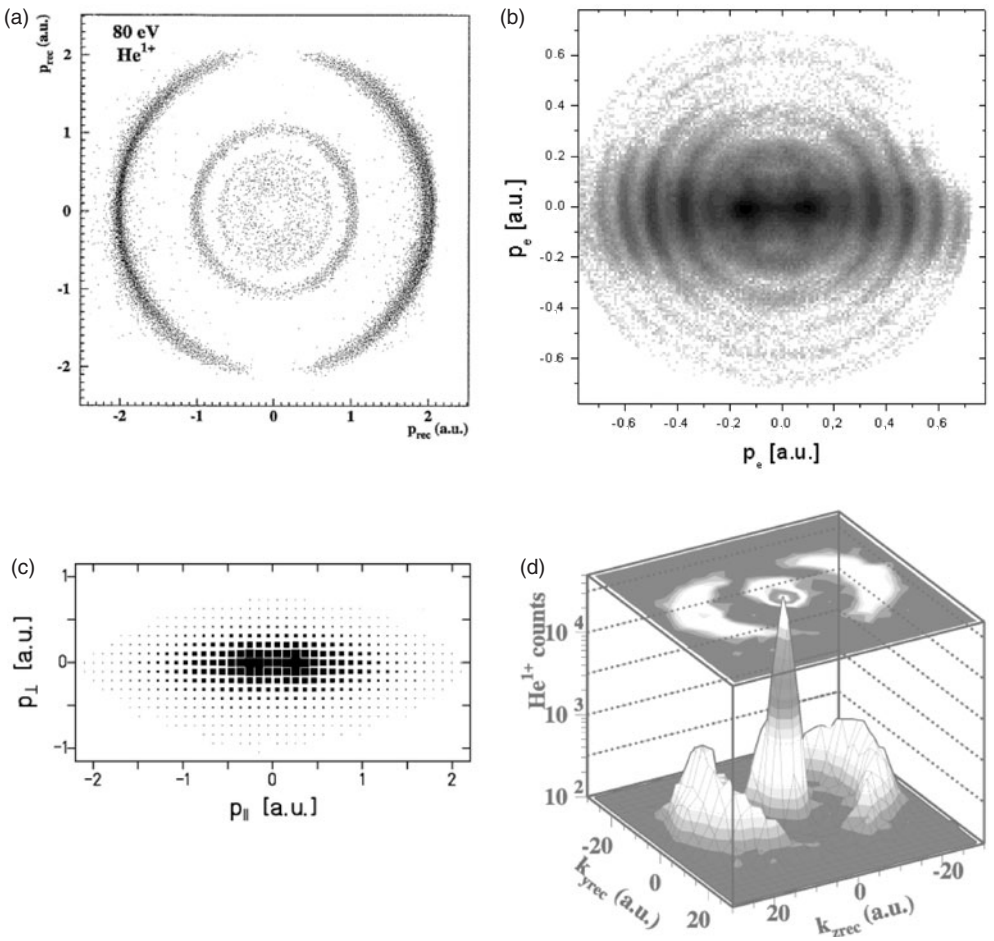

Figure 4. Momentum distributions for single ionization in collisions with photons propagating along the z-axis for linear polarization along the x-direction. (*a*) Single ionization of He by absorption of single 80 eV photons. In the figure, the recoil-ion momentum distributions are integrated over $P^{\mathrm{f}}_{\mathrm{R}z} = 0 \pm 0.1$ a.u. and $p_{\mathrm{rec}} = P^{\mathrm{f}}_{\mathrm{R}}$. From Dörner *et al* (1997). (*b*) Electron momentum distribution for multi-photon single ionization of Ar by 25 fs laser pulses at 780 nm and an intensity of a few $10^{13}\,\mathrm{W\,cm^{-2}}$. The momentum distributions represent a cut along the z-direction of $P^{\mathrm{f}}_{\mathrm{R}z} = 0 \pm 0.1$ a.u.. (*c*) Recoil-ion momentum distribution for tunnelling single ionization of Ne interacting with $1 \times 10^{15}\,\mathrm{W\,cm^{-2}}$, 25 fs laser pulses at 780 nm. All events along z are projected. From Moshammer *et al* (2003a). (*d*) Recoil-ion momentum distribution created by 7 keV linear polarized photon impact, outer rim: photo absorption, narrow peak: Compton scattering ($k_{z\mathrm{rec}} = P^{\mathrm{f}}_{\mathrm{R}x}$, $k_{y\mathrm{rec}} = P^{\mathrm{f}}_{\mathrm{R}y}$) (from Spielberger *et al* (1995)).

circles due to the simultaneous excitation of the remaining He^+ electron to various n-levels. For the outer circle where the He^+ ions are in their ground state (GS), one observes a clean dipolar intensity distribution with its maximum along the horizontal polarization direction. For multi-photon absorption (figure 4(*b*)) several rings are found in the electron momentum distribution, separated by the recoil-momentum of one individual laser photon. Close to zero momentum the circular structure is washed out due to the distortion of the atomic levels as well as of the continuum by the strong laser field. Moreover, only small parts of the circles are actually populated with a distinct maximum along the horizontal polarization direction and a rapid decrease towards larger angles, indicating that considerable momentum can be

transferred if few photons are involved. If the field becomes very strong (10^{15} W cm^{-2}), the circular structure disappears completely (figure 4(*c*)). Now, the recoil-ion momentum pattern is strongly extended along the polarization axis. The distribution obtained along the x- and y-directions can be well understood within a classical field perspective in terms of tunnelling of the active electron through the barrier formed by the modification of the atomic potential in the oscillating laser field (for details see section 4.2).

For Compton scattering finally, which dominates the photo absorption cross section at large E_γ, the recoil-ion essentially acts as a spectator (inner peak in figure 4(*d*)). Energy and momentum conservation is fulfilled by the photon and the electron alone, leaving the ion just with the momentum of the removed electron, i.e. with the bound-state momentum distribution, namely the 'Compton profile' (see, e.g. Samson *et al* (1994), Spielberger *et al* (1995, 1996), Krässig *et al* (1999)).

3. Imaging techniques

The rapid and still ongoing development of RIMS during the last ten years can undoubtedly be viewed as an experimental break-through for the investigation of any kind of atomic reactions. Whenever atoms or simple molecules interact with electrons, ions or photons and charged target fragments emerge the concept of high-resolution recoil-ion momentum measurements resulted in additional and complementary information compared to the traditional methods. State of the art high-resolution recoil-ion momentum spectrometers evolved through numerous technical developments like, e.g. the implementation of cold supersonic gas-jet targets, the use of well defined electric extraction fields for recoil-ions as well as for electrons and the rapid progress in charged particle detection techniques. Among them the use of supersonic jets to produce well localized and internally cold targets (COLTRIMS) can be viewed as the most important ingredient. They allowed recoil-ion momentum resolutions far below 1 a.u. which would be impossible with room temperature targets (the momentum spread of room temperature helium is about 3.7 a.u.). Another decisive development was the invention of completely novel and extremely efficient electron imaging concepts. In combination with COLTRIMS these so-called 'reaction-microscopes' enabled the projection of recoil-ions and electrons in coincidence and opened up a whole area for kinematically complete atomic reaction studies. Combined with advanced multi-particle detection techniques kinematically complete studies of atomic collision reactions with up to five outgoing particles became feasible (triple ionization of Ne in collisions with heavy ions, Schulz *et al* (2000)). Here, we briefly discuss the working principle of these modern spectrometers leaving out a detailed historical overview (for this the reader is referred to Cocke *et al* (1991), Ullrich *et al* (1994, 1997), Dörner *et al* (2000)).

3.1. Reaction-microscopes

The general design of a reaction-microscope is shown schematically in figure 5. A well collimated beam of cold atoms or molecules, usually provided by a cooled supersonic gas jet, is crossed with a projectile beam of any kind. The cross-over defines the effective target volume which is placed in a region where a weak electrostatic field is applied for extraction of charged target fragments. On either side of this acceleration region a field-free drift path and a large area position sensitive detector is located to register the recoiling target ions and electrons, respectively. The drift path lengths should be adapted to the acceleration lengths to avoid that different starting positions (potentials) in the acceleration field result in different

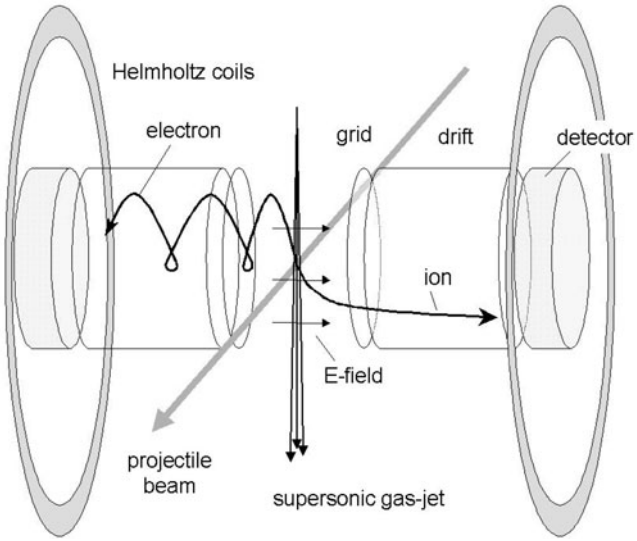

Figure 5. Reaction-microscope (from Moshammer *et al* (2003b)).

flight-times (time-focusing condition). Electrons and ions are detected after post acceleration by channel plate detectors equipped with structured anodes for position decoding.

From most atomic reactions, the recoil-ions emerge with kinetic energies of some meV or below and extraction fields of a few $\mathrm{V\,cm^{-1}}$ are generally sufficiently high to achieve a 4π collection efficiency (with typical detector sizes). However, emitted electrons have usually considerably larger kinetic energies making it much harder to collect them. Most of them simply miss the detector. In order to achieve a high acceptance together with a good resolution for both electrons and recoil-ions in coincidence, a weak homogenous magnetic field (generated by a pair of large Helmholtz coils) is superimposed along the spectrometer axis effectively confining the electron motion in space. Then, with basically two parameters, the magnetic field strength and the extraction voltage, the resolution and the acceptance both become adjustable over a large range in the electron and ion branch individually. It is essentially this zooming option which makes reaction-microscopes extremely versatile and which considerably extended the range of applications for coincident electron–ion imaging.

3.1.1. Imaging of ions. Recoil-ions produced in the target zone are accelerated by the electric extraction field onto the position sensitive detector. Then, from the obtained position and time-of-flight (TOF) information of each detected ion, the trajectory can be reconstructed and the initial momentum vector can be calculated unambiguously. The TOF has to be measured with respect to a trigger signal which uniquely defines the time of interaction of a projectile with a single target atom. To do so either a pulsed beam of projectiles (synchrotron-radiation, pulsed lasers, bunched electron or ion-beams) has to be used or single projectiles of a continuous beam have to be detected with a time-sensitive detector, e.g. after the collision. The TOF spectrum contains two important pieces of information. First, different ion species can be distinguished because they appear as well separated peaks in the TOF spectrum due to the dependence of the flight-time on the mass to charge ratio. Second, the shapes of these individual peaks contain information about the initial ion momentum. To illustrate this, we assume that, for a given spectrometer, ions of a certain mass and charge but with zero initial momentum appear after a flight-time t_0 at the detector. Then, for those ions which emerge with an initial velocity vector

pointing toward the detector the measured TOF will be shorter than t_0 and vice versa. For a spectrometer with a homogenous extraction field it is possible to assign to each channel in the TOF spectrum the corresponding recoil-ion momentum parallel to the spectrometer axis of ($P_{R\|}$ in a.u., qU in eV, a in cm and t, t_0 in ns)

$$P_{R\|} = 8.042 \times 10^{-3} \cdot \frac{qU}{a} \cdot (t_0 - t), \tag{10}$$

where t is the actual TOF and a is the distance over which the ion of charge q is accelerated to an energy of qU. This relation is independent of the particle mass and it is valid for ions and electrons as long as their initial kinetic energy is small compared to qU. Usually, this is very well fulfilled for recoil-ions from atomic reactions but not for those resulting from molecular fragmentation. Moreover, only the knowledge about the electric field strength U/a at the source point is required to calculate the ion parallel momentum and no further information about the overall geometry of the spectrometer is needed. Thus, with a time resolution of 1 ns in the TOF measurement under otherwise ideal conditions a momentum resolution below 0.01 a.u. is achievable when a field of 1 V cm^{-1} is used for extraction. An example of a TOF spectrum is shown in figure 6 for ionization of Ar atoms with strong 25 fs laser pulses at an intensity of several 10^{13} W cm^{-2}. The laser polarization direction was chosen to be parallel to the spectrometer axis. The inset of figure 6 shows the magnified Ar^{1+} peak with distinct individual peaks corresponding to the absorption of a certain number of 1.5 eV photons above the ionization threshold. Basically, the recoil-ion compensates the momentum of the emitted electron, the kinetic energy of which is given by the total number of absorbed photons minus the ionization potential. In this case, structures in the ion momentum distribution (obtained after conversion of the TOF spectrum using (10)) in the order of 0.1 a.u. are clearly resolved. This corresponds to a kinetic energy of the Ar^{1+} ions of less than 2 μeV.

The momentum components perpendicular to the spectrometer axis can be determined from the position of impact on the ion detector. For a point like source of ions and for

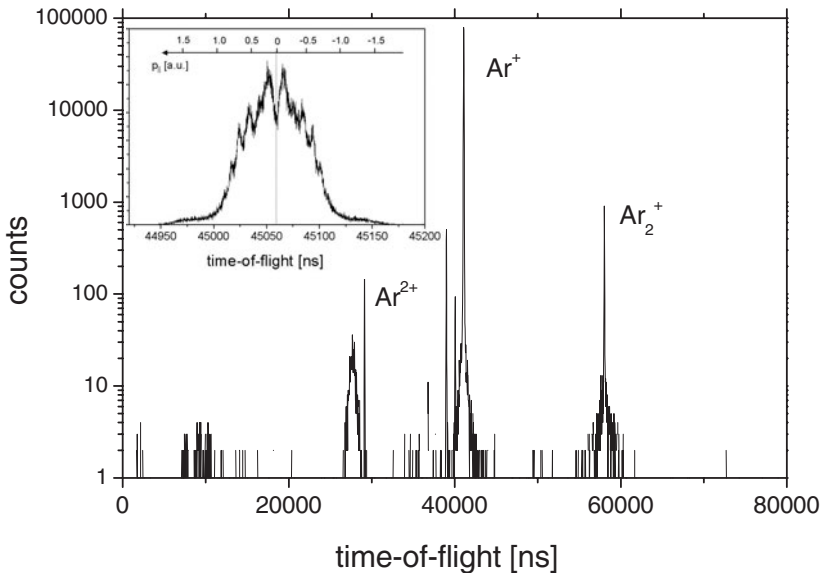

Figure 6. TOF spectrum for ionization of Ar with 25 fs laser pulses at an intensity of some 10^{13} W cm^{-2}. The inset shows a blow up of the Ar^{1+} TOF-peak (see text).

well defined acceleration (homogenous electric field) and ion drift regions the transverse ion momentum vector is given by ($P_{R\perp}$ in a.u., m in amu, qU in eV, distances in cm)

$$\vec{P}_{R\perp} = 11.6 \cdot \frac{\vec{r}}{2a+d} \cdot \sqrt{qU \cdot m}, \tag{11}$$

where r is the radial displacement on the detector with respect to the position where ions with zero initial momentum hit the detector. The distances a and d denote the acceleration and drift length, respectively. Again, this approximation is very well justified as long as the width Δt of the ion TOF-peak is much smaller than the mean flight-time, or in other words, as long as the kinetic energy gain due to the extraction is significantly larger than the initial recoil-ion energy. The achievable momentum resolution depends on the position resolution of the detector and on the extension of the target zone. In many realistic situations the latter is dominating. For a time-focusing spectrometer with an extraction voltage of 10 V applied over 10 cm a target extension of 1 mm causes a transverse momentum uncertainty of $\Delta P_{R\perp} = 0.18$ a.u. for He-ions. However, the achievable resolution can be increased significantly either by lowering the extraction voltage or by increasing the spectrometer size as long as the resulting reduction in the transverse momentum acceptance is no matter of concern.

In order to eliminate the influence of the target extension on the transverse momentum resolution, spectrometers with the so-called position-focusing have been developed (see, e.g. Abdallah *et al* (1998), Dörner *et al* (1998)). They focus ions starting at different positions onto a single spot on the detector while the displacement on the detector is still proportional to the initial momentum. To achieve position-focusing a weak electrostatic lens is implemented into the acceleration region, preferably as close as possible to the reaction-zone. Thus, the resolution is no longer limited by the source extension but by the imaging properties of the spectrometer. This concept has been used mainly to study electron capture reactions in ion–atom collisions as well as for most photon impact studies where a high-resolution is decisive.

3.1.2. Imaging of electrons. The conceptually most obvious scheme for coincident imaging of electrons and ions is to place a second position sensitive detector opposite to the ion detector. In fact, this concept has been used to study low-energy electron emission in ion–atom collisions (Dörner *et al* 1996a, Edgü-Fry *et al* 2002) and photoionization close to threshold (Dörner *et al* 1996b). For many applications, however, the accepted maximum electron energy in the transverse direction is too small (for early work on the two-dimensional imaging of photoelectrons alone, using large extraction fields, see Helm *et al* (1993)).

To circumvent this limitation and to increase the electron energy acceptance maintaining at the same time the full resolution in the recoil-ion branch a solenoidal magnetic field is superimposed parallel to the electric field (Moshammer *et al* 1996). It acts over the whole flight-path and forces electrons onto spiral trajectories from the reaction volume to the detector. Again, the position and TOF information allows an unambiguous reconstruction of the initial electron momentum vector. The longitudinal motion is not changed and the same considerations as those for the recoils can be applied to reconstruct the longitudinal momentum from the electron TOF, however, because of their high kinetic energies, no approximate equations should be used. In the transverse direction (perpendicular to the field axis), the electrons travel along a circle with radius $R = P_{e\perp}/(qB)$ where the time T for one turn is given by the inverse of the cyclotron frequency $\omega = (qB)/m_e = 2\pi/T$ (B: magnetic field strength, m_e and q: electron mass and charge, respectively). In useful units these equations are

$$\omega = 9.65 \times 10^{-6} \cdot \frac{qB}{m_e} \qquad \text{and} \qquad R = 12.39 \cdot \frac{P_{e\perp}}{qB} \tag{12}$$

with ω in ns^{-1}, q and $P_{e\perp}$ in a.u., B in Gauss, m_e in amu. With a magnetic field of only 10 Gauss all trajectories of electrons with energies up to 100 eV are confined to a cylinder with a radius of 3.3 cm, independent of the electric field strength and independent of the spectrometer geometry. Hence, a detector with 8 cm diameter is sufficient to achieve a 4π collection efficiency for electrons with energies of more than 100 eV. Under these conditions the revolution time for electrons is 35 ns, i.e. in the range of, or even smaller than, typical electron flight-times. The cyclotron time for ions on the other hand of more than 250 μs for He under the above conditions is usually much longer than their flight-times, indicating that the ion trajectories are only weakly affected by the magnetic field. It basically results in a slight rotation of the ion image on the recoil-detector, which is easily compensated by a corresponding back-rotation of the whole ion position distribution. In conclusion, by changing the magnetic field strength the accepted maximum transverse momentum of electrons is adjustable without noticeably affecting the recoil-ion imaging.

To calculate the electron transverse momentum vector, both pieces of information, position and TOF, are required. To illustrate this, we consider the projection of an electron trajectory onto the electron detector surface, i.e. onto a plane perpendicular to the magnetic field axis (figure 7). An electron, which is emitted at the origin (point A) with a transverse momentum $P_{e\perp}$ under a certain angle φ with respect to the positive x-axis travels on a spiral trajectory, corresponding to a circle (radius R) in the transverse plane, before it hits the detector at the point B with a certain displacement r from the centre. The radius R is a direct measure of $P_{e\perp}$ (12) while the arc-angle ωt depends only on the electron TOF. From simple geometrical considerations (figure 7) one gets

$$R = \frac{r}{2|\sin(\omega t/2)|}. \tag{13}$$

Thus, the magnitude of the transverse momentum $P_{e\perp}$ can be calculated from the position of detection, (r, ϑ) in cylindrical coordinates, and the electron TOF t using (12) and (13). With

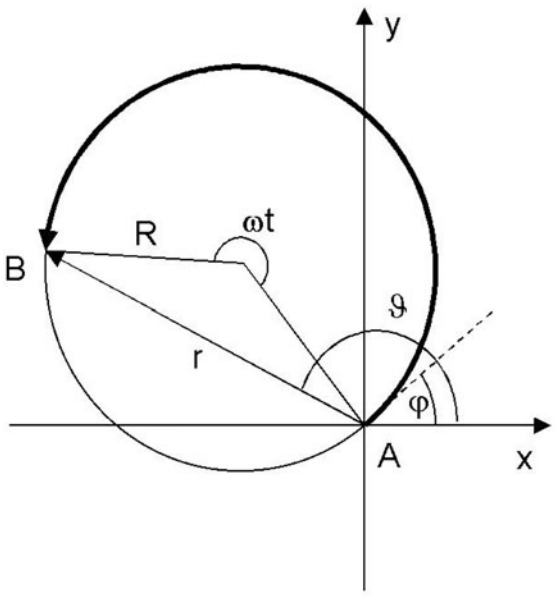

Figure 7. Projection of an electron trajectory onto a plane perpendicular to the magnetic field (view along the magnetic field lines) (from Moshammer *et al* (2003b)).

the emission angle φ, which is given by

$$\varphi = \vartheta - \frac{\omega t}{2}, \tag{14}$$

the transverse momentum vector is determined.

What happens if the electron performs more than one complete turn? In this case ωt has to be replaced by $\omega t - N \cdot 2\pi$ where N (number of full turns) is the next lowest integer of the ratio $(\omega t)/(2\pi)$. Still, the assignment of measured quantities and initial momentum is unique, as long as the denominator in (13) is larger than zero. The only prerequisite for reconstruction is the knowledge of the magnetic field strength and direction, respectively.

Whenever electrons perform exactly N complete turns they hit the detector at the origin (point A in figure 7) independent of their initial transverse momentum or, in other words, all electrons with flight-times equal to a multiple integer of T (the inverse cyclotron frequency) are focused onto the same spot on the detector and no momentum information is obtained. These specific cases appear as nodal points when the radial displacement on the electron detector is plotted versus the electron TOF (figure 8). The nodes deliver important and valuable information. First, they serve as a good control of the experimental conditions and, more important, they allow a very precise and intrinsic determination of the magnetic field via a measurement of the inverse cyclotron frequency. It is given by the time-distance between two nodes. Whenever important information about the physical process is masked by these nodes, which might happen, the magnetic field can be changed slightly resulting in a corresponding time-shift of the nodal points.

The transverse momentum resolution is given by $\Delta P_{e\perp} = P_{e\perp} \cdot \Delta r/r$, where Δr is the effective position uncertainty resulting from both the detector resolution and the target size.

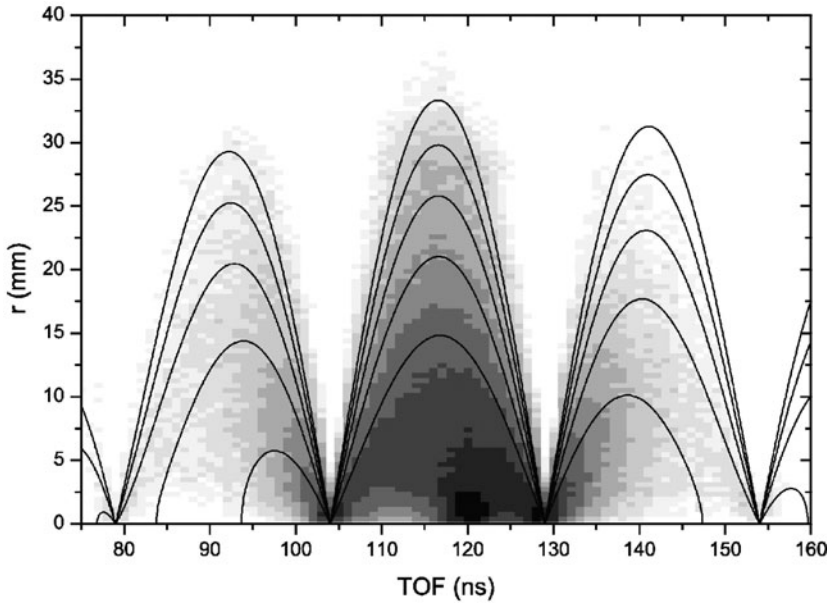

Figure 8. The electron radial displacement r on the detector versus the electron TOF for single ionization of H_2 by 6 MeV proton impact. The cyclotron revolution time corresponds to a magnetic field strength of 14 Gauss. The solid lines are the calculated displacements r for electrons with kinetic energies between 10 and 50 eV in steps of 10 eV. The point (TOF = 120 ns, $r = 0$) represents the origin ($E_e = 0$) on the electron energy scale (from Moshammer *et al* (2003b)).

With $\Delta r = 1\,\text{mm}$ the transverse momentum resolution is $\Delta P_{e\perp} = 0.025\,\text{a.u.}$ for electrons which hit the detector at $r = 4\,\text{cm}$ with $P_{e\perp} = 1\,\text{a.u.}$. This value should be regarded as a lower limit because a finite time resolution, which enters into the determination of the sin-term in (13), as well as magnetic field distortions contribute in addition.

3.2. Target preparation

A prerequisite for high-resolution momentum spectroscopy is a cold atomic or molecular gas-target because typical recoil-ion momenta are of the order of, or even smaller than, the thermal momentum spread at room temperature. In addition, a localized and small target size is needed for particle imaging. Basically two concepts are applied in COLTRIMS and reaction-microscopes.

3.2.1. Supersonic gas-jets. With supersonic gas-jet devices well localized and cold atomic or molecular beams are produced. A gas at high pressure (1–20 atm) is forced through a small nozzle (10–100 μm) into vacuum and thereby accelerated to supersonic speed at the expense of internal motion resulting in an effective cooling. Starting from room temperature the gas is cooled down to temperatures of a only a few Kelvin or even below (for more detailed information, see Miller (1988)). One or several stages with differential pumping are used to handle the enormous gas-load and to maintain a good vacuum in the reaction chamber. To extract a geometrically well defined atomic beam one or several small 'skimmer' apertures are placed behind the nozzle and between the different pumping stages.

For most applications a dense and narrow atomic beam is required which is then crossed with a projectile beam in the interaction chamber. A small interaction volume, which is given by the overlap between the projectile and target-beam, can be obtained with narrow gas beams resulting in a high momentum resolution for particle imaging. Without too much effort particle densities in order of 10^{11}–$10^{12}\,\text{cm}^{-3}$ at a distance of 10 cm away from the nozzle are reachable with supersonic gas-jets.

Though the target gas is cooled by a factor of 1000, or even more if pre-cooling of the gas is used, the residual momentum spread certainly sets a lower limit in the achievable ion momentum resolution. In the direction parallel to the gas-jet velocity the intrinsic jet-temperature dictates the momentum spread. It is about 0.1 a.u. for expansion of He at room temperature. The perpendicular momentum spread is much smaller, it is determined by the jet velocity and the divergence of the atomic beam.

Over the last five years supersonic gas-jets became the standard devices to produce cold and localized atomic or molecular targets in connection with recoil-ion momentum spectroscopy (COLTRIMS). With this method a large variety of different gases is accessible ranging from helium or other noble gases up to any type of molecular gases. Cooling of the gas before expansion is useful for helium or molecular hydrogen to reduce the internal gas-jet temperature and to reach the optimum momentum resolution but it can lead to the formation of clusters or liquid droplets if heavy gases are used. One should also be aware that the internal momentum spread increases with the mass m of the gas atoms $\Delta P_{\text{jet}} \propto \sqrt{m}$ even if the same final jet temperature is obtained. Thus, the generation of a gas jet with a low intrinsic momentum spread of $\Delta P_{\text{R}} < 0.5\,\text{a.u.}$ along the jet-direction is definitely hard to achieve for gases heavier than argon.

3.2.2. Magneto optical traps (MOTRIMS). A significant further reduction of the target temperature is achievable when laser-cooled atoms trapped in a magneto optical trap (MOT)

are used as a target. In the first pioneering experiment Wolf and Helm (2000) measured recoil-ion energies of photoionized Rb atoms extracted from a MOT with very high resolution. Basically, the same method has been used very recently (Flechard *et al* 2001, Turkstra *et al* 2001, van der Poel *et al* 2001) to study single electron capture reactions in keV ion collisions with atoms trapped in a MOT. In these first experiments an unprecedented resolution of $\Delta P_R = 0.03$ a.u. in the recoil-ion momentum (Flechard *et al* 2001) has been achieved by taking benefit from the sub-mK intrinsic temperature of the target. Certainly, this value is not the ultimate resolution set by the gas cloud temperature of typically $100\,\mu$K. It would correspond to a momentum resolution of $\Delta P_R = 0.003$ a.u. for lithium and $\Delta P_R = 0.01$ a.u. for rubidium. With typical densities in the range of several $10^{10}\,\mathrm{cm}^{-3}$ and radii of 1 mm or below the atomic clouds trapped in MOTs are ideally suited as targets for recoil-momentum spectroscopy (MOTRIMS). Another important aspect is that the palette of possible targets is considerably widened. All alkali and earth alkaline atoms are easily trapped in a MOT, but they are hardly produced and cooled in a supersonic gas-jet. These atoms are in some situations of particular interest because they represent single active electron (SAE) targets and, therefore, have many features in common with atomic hydrogen, the simplest atomic target, which is not directly accessible to COLTRIMS because efficient cooling methods are not available. Finally, atoms in traps can be easily prepared in excited states and even aligned with respect to the laboratory frame.

3.3. New developments

In this section, a few technical developments related to recoil-ion and electron momentum spectroscopy, which are still ongoing and which might play a role in future applications, are listed and briefly discussed. Though this list is quite incomplete it represents a still continuing evolution of many-particle imaging devices to investigate atomic and molecular reactions.

The limited number of target species accessible to COLTRIMS is, at least to some extent, a constraint. This is mainly because both conditions, high target density and extremely low temperature, are hard to combine if one is interested in targets like highly excited atoms, metastable helium, atomic hydrogen, vibrationally cold molecules or others. Very recently, the Frankfurt group succeeded in producing a supersonic jet of dense and internally cold metastable He-atoms (Jahnke 2003). A high pressure discharge burning between the entrance and exit surface of a $50\,\mu$m nozzle collisionally excites He while the following adiabatic expansion into the vacuum reduces the internal temperature. After a subsequent Stern–Gerlach magnet the beam can be used for experiments with oriented and cold metastable helium atoms.

If complex targets are used, for example, molecules or clusters, the number of particles ejected from a break-up reaction can be quite large. The desire to detect all of them increases the demands on the detectors concerning their multi-hit capability. Delay-line anodes for position encoding have been developed which fulfill the requirement of almost negligible dead-time (Jagutzki *et al* 1998, 2002, 2002a, b). On the other hand, with on-going development of integrated electronic circuits concerning speed and compactness, large area pixel anodes with ultra-fast readout of individual pixels are in the realm of possibility. Presently, work is in progress to develop such an anode where one thousand or more pixels are individually read out using highly integrated electronics mounted on-board directly at the anode.

The flexibility of imaging spectrometers can be increased further if the traditional concept of using only static electric and magnetic fields for projection and guiding of charged particles is skipped. Obviously, the application of pulsed or otherwise time-dependent fields can help to adapt the spectrometer performance to specific problems. To study, for example, molecular fragmentation, maintaining at the same time a high-resolution for the emitted electrons, a pulsed

extraction field can be used. The initially small field is ramped up considerably on a sub-μs timescale whenever an electron hits the detector. Because the ions do not travel over a large distance during this short time they experience a large acceleration ensuring 4π detection efficiency for them. This method has been successfully applied for the first time to investigate double photoionization of molecular hydrogen (Dörner *et al* 1998a). An electric field between two grids placed at an appropriate position in the ion or electron flight-path can serve as a switchable potential barrier. By gating the applied voltage in synchronization with an external time reference unwanted parts of the TOF spectrum, which would overload the detector, can be masked out. This method has been applied to investigate electron transfer reactions in fast proton helium collisions (Schmidt *et al* 2002). A similar approach has been used for high-resolution electron capture measurements. There the recoil-ions have been extracted exactly parallel to the incoming beam direction. A pulsed electric field acting perpendicular to the ion trajectory within the drift path kicked the recoil-ions onto the detector, which was mounted beneath the projectile beam axis (Fischer *et al* 2002). In general, the possibilities opened up with pulsed electric fields are by far not yet exhausted.

In order to boost the resolution for high-energy electron imaging (>100 eV) Weber *et al* (2003) succeeded in combining a retarding electric field with the solenoidal magnetic guiding field. Maintaining the 4π solid angle, they reached a resolution of <1 eV at 300 eV electron energy.

Recently, the imaging concept of the reaction-microscope has been extended to the detection of electrons emitted from surfaces (Hattass *et al* (2003), patented by Moshammer and Ullrich (1998)). For ions emerging from solids, this technique has been developed early by Moshammer *et al* (1990) (Matthäus *et al* 1991, 1993) and was recently used by Schmidt-Böcking *et al* (2003) (see also Jalowy *et al* (2002, 2002a, b, 2003, 2003a)).

4. Results

4.1. Photons

Since 1994 reaction-microscopes have been successfully used to investigate the interaction of single photons with atoms and molecules at synchrotron radiation sources around the world. The main topics addressed in these studies were:

1. Separation of photoabsorption and Compton scattering in single and double ionization of helium (Spielberger *et al* 1995, 1996, 1999, Krässig *et al* 1999) and the precision measurement of the ratio of double to single ionization of helium by photoabsorption (Dörner *et al* 1996b).
2. Kinematically complete studies of double ionization of helium by photoabsorption.
3. The geometry of small photoexcited molecules (Muramatsu *et al* 2002, Ueda *et al* 2003).
4. Photo- and Auger-electron angular distributions from small fixed-in-space molecules.

We will briefly review the work on topics 2 and 4 in sections 4.1.1 and 4.1.2. For topics 1 and 3 we refer the reader to the original literature and previous reviews.

4.1.1. Double ionization of atoms: a brief summary. Following the pioneering kinematically complete experiment on double photoionization of helium by Schwarzkopf *et al* (1993) today experimental data have been reported for energies from 0.1 eV (Huetz and Mazeau 2000) to 450 eV above threshold (Knapp *et al* 2002) for linear as well as circular polarized light. This work together with the impressive theoretical progress in this field has recently been reviewed

by Briggs and Schmidt (2000). We highlight here mainly the contributions of RIMS to this field.

The three particles in the final state after photo double ionization are kinematically completely determined by five linear independent momentum components. They can be measured either by detecting two electrons in coincidence or one electron and the recoiling ion momentum. The key advantage of the coincident imaging of ion and electron momenta is the 4π solid angle achieved for all energy sharings between the electrons. This coverage of the total final state phase space has many benefits:

1. An overview can be gained showing which regions of phase space are most important for the process of double ionization, i.e. which contribute most to the total cross section.
2. The data can be transformed to any set of coordinates. Thus, not only the traditional angles and energies of the two electrons (or momenta $\vec{k}_1 \equiv \boldsymbol{k}_1$, $\vec{k}_2 \equiv \boldsymbol{k}_2$) can be chosen, but also collective coordinates like Jacobi coordinates ($\vec{k}_+ = \vec{k}_1 + \vec{k}_2 \equiv \boldsymbol{k}_+$ and $\vec{k}_- = \frac{1}{2}(\vec{k}_1 - \vec{k}_2) \equiv \boldsymbol{k}_-$) or hyperspherical coordinates. In such momentum space images the characteristics of the photo double ionization process become directly visible (Dörner *et al* 1996b).
3. The data can be reliably normalized on absolute scale (for details see Bräuning *et al* (1998), Dörner *et al* (1998)), which is very difficult otherwise (Schwarzkopf and Schmidt 1995). Such absolute data provide a particular sensitive test for theory (Pont *et al* 1996, Kheifets and Bray 1998, Lucey *et al* 1998).

To discuss the main physical effects and the main features in the cross section, we start from partially differential data providing an overview progressing to fully differential results.

Figure 9 shows the momentum distributions of one of the electrons and of the doubly charged ion at photon energies of 1 eV, 20 eV and 100 eV above threshold. The striking difference between the electronic and ionic distributions reflects part of the mechanisms leading to photo double ionization. The photon acts upon a charge dipole in the atom. This dipole might be thought of as consisting of the positive ion on one pole and either the centre of charge of the electron pair or one of the electrons on the other pole. In either case, the first step of the absorption of the photon will imprint the dipolar characteristics of the linear polarized photon on the distribution of the fragments of a charge dipole. The experiments indicate that the momentum distribution of the nucleus shows a memory of this absorption of the photon. At low excess energies this pattern is completely washed out in the electronic momentum distribution by the electron–electron interaction which is indispensable for double ionization. For 100 eV excess energy (and even more pronounced at 450 eV (Knapp *et al* 2002)) the fast electron also shows a dipolar emission pattern (figure 9(*h*)). It is very illustrative to switch from single electron coordinates $\vec{k}_{1,2}$ to the Jakobi coordinates $\vec{k}_{+,-}$, corresponding to a change to a molecular perspective of the He atom (Feagin and Briggs 1986). This is most useful if the saddle region of the potential surface governs the final state of the reaction, which is expected close to threshold (Wannier 1953). The two electrons then create a two-centre saddle potential in which the nucleus is located. The coordinate $\vec{k}_-$ is along the line connecting the two electrons and $-\vec{k}_+$ is the momentum vector of the ionic core. At 1 and 20 eV there is a clear propensity for an escape of the nucleus perpendicular to $\vec{k}_-$. This can be understood by a Wannier type analysis, which predicts, that double ionization near threshold can only be reached if ionic and electron motion are perpendicular, all other geometries lead to single ionization (Wannier 1953, Huetz *et al* 1991, Feagin 1995, 1996, Kazanski and Ostrovsky 1995, 1993, 1994). In the molecular picture the electronic separation $\vec{R}$ is interpreted as a molecular axis and the projection m of the total angular momentum on this axis is taken as an approximate quantum number. This propensity for $m = 1$ breaks down at 100 eV. Without this propensity,

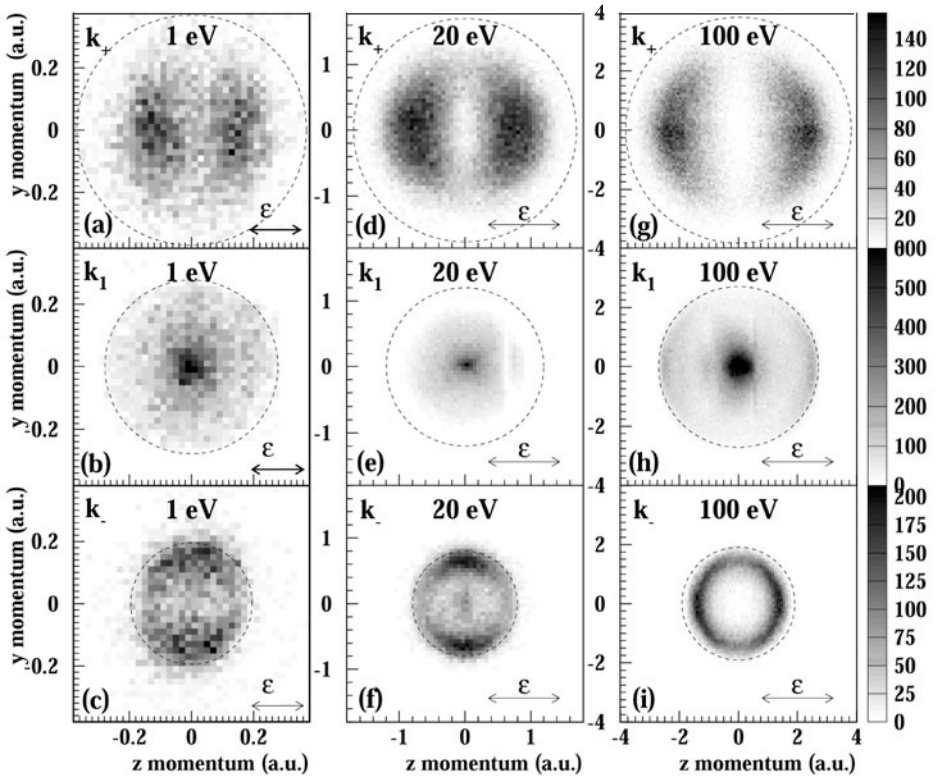

Figure 9. Density plots of projections of the momentum distributions from double ionization of He for three different energies. From left to right: data sets for 1, 20 and 100 eV above threshold. The z and y components of the momentum are plotted on the horizontal and vertical axes, respectively. The polarization vector of the photon is in the z-direction and the photon propagates in the x-direction perpendicular to y and z. For 100 eV above threshold only events with -1 a.u. $< k_x <$ 1 a.u. are projected onto the plane. (*a*), (*d*) and (*g*): momentum distributions of the He^{2+} ion (k_+) for 1, 20 and 100 eV above threshold. (*b*), (*e*) and (*h*): electron momentum (k_1), and (*c*), (*f*) and (*i*) electron pair relative momentum $(k_1 - k_2)/2$. The circle locates the maximum possible momentum in each coordinate at the respective photon energy (from Dörner *et al* (1996), Bräuning *et al* (1997), Knapp *et al* (2002a)).

the main motivation for analysing the process in Jacobi coordinates is lost. The evolution of the three-body system is no longer governed by the saddle region of the potential.

We now investigate the internal structure of the two-electron continuum wave in $\vec{k}_1$, $\vec{k}_2$ coordinates (figure 10). Neglecting the (small) photon momentum, the vector momenta of the ion and both electrons have to be in one plane. Figure 10(*a*) shows the electron momentum distribution in this plane for linear polarized light. The data are integrated over all orientations of the polarization axis with respect to this plane; the x-axis is chosen to be the direction of one electron. The structure of the observed momentum distribution is dominated by two physical effects. First the electron–electron repulsion leads to almost no intensity for both electrons in the same half plane. Second, the $^1P^o$ symmetry leads to a node in the square of the wave function at the point $\vec{k}_1 = -\vec{k}_2$ (Huetz *et al* 1991, Schwarzkopf *et al* 1993, Maulbetsch and Briggs 1995, Malegat *et al* 1997). The corresponding data for left and right circular polarized light are shown in figures 10(*b*) and (*c*). They show a strong circular dichroism, i.e. a dependence on the chirality of the light. This might be surprising since the helium atom is perfectly spherical symmetric. Berakdar and Klar (1992) first pointed out that for circular

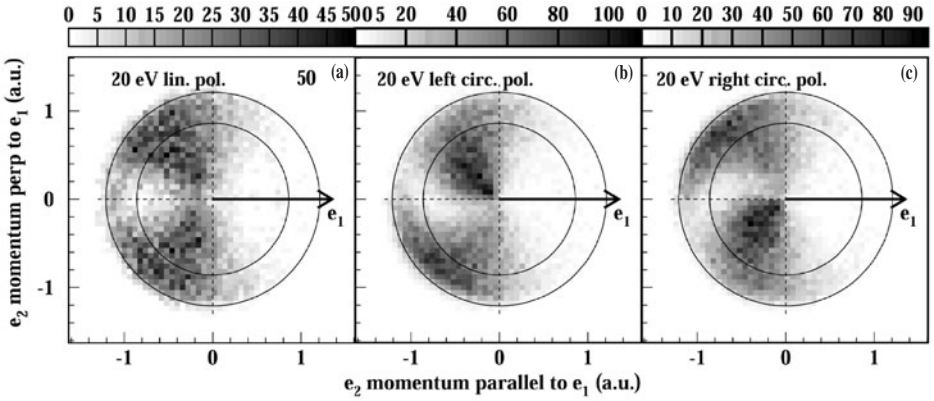

Figure 10. Photo double ionization of He at 20 eV above threshold by linear, left and right circular polarized light. Shown is the momentum distribution of electron 'two' for fixed direction of electron 'one' as indicated by the arrow. The plane of the figure is the momentum plane of the three particles. The data of (*a*) are integrated over all orientations of the polarization axis with respect to this plane. The figure samples the full cross sections, for all angular and energy distributions of the fragments. The outer circle corresponds to the maximum possible electron momentum, the inner one to the case of equal energy sharing. In (*b*) and (*c*) the light propagates into the plane of the figure, the electrons are confined to the plane perpendicular to the light propagation (from Dörner *et al* (1998b) and Achler *et al* (2001)).

dichroism to occur it is sufficient that the direction of light propagation and the momentum vectors of the electrons span a tripod of defined handedness. This is the case if the two electrons and the light direction are non-co-planar and the two electrons have unequal energy (see Berakdar *et al* (1993), Berakdar (1998, 1999), Berakdar and Klar (2001) for a detailed discussion and experimental results, Viefhaus *et al* (1996), Kheifets and Bray (1998), Mergel *et al* (1998), Soejima *et al* (1999), Kheifets *et al* (1999a), Achler *et al* (2001), Collins *et al* (2002)).

Finally, FDCS can be investigated. The main features seen here at low to moderate excess energies are the interplay between selection rules resulting from the $^1P^o$ symmetry and the electron repulsion. A detailed discussion goes beyond the scope of this paper; we refer the reader to (Briggs and Schmidt 2000). In general, very good agreement is found between the experimental data even on an absolute scale and the most advanced theoretical approaches (Pont and Shakeshaft 1995, 1996a, Kheifets and Bray 1998, 1998a, 2000, Malegat *et al* 2000, 2002, Colgan *et al* 2001, Colgan and Pindzola 2002, Selles *et al* 2002). At very high excess energies of 450 eV finally (Knapp *et al* 2002), one electron is found to leave fast, carrying away most of the photon energy and angular momentum. In the angular distributions of the second, slow electron clear traces of the mechanism which led to its ejection can be found (see also Teng and Shakeshaft (1994), Keller (2000)). Electrons emitted via the shake-off (SO) mechanism are expected to be isotropic or slightly backward directed with respect to the primary electron, while electrons knocked out in a binary collision (two-step 1 (TS1)-mechanism) will yield 90° between the two electrons. At 529 eV photon energy the electron angular distributions show a dominance of the SO mechanism for secondary electrons which have very low-energy (2 eV) and display clear evidence that an inelastic electron–electron scattering is necessary to produce secondary electrons of 30 eV (Knapp *et al* 2002) (see figure 11).

4.1.2. Photoionization of fixed-in-space molecules. The combination of photons of narrow bandwidth and well controlled polarization from synchrotron radiation sources with electron

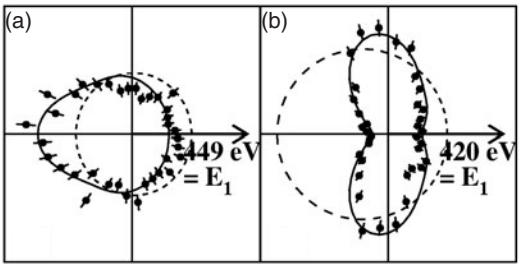

Figure 11. FDCS of the He photo double ionization at 529 eV photon energy. The primary photoelectron 'one' emission direction is indicated by the arrow, the polarization is horizontal, the angular distribution of the complementary electron 'two' with energy E_2 is given by the symbols. (*a*) 447 eV $< E_1 <$ 450 eV, 0 eV $< E_2 <$ 3 eV. (*b*) 410 eV $< E_1 <$ 430 eV, 20 eV $< E_2 <$ 40 eV. (*a*) Shows the dominance of SO, (*b*) the 90° emission indicates the importance of TS1 at this energy. The solid line shows the full CCC calculation, the dashed line is the SO only part of the CCC calculation (from Knapp *et al* (2002)).

and ion imaging provides an extremely versatile and powerful tool for molecular physics. The photon allows complete control of the angular momentum and the total energy of the molecular states populated. The kinematically complete measurement of the emitted electron(s) and fragment ions allows one to measure the response of the molecule to the energy and angular momentum deposition. Such processes of photoexcitation or ionization of molecules can often be split into two independent sub-processes (Born-Oppenheimer approximation): first, a fast electronic transition occurs, followed by the slow process of dissociation of the molecular ion. The ion momenta resulting from dissociation are usually in the eV-regime, i.e. at least two orders of magnitude higher than in atomic ionization processes. Of particular interest are dissociation processes which are fast compared to typical rotation times of the molecule. In this case, the molecular orientation at the instant of the electronic transition can be determined *a posteriori* by measuring the direction of the fragments (axial recoil approximation, Zare (1972)).

Electron angular distributions for molecules fixed-in-space by detection of the molecular fragments have been first performed by Shigemasa and co-workers with traditional analysers for electrons and ions (Shigemasa *et al* 1995) (see also Watanabe *et al* (1997), Shigemasa *et al* (1998), Cherepkov *et al* (2000, 2000a), Ito *et al* (2000, 2000a), Motoki *et al* (2002) for later experiments by this group). Another group has combined TOF electron spectrometers (Golovin *et al* 1997, Heiser *et al* 1997, Gessner *et al* 2002) with imaging of the molecular fragments.

We will restrict the further discussion on experiments where coincident imaging of electrons and ionic fragments has been used for valence or innershell ionization. A variety of molecules has been studied, including CO (Hikosaka and Eland 2000, Landers *et al* 2001, Weber *et al* 2001a, Jahnke *et al* 2002), N_2 (Hikosaka and Eland 2000a, Jahnke *et al* 2002), NO (Gessner *et al* 2002), CO_2 (Saito *et al* 2003), O_2 (Heiser *et al* 1997, Lafosse *et al* 2001, 2002), H_2 (Dörner *et al* 1998a, Hikosaka and Eland 2002), CH_3Cl (Hikosaka *et al* 2001), CH_3F (Hikosaka *et al* 2001) and $C_2H_{2,4,6}$ (Osipov *et al* 2003).

From the energy correlation between photoelectrons, Auger electrons and some of the kinetic energy of the fragments (kinetic energy release (KER)) mostly the ionization or excitation channels (Lafosse *et al* 2000, 2001, Hikosaka and Eland 2002) or the Auger decay paths (Weber *et al* 2003) can be disentangled. One example where NO is ionized by absorption of a 23.64 eV photon is shown in figure 12. The diagonal lines correspond to different excited

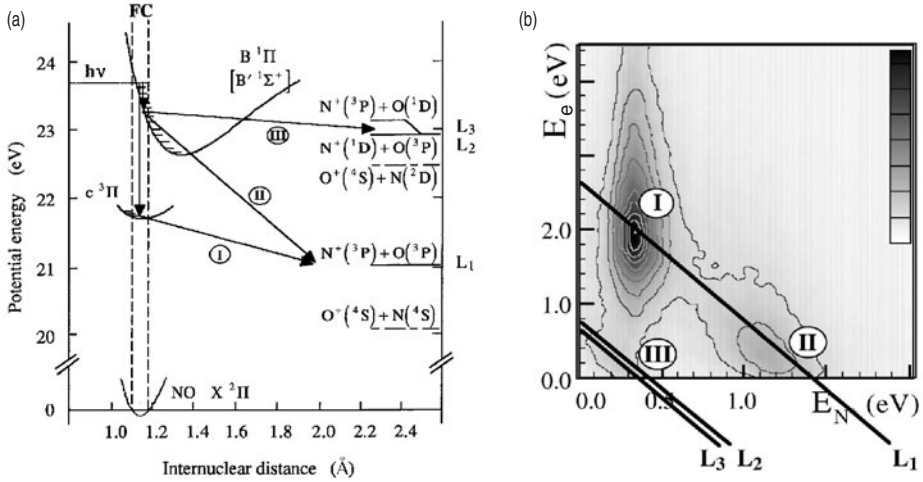

Figure 12. (*a*) Simplified potential energy diagram for NO^+. (*b*) Electron and N^+-ion kinetic energy correlation for photoionization of NO at 23.64 eV photon energy. The three numbered island correspond to the three reaction pathways shown in (*a*) (from Lafosse *et al* (2000)).

final states of the N^+ fragment. The three islands show different reaction paths which are shown in the correlation diagram in figure 12(*b*).

For a well-controlled reaction pathway the angular distribution of the electrons can be studied. In contrast to the case of atomic photoionization, photoelectron angular distributions from molecules show a very rich structure (Dehmer and Dill 1976, Dill 1976). Examples are shown in figure 13. What are the physical mechanisms producing this structure? From the angular momentum perspective these distributions show that high angular momenta are present in the electronic wave function. The one unit of angular momentum of the photon is absorbed by the molecule creating an entangled state of the continuum electron and the molecular ion. The angular momentum part of the continuum electron and the molecular ion wavefunction are mirror images of each other. The electron leaves the rotational molecular ion wave packet behind which is the coherent superposition of many angular momentum states (Choi *et al* 1994) and, vice versa, the continuum electron wave function is a superposition of many angular momentum components. This angular momentum exchange between electron and molecular ion results from a multiple scattering of the electron wave on its way out of the molecular potential. If one discusses this process not on an angular momentum basis but in a plane wave perspective (corresponding to the asymptotically detected linear momenta) one might say that the many narrow minima and maxima in the angular distribution are the result of multiple interferences. There are many semi-classical paths on which the electron can get from its origin, e.g. at the carbon centre to the final detector direction. All these different paths have to be added coherently. For example, the direct wave from the carbon has to be added to a wave scattered at the oxygen. The phase shift between the different paths is determined by the details of the molecular potential. As a consequence, the narrow interference minima and maxima are a very sensitive probe of the potentials used. In reality, this problem becomes more interesting by the fact that this potential is time-dependent since the molecular wave function reacts to the creation of a hole by the photon. For innershell ionization, for example, very good results are obtained by assuming a frozen potential with a charge of $\frac{1}{2}$ K-hole instead of the full charge.

The angular distributions also depend strongly on the direction of the photon polarization axis with respect to the molecular axis, since this determines the projection of the photon

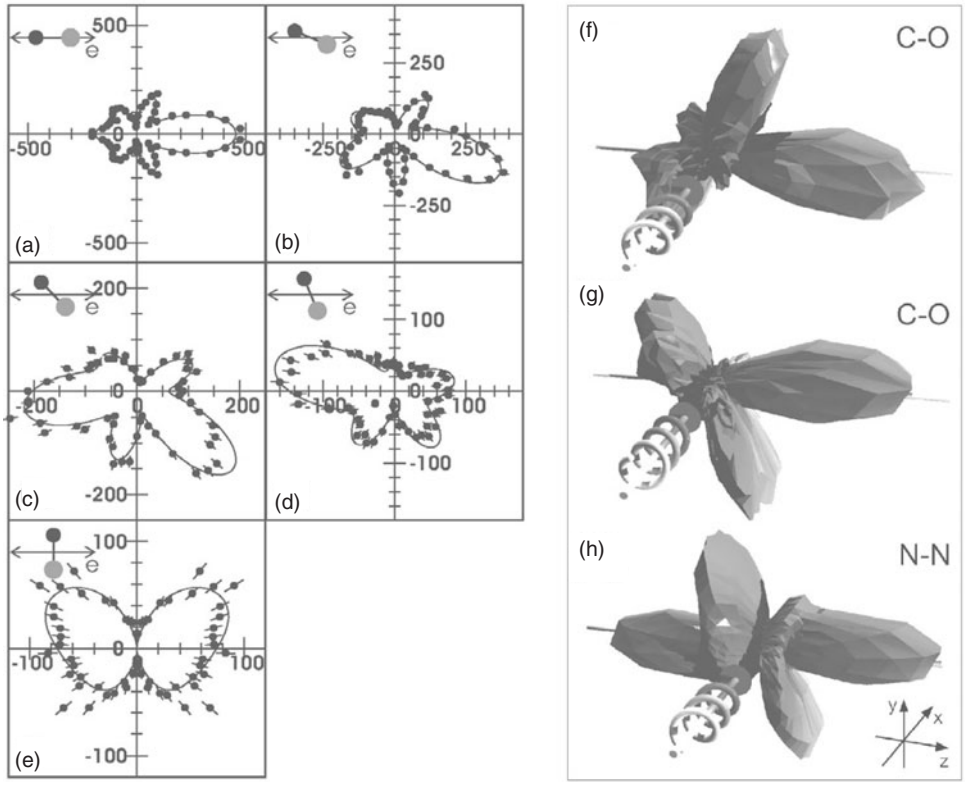

Figure 13. Angular distribution of K-shell photoelectrons at 10 eV electron energy. (*a*)–(*e*) Carbon K-shell electrons from CO molecule for linearly polarized light. The orientation of the molecule and the polarization vector is indicated in the figure. The black dot is the carbon, the grey dot is the oxygen end of CO (from Landers *et al* (2001)). The full line is a fit of spherical harmonics for (*f*) and (*g*) left and right circular polarized light. CO orientation along the rod as indicated. The direction of the photon is shown by the spiral. (*h*) as (*f*) and (*g*) but for N_2 (from Jahnke *et al* (2002)).

angular momentum onto this axis (see figures 13(*a*)–(*e*)). By combining linearly and circularly polarized light, the amplitudes and phases of the different angular momentum partial waves can be measured (Gessner *et al* 2002, Jahnke *et al* 2002, Motoki *et al* 2002). In addition, the electron wavelength can be scanned by scanning the photon energy. By this technique the diffraction pattern of an electron wave launched from a well defined position inside a molecule can be measured, the molecule can be 'illuminated from within' (Landers *et al* 2001). Once the multiple scattering problem is sufficiently understood theoretically one can use the sensitivity of the electron diffraction pattern on the molecular geometry and potential to test not the scattering calculation but the potential itself. In solid state physics at least the nearest neighbour geometry is often explored in this way by 'x-ray-photoelectron diffraction' (XPD).

One might ask, if for innershell ionization the two steps of photoelectron emission and the subsequent Auger electron emission can be treated independently (two-step model) (Dill *et al* 1980, Kuznetsov and Cherepkov 1996, Guillemin *et al* 2001). The validity of the two-step model has recently been confirmed in a study of the decay channel and molecular frame angular distribution of the Auger electron from carbon K-shell photoionized CO (Weber *et al* 2003). The Auger electron angular distribution in the molecular frame is shown in figure 14, for two different Auger decay channels. A clear fingerprint of the symmetry of the transition is seen in

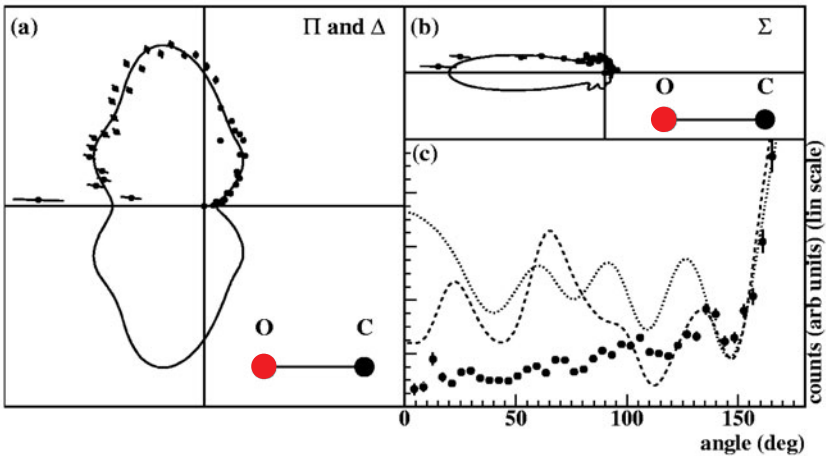

Figure 14. Angular distribution of carbon-K-Auger electrons from CO^+. (*a*) For a Π and Δ transition ($CO^+(^1\Sigma^+) \rightarrow CO^{2+}(^1\Delta, {}^3\Pi, {}^1\Pi$ transition). (*b*) Corresponds to a $CO^+(^1\Sigma^+) \rightarrow CO^{2+}(^1\Sigma)$ transition. (*c*) same data as in (*b*): 0° corresponds to emission in direction of the carbon. The full lines in all figures are fits of Legendre polynomials to guide the eye. Other lines in (*c*) are results of a multiple scattering calculation for an S electron wave starting at the carbon centre in CO^{2+}. - - - -: both vacancies in the CO^{2+} at C(2p). ·····: one vacancy each at C(2p) and O(2p). The absolute height of the calculation is arbitrary (from Weber *et al* (2003)).

the angular distribution. A Π transition leads to emission preferentially perpendicular to the molecular axis while for a Σ transition a strongly peaked emission along the molecular axis is found. The K-hole is located at the carbon; the Auger electrons, however, show a striking narrow emission in the direction of the neighbouring oxygen atom. Such an emission into the direction of the neighbouring atom is known from photoelectron diffraction as 'forward focusing' (Poon and Tong 1984). The screened Coulomb potential next to the source of a photoelectron wave can act as a lens which collects a large amount of the electron flux into the forward direction. A close inspection of this pattern (figure 14(*c*)) shows an oscillatory structure. This is due to a diffraction of the Auger electron wave in the two-centre potential as has been reported in the theoretical study of Zähringer *et al* (1992).

In the field of photoionization of molecules only the first steps have been done so far and many exciting challenges still lie ahead. One open problem is electron correlation in direct double ionization of fixed-in-space H_2 (Kossmann *et al* 1989, Reddish *et al* 1997, Feagin 1998, Reddish and Feagin 1998, Dörner *et al* 1998a, Walter and Briggs 1999, 2000). In this case not only the internuclear axis but also the internuclear distance at the instant of photoabsorption can be measured via the ion fragment momenta. This would, for the first time, allow control of the initial state in a double ionization process (Weber 2003). Another very promising route is to take such experiments to the time domain by using pump-probe techniques (Davies *et al* 2000). Among the open and controversially discussed questions is also the localization or delocalization of vacancies in homonuclear molecules (Pavlychev *et al* 1998) as well as multiple electron processes manifested in the satellite lines (De Fanis *et al* 2002).

4.2. Single and multiple ionization in intense laser fields

The interaction of intense coherent light with atoms, molecules, clusters or solids has attracted increasing attention in the recent past triggered by the tremendous technical progress in the

realization of such radiation. Pulse times below 100 fs and intensities exceeding $10^{16}\,\mathrm{W\,cm^{-2}}$ are routinely realized nowadays (see, e.g. Brabec and Krausz (2000)) using Ti : Sa lasers (800 nm, $\hbar\omega = 1.5\,\mathrm{eV}$). Single electron emission, the intensity dependence of ion rates, multiple ionization yields, dissociation of molecules or clusters, harmonic generation, etc have been explored in detail over many years essentially using single particle detection techniques (see, e.g. DiMauro and Agostini (1995)). A profound theoretical understanding of non-linear multi-photon processes has emerged for reactions that either involve only one electron or for processes where electrons can be considered to act independently within a so-called 'SAE' (single active electron) description (see, e.g. Protopapas *et al* (1997)).

Many-electron dynamics, i.e. the femtosecond time-dependent correlated motion of several electrons and ions in the field, however, which determine, for instance, pathways to multiple ionization or the dissociation of molecules and clusters, cannot be treated by *ab initio* theories presently. Even helium double ionization, the most simple two-electron reaction, has remained subject of numerous controversial debates over the last decade (see, e.g. Lambropoulos *et al* (1998)). Experimentally, a break-through was achieved about three years ago with the first successful implementation of reaction-microscopes (see section 3) producing data with unprecedented resolution and completeness for many-electron processes.

This section tries to summarize new results on the fragmentation of atoms obtained using these next-generation methods (for a recent review on the field, see also Dörner *et al* (2002)), giving only a few references on molecular dissociation work. After the introduction, recent data on single ionization in the tunnelling regime will be described in section 4.2.2 followed by a selection of illustrative results on double ionization in section 4.2.3 giving reference to available theoretical predictions. Sections 4.2.4 and 4.2.5 deal with the details of the correlated electronic motion.

4.2.1. Single ionization: recollision in the tunnelling regime. Single electron emission with eV up to MeV electron energies as a result of the interaction of intense laser pulses with atoms has been explored in great detail in the past, covering a large range of laser intensities. At low intensity, for typical Keldysh (1964) parameters $\gamma = (I_\mathrm{P}/2U_\mathrm{P})^{1/2} \geqslant 1$ (I_P: ionization potential; $U_\mathrm{P} = I/(2\omega)^2$: ponderomotive potential; I, ω: laser intensity and frequency), the 'quantum-nature' of the field causes rich structure in the photoelectron spectra due to a variety of processes that might occur, like 'ATI', 'channel opening' or 'closing', 'resonant enhanced ionization', coherent scattering, etc. At high intensities instead, for $\gamma < 1$ where the field might be treated classically, the spectra become increasingly smooth and unstructured. This has been explained early by quasi-static tunnelling (Keldysh 1964, Faisal 1973, Corkum *et al* 1989, Delone and Krainov 1998) or by treating ATI quantum mechanically (the so-called Keldysh–Faisal–Reiss (KFR)-model Keldysh (1964), Faisal (1973), Reiss (1980, 1987)). In tunnelling theory, the active electron tunnels through the barrier in a first step and is then accelerated, gaining drift energy in the oscillating field $\vec{E}(t) = \vec{E}_0 \sin(\omega t)$ in a second step. The drift momentum $P_\mathrm{drift}(t_0) = (q/\omega)E_0 \cos(\omega t_0)$ is a smooth function of the tunnelling phase $\varphi = \omega t_0$ and is zero for tunnelling at the maximum of the field. The maximum drift energy of $2U_\mathrm{P}$ is reached for tunnelling at a phase where the field is zero. Immediately, interest concentrated nearly exclusively on large electron energies, beyond $2U_\mathrm{P}$, where significant deviations from simple tunnelling as well as KFR-models were recognized and explained by 're-scattering' of the oscillating electron at its parent ion (see, e.g. Walker *et al* (1996), Delone and Krainov (1998), Sheehy *et al* (1998)) causing acceleration up to a maximum energy of $10U_\mathrm{P}$.

Recently, the low-energy part of the spectrum has been explored for the first time for single ionization of Ne in the tunnelling regime (25 fs, $1 \times 10^{15}\,\mathrm{W\,cm^{-2}}$, 800 nm, linear polarization)

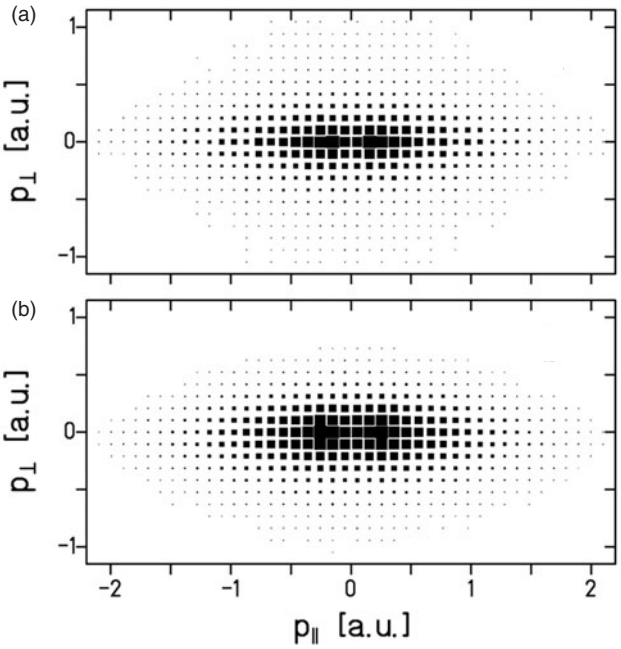

Figure 15. Longitudinal and transverse momentum distribution of Ne^{1+} recoil-ions (1a) and of electrons (1b) for single ionization by 1×10^{15} W cm^{-2}, 25 fs laser pulses at 800 nm. The z-scale is linear with the box sizes proportional to the number of events at a given momentum (from Moshammer *et al* (2003a)).

at $\gamma = 0.39$ by mapping the complete final state momentum space with high-resolution in coincidence with Ne^{1+} ions (Moshammer *et al* 2003a). As shown in figure 15, smooth distribution without any indication of an ATI peak structure is observed along the longitudinal ($P_\parallel$) as well as transverse ($P_\perp$) momentum directions for the electron (figure 15(a)) as well as for the ion (figure 15(b)), as expected. Surprisingly, however, a distinct minimum at zero electron momentum was found in striking contradiction to the well accepted tunnelling theory. Since tunnelling is most likely at the maximum of the field ($\varphi = \pi/2$) and since those electrons receive zero drift momentum, a Gaussian distribution function is predicted with a maximum of the electron momentum distribution at $P_{e\parallel} = 0$, independent of $P_{e\perp}$.

Quantitatively this is illustrated in figure 16, where the tunnelling theory result (Delone and Krainov 1991) for 0.7×10^{15} W cm^{-2} is shown (thin line) along with the experimental data from figure 15 projected onto the longitudinal axis for all transverse momenta. Also indicated (thick line) is the result of recent semi-classical calculations (Chen and Nam 2002) for an intensity of 0.7×10^{15} W cm^{-2} and a helium target, clearly showing not only a minimum at $P_{e\parallel} = 0$ but also deviations from the Gaussian shape in qualitative agreement with the experimental data. Here, in order to model single ionization, electrons are set into the continuum with a velocity distribution obtained from the wave function of the tunnelled electron. Then, the set of trajectories is propagated according to Newton's classical equations in the combined field of the laser and of the Coulomb potential of the residual singly charged helium ion. The latter is also modelled classically assuming the electron to be in the He^+ GS represented by a micro-canonical distribution. Thus, all mutual interactions between all particles are accounted for during the whole laser pulse in all three dimensions.

Within this model both, the minimum at zero momentum as well as the deviations from the Gaussian-shaped tunnelling-theory prediction result from the interaction of the tunnelled

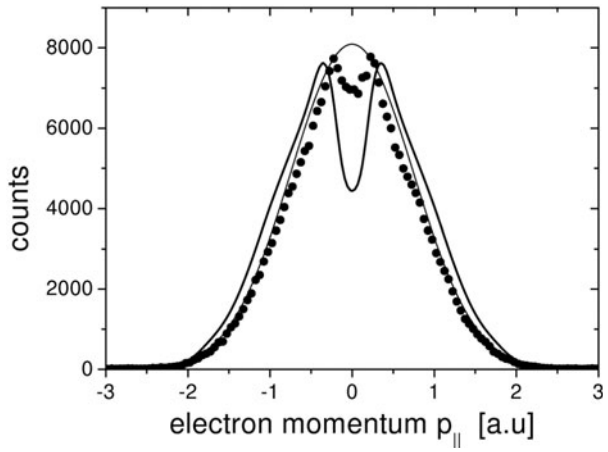

Figure 16. Longitudinal momentum distribution of the emitted electron ($P_{e\|}$) for the same conditions as in figure 15. ——: prediction of tunnelling theory (Delone and Krainov 1991) for 0.7×10^{15} W cm^{-2}. ——: prediction of semi-classical calculations at 0.7×10^{15} W cm^{-2} for He single ionization (Chen and Nam 2002) (from Moshammer *et al* (2003a)).

electron with its parent ion, i.e. are a consequence of rescattering. Electrons tunnelling in the maximum of the field experience multiple recurrences to the parent He^+ ion with low velocities and, accordingly, large elastic scattering cross sections. Thus, they are effectively redistributed to larger transverse momenta depleting at the same time the intensity at $P_{e\perp}$ close to $P_{e\|} = 0$. Switching off the interaction with the He^+ ion, which can either be represented classically as described above or simply by a screened potential, causes both characteristic features to disappear and the tunnelling-theory result is recovered. Whereas the width of the momentum distribution significantly depends on the intensity, the minimum however is observed for all power densities investigated, ranging from 0.3×10^{15} to 1×10^{15} W cm^{-2}.

Thus, high-resolution momentum imaging surprisingly revealed new insight into single ionization in the tunnelling regime at low electron energies, a process that had been considered to be well understood before. Whereas effects from re-collision have been clearly observed and are commonly accepted to be of decisive importance at high electron energies beyond $2U_P$, recollision has never been discussed in the context of extremely small electron momenta at essentially zero electron energy. Recent purely classical, and, thus, 'over-the-barrier' calculations on strong field single ionization (Feeler and Olson 2000) showed a maximum at zero momentum leading to the conclusion that the dip in the semi-classical theory seems to be closely connected with the quantum nature of the first 'tunnelling' step.

4.2.2. Double ionization: non-sequential and sequential. In figure 17 momentum distributions parallel ($P_\|$) and perpendicular ($P_\perp$) to the laser polarization axis are shown for $Ne^{(1-2)+}$ ions created in intense, linear polarized fields in the sequential and non-sequential (NS) regime, at 25 fs pulse length (Moshammer *et al* 2000). Similar data have been published for He by Weber *et al* (2000) and Ar by Weber *et al* (2000a) and Feuerstein *et al* (2001). Note, in disagreement with figures 15 and 16 (Moshammer *et al* 2003a), the momentum distribution for single ionization displays a maximum at zero momentum. This is due to the limited recoil-ion momentum resolution achieved in these early measurements being not sufficient to observe the dip.

As for single ionization in the more recent experiments, a pronounced double peak structure along the polarization direction was found for double and triple ionization in an

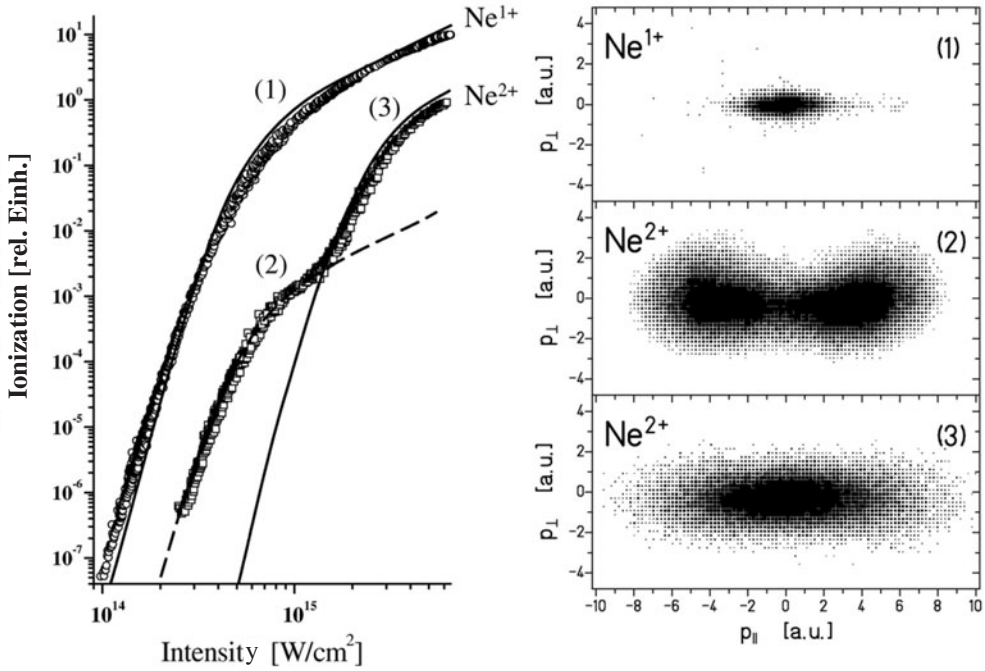

Figure 17. Ne double ionization by 780 nm, 25 fs laser pulses. Left: Ne^{1+}, Ne^{2+} yields as a function of the laser intensity (from Larochelle *et al* (1998)). ——: independent event model. Right: ion momentum distributions for different intensities (see text; from Dörner *et al* (2002)).

intensity regime (see (2) in figure 17) where double ionization is dominated by NS mechanisms (Larochelle *et al* 1998). This structure automatically ruled out 'SO' (Fittinghoff *et al* 1992) or 'collective tunnelling' (Eichmann *et al* 2000) as dominant NS double ionization mechanisms, terminating ten years of discussion. At the same time, the peaks were found to be compatible with the 'antenna' (Kuchiev 1987) or the 'recollision' mechanism (Corkum 1993) as was first shown within classical considerations (Feuerstein *et al* 2000, Moshammer *et al* 2000, Weber *et al* 2000). Subsequently, a variety of theoretical predictions (see the detailed discussion and references in Dörner *et al* (2002)) based on S-matrix theory, on the numerical solution of the time-dependent Schrödinger equation (TDSE) as well as on the classical or semi-classical approximations essentially established the double peak-structure and recollision as the dominant NS double ionization mechanism (see also earlier measurements with circularly polarized light by Fittinghoff *et al* (1994) and Dietrich *et al* (1994)). In the sequential regime a broader distribution is observed with a single peak at zero momentum along the field axis (see (3) in figure 17).

Interestingly, the ability of the experiments to distinguish between different ionization mechanisms relies on the fact that the ion momenta can, under certain conditions, provide information on the phase $\varphi = \omega t_0$ of the time-dependent laser field $\vec{E}(t) = \vec{E}_0 \sin(\omega t + \varphi)$ where (multiple) ionization took place, i.e. at what phase the ion was born. This becomes obvious within the classical treatment (Chen *et al* 2000, Feuerstein *et al* 2000, Moshammer *et al* 2000, Weber *et al* 2000) but is also inherent to all quantum calculations listed earlier. As mentioned before, a charged particle created with charge q and zero initial momentum at a time t_0 in a pulse that is long compared to the oscillation period ($\tau\omega \gg 1$; τ: pulse duration), gains a final drift momentum parallel to the laser field that only depends on the phase. At a

laser frequency of $\omega = 0.05$ a.u. and a field amplitude $E(t) = 0.18$ a.u. (1×10^{15} W cm^{-2}) a typical momentum resolution for singly charged ions of 0.1 a.u. would thus translate to a phase resolution of about 3% of a full optical cycle, i.e. to a time resolution of 80 attoseconds.

The 'tracing' of the phase by measuring the ion drift momentum is disturbed by any momentum transferred to the ion when it is created by a certain process like 'tunnelling', multi-photon absorption, 'rescattering' or excitation during rescattering plus subsequent tunnelling ionization of the excited electron. This leads to a reduced, nevertheless still sufficient phase resolution for the neon target, as is impressively demonstrated for NS double ionization: 'rescattering', where double ionization is due to an ionizing collision between the first electron being accelerated in the laser field and thrown back on its parent ion, mainly occurs at a phase where the electric field is close to zero, i.e. at $\omega t_0 = n \cdot \pi$ ($n = 1, 2, \ldots$) resulting in a large drift momentum of the doubly charged ion. In contrast, zero average drift momentum is expected to dominate for the other two NS double ionization mechanisms that have been proposed, 'SO' and 'collective tunnelling', since both most likely occur at maximum field strength, i.e. at phases $\omega t_0 = (2n + 1) \cdot \pi/2$ ($n = 0, 1, 2, \ldots$). The various mechanisms can only be distinguished in an unambiguous way by an ion momentum measurement alone, if the momentum transfer during creation of the ion by the one or other mechanism is less than the differences in ion drift momenta resulting from the average phase differences where the processes occur.

4.2.3. Correlated motion of electrons in the sequential and NS regimes. Subsequent experimental and theoretical work started to explore the correlated motion of the emitted electrons. In figure 18, for example, the correlated momenta of two emitted electrons are shown along the field direction ($k_{ezi} = P_{ei\parallel}$) for double ionization of Ar in the NS (3.8×10^{14} W cm^{-2}, upper panel) as well as in the sequential regime (1.5×10^{15} W cm^{-2}, lower panel), first published by Weber *et al* (2000b). Whereas the electrons were found to behave independently for sequential ionization, peaking at zero drift momentum (figure 18(*b*)), a strongly correlated behaviour is visible in the NS regime with a pronounced maximum for both electrons being emitted into the same hemisphere with very similar momenta (figure 18(*a*)). The authors explained the location of this maximum in a simple rescattering scenario where the returning electron excites the remaining ion which then is immediately field-ionized.

Pure collisional ionization during rescattering, essentially without the assistance by the laser field, seems to be responsible for Ne double ionization as illustrated in figure 19(*a*). As discussed by Moshammer *et al* (2003), for example, recollision happens at a well defined energy E^{recoll} and phase ωt_1 for a certain tunnelling phase of the first electron ωt_0. After recollision, each electron obtains a well defined and equal drift momentum of $P_{ei\parallel}^{\mathrm{drift}}(\omega t_0)$. In addition, they can share the excess energy $E^{\mathrm{ex}} = E^{\mathrm{recoll}} - I_{\mathrm{P}}$ (I_{P}: ionization potential). Neglecting the transverse energies of the electrons, energy conservation $P_{e1\parallel}^2 + P_{e2\parallel}^2 = 2E^{\mathrm{ex}}$ yields a circle with radius $(2E^{\mathrm{ex}})^{1/2}$ around the points $(\pm P_{e1\parallel}^{\mathrm{drift}}(\omega t_1), \pm P_{e2\parallel}^{\mathrm{drift}}(\omega t_1))$ as the maximum possible drift momentum combination. Considering all phases, the full curved lines in figure 19(*a*) for Ne were calculated to represent the classical boundaries, defined by momentum and energy conservation during rescattering, inside which all correlated events must occur.

While the comparison with the experimental data impressively shows that nearly all events are within these boundaries for the Ne target, the correlation pattern itself, however, with many electrons of quite similar longitudinal momenta, is not reproduced by calculations based on field-free electron-impact (e,2e) ionization dynamics. Similar to field-free collisions, unequal energy sharing between both emitted electrons has been calculated to be the most likely

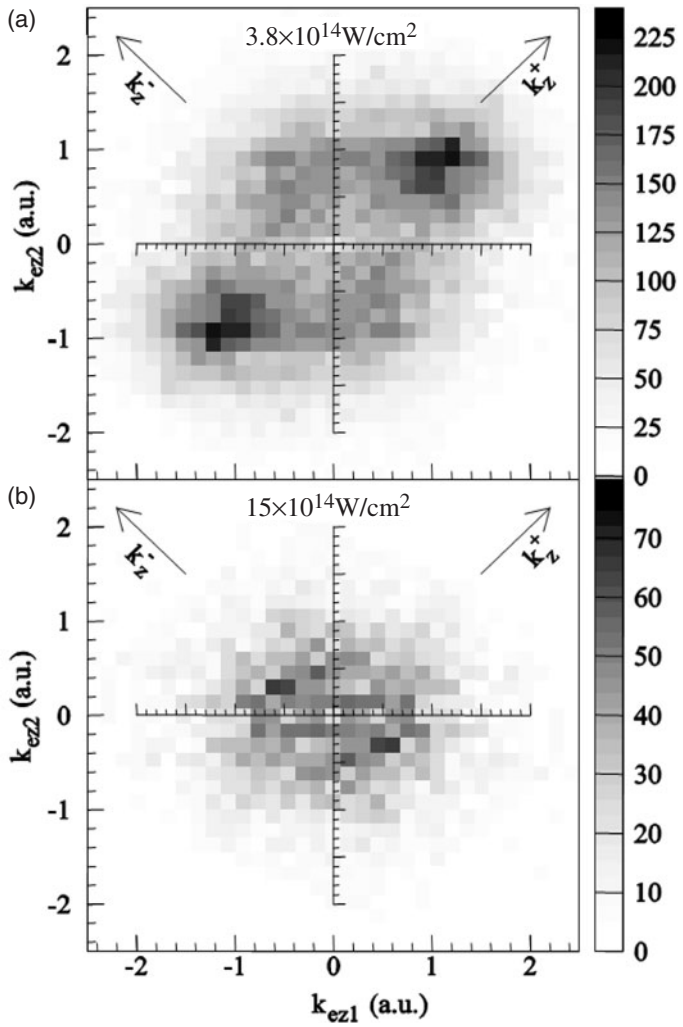

Figure 18. Correlated electron momenta along the polarization axis for double ionization of Ar at (*a*) 3.8×10^{14} W cm^{-2} (NS regime) and (*b*) 1.5×10^{15} W cm^{-2} (sequential regime) (from Weber *et al* (2000b)).

situation at not too low intensities, resulting in unequal final momenta for NS double ionization of Ne at 1×10^{15} W cm^{-2} (Goreslavskii and Popruzhenko 2001). Several other calculations, using a hard core form factor for the electron collision, solving the one-dimensional TDSE with correlated electrons, using an S-matrix approach (Becker and Faisal 2000, 2002) or semi-classical methods (Chen *et al* 2000) seem to be not in accordance with this experimental results. However, most theoretical work was devoted to helium whereas, until now, no such experimental data have been reported. Hence, final conclusions have to await further clarification. Nevertheless, recent calculations within the S-matrix approach by Becker and Faisal (2002) considering the SO amplitude separately resulted in two electrons emerging with very small momenta, i.e. strongly peaked at the origin in figures 18 and 19 and, therefore, support the above argument.

For both argon measurements shown in figure 18(*a*) (Weber *et al* 2000b) and figure 19(*b*) (Feuerstein *et al* 2001), the classically allowed direct ionization regime without any assistance

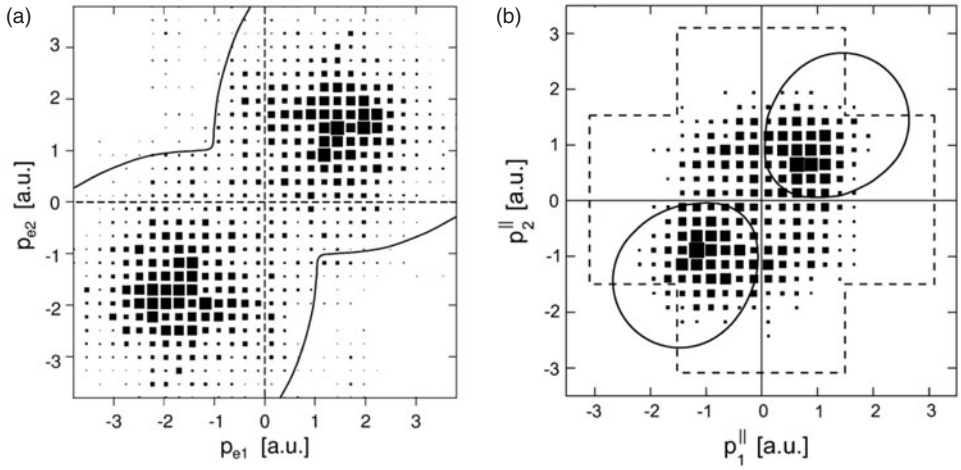

Figure 19. Correlated electron momenta along the polarization axis for double ionization of Ne (*a*) at 1×10^{15} W cm^{-2}. ——: kinematical boundaries for classical rescattering (from Moshammer *et al* (2003)). (*b*) Same as (*a*) for Ar^{2+} creation at 0.25×10^{15} W cm^{-2} (Feuerstein *et al* (2001)). ——: classical boundaries for recollision. - - - -: kinematical limit for excitation during recollision followed by field ionization in one of the subsequent laser cycles.

of the field shrinks significantly due to the lower intensity. At 2.5×10^{14} W cm^{-2} (figure 19(*b*)) it is completely restricted inside the full lines, i.e. to the quadrants with equal emission direction of both electrons with equal signs of both momenta. A large yield of electrons being emitted into opposite hemispheres has been interpreted as excitation during recollision of the still bound electron which then might be field-ionized in one of the subsequent maxima of the oscillating field (Feuerstein *et al* 2001). Note that direct field ionization 'at the instant' of recollision leads to emission into the same hemisphere (Weber *et al* 2000b). In contrast to Ne, the argon 3p to 3d excitation cross sections are large, making such a scenario quite likely as will be discussed in more detail in section 4.2.4. Observed momenta were within the classical kinematical limits (broken lines) for this process which tends to 'fill the valley' in between the two 'recollision maxima' in the ion-momentum distribution (projection onto the diagonal from the lower left to the upper right in figure 19, see Feuerstein *et al* (2001)).

In summary, even if the overall structure of novel experimental data obtained using reaction-microscopes strongly supports that rescattering is the dominant NS double ionization mechanism at least for the neon target, the correlated motion of both electrons in the field is far from being consistently understood theoretically.

4.2.4. Final state Coulomb repulsion and sub-threshold recollision at low intensity. Preferred emission of two electrons with nearly identical momenta along the field direction as observed in the experiment for neon targets seems to contradict electron-repulsion in the final state. Quantum mechanical calculations solving the one-dimensional TDSE on a grid with fully correlated electrons in the helium atom (figure 20 left) yielded a minimum for equal $P_{ei\parallel}$ (Lein *et al* 2000). Here, however, the Coulomb repulsion is certainly overestimated due to the one-dimensionality of the model. Experimentally, one can artificially reduce the dimensions in the final state by the requirement, that the final transverse momentum of one of the electrons—and thus, in an (e,2e) scenario also of the second one—is small. Then, as illustrated in figure 20 (right), the maximum along the diagonal with equal $P_{ei\parallel}$ was found to be significantly depleted

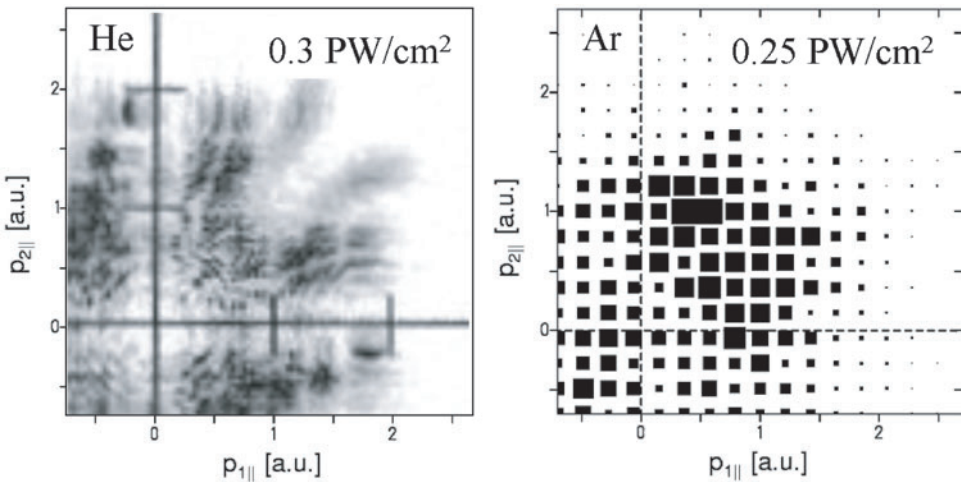

Figure 20. Correlated momenta of electrons for He^{2+} (left, theory by Lein *et al* (2000)) and Ar^{2+} (right, experiment (Moshammer *et al* (2002)) creation at indicated laser intensities. Experiment: the transverse momentum of electron 1 is larger than 0.5 a.u..

(Weckenbrock *et al* 2001, Moshammer *et al* 2002). The electrons are restricted in their transverse motion and, consequently, repel each other more strongly longitudinally.

Very recently, recoil-ion momentum distributions have been measured for Ar^{2+} and Ne^{2+} ions at very low intensities extending down to maximum recollision energies $E^{\mathrm{recoll}} = 3.17 \cdot U_{\mathrm{P}}$ well below the ionization potential I_{P} of GS Ar^{+} or Ne^{+} ions in a field-free environment (Eremina *et al* 2003). In figure 21, they are shown for various ratios of recollision energies to ionization potentials $E^{\mathrm{recoll}}/I_{\mathrm{P}}$ ranging from values larger than one, where classical field-free recollision impact ionization is possible, to $E^{\mathrm{recoll}}/I_{\mathrm{P}}$ as low as 0.5, where the energy of the re-colliding electron is well below threshold. The smooth transition between both regimes observed in the ion rates has always been an argument against a simple recollision scenario to explain NS double ionization. The observed momentum distributions for Ar, Ne and He at similar $E^{\mathrm{recoll}}/I_{\mathrm{P}}$ strongly differ from each other indicating first, that different mechanisms are active below and above threshold for the various species. Whereas the valley between the maxima is more and more filled for Ar, finally displaying one single maximum at zero drift momentum for $E^{\mathrm{recoll}}/I_{\mathrm{P}} = 0.5$, a clear double peak structure remains for Ne even at $E^{\mathrm{recoll}}/I_{\mathrm{P}} = 0.7$. At the same time there is only one single peak for the helium target directly at threshold, evolving only slowly into a quite weak double hump structure at relatively high intensities of $E^{\mathrm{recoll}}/I_{\mathrm{P}} = 2.3$.

While for argon the transition can be understood in terms of the increased importance of excitation during recollision followed by field ionization at lower intensities along the lines discussed above, smoothly 'filling the valley', the pronounced sub-threshold double-hump structure for neon double ionization was explained as increased importance of recollision at phases of the field, where it is not zero (Eremina *et al* 2003). Here, the effective ionization potential of Ne^{1+} is lowered to such an extent that the re-colliding electron can still ionize the Ne^{+} ion assisted by the field. In such a scenario, increasingly, but smoothly, different but well-defined and narrow recollision phase intervals become important leading to well defined but lower recoil-ion momenta and, thus, to a pronounced double-peak structure.

Helium (left row in figure 21) finally, behaves very much like argon with a single peak at zero longitudinal momentum even above the recollision threshold making the whole scenario

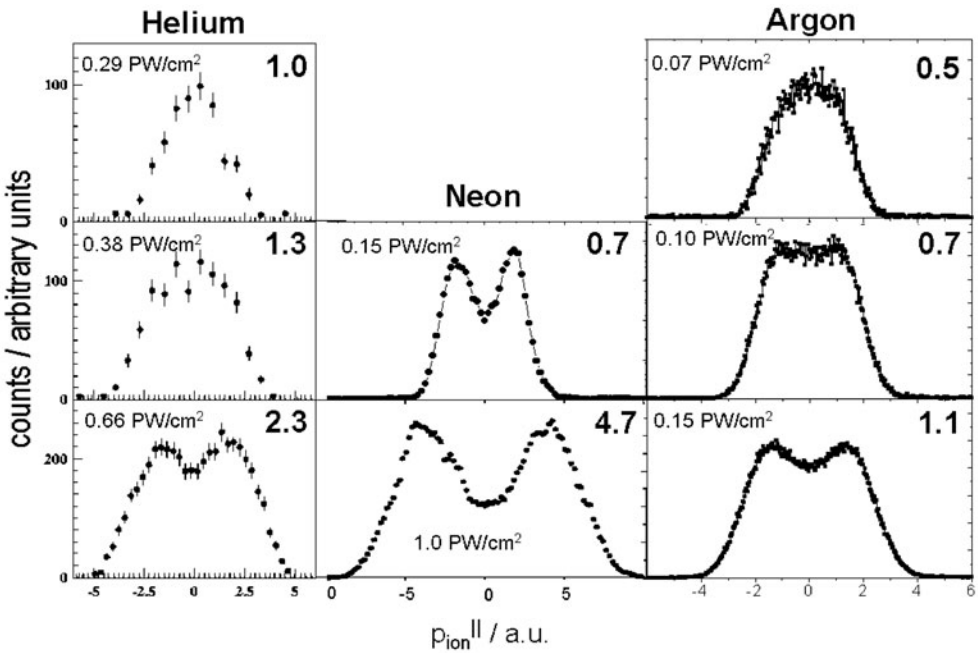

Figure 21. Ion momentum distributions along the laser polarization direction for He (Weber *et al* 2000), Ne (Moshammer *et al* 2000) and Ar (Eremina *et al* 2003). Respective intensities are indicated in each panel. Upper right number in the panels: ratio of recollision energy to the ionization potential of the singly charged ion without field.

quite confusing at first glance. It has been shown recently (Bastos de Jesus *et al* 2003), however, that the different behaviour of the various rare gas targets can be consistently explained in a quantitative way by taking into account the ratio of electron impact excitation to ionization cross sections for the singly charged ions. It turns out, that neon plays a special role in that this ratio is exceptionally small compared to the other elements. Accordingly, excitation during recollision followed by field ionization of the excited electron is a small channel compared to direct electron impact ionization during rescattering and, thus, the double hump structure prevails to intensities even below the field-free recollision threshold. The quantitative interpretation given by Bastos de Jesus *et al* (2003) was based on estimates of the above ratio on the basis of empirical models used in plasma physics taking into account all recollision energies and relative intensities, calculated from the tunnelling phases for the electron weighted with the tunnelling probability, and assuming that the excitation/field-ionization channel leads to a maximum of the recoil-ion momentum distributions at zero.

Nevertheless, more experimental results for helium, which is the only system where fully quantum-mechanical calculations might be expected within the near future (Parker *et al* 2001) are urgently needed.

4.2.5. Transverse momentum exchange. The electron and ion momenta in the direction of the laser polarization which have been discussed so far are mainly a result of the acceleration in the field. This is what allows one to use them to gain insight into the time evolution of the ionization process. The momentum components of all particles perpendicular to the field in contrast are solely a result of the few-body momentum exchange. Therefore, the subtleties of the

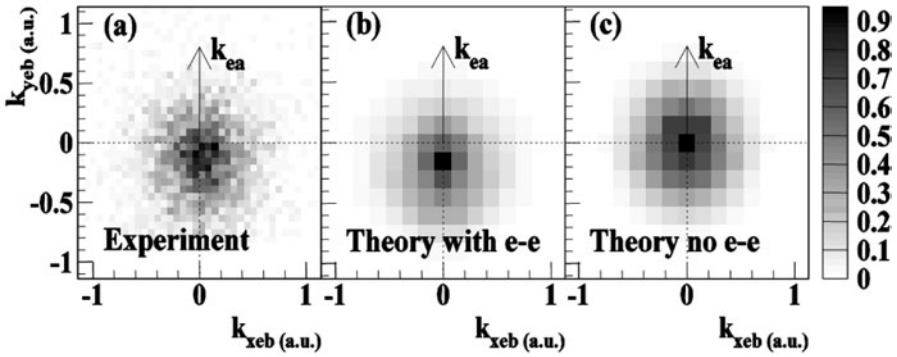

Figure 22. Electron momentum distribution in the plane perpendicular to the polarization for double ionization of Ar at $1.9 \times 10^{14}\,\mathrm{W\,cm^{-2}}$. The direction of the first electron is indicated by the arrow, the perpendicular momentum of the second electron is shown. The data are integrated over the momentum components in field direction. (*a*) Experiment, (*b*) theoretical results including e–e momentum exchange in the recollision and e–e repulsion after the recollision. (*c*) Theoretical results not including final state repulsion (from Weckenbrock *et al* (2003)).

momentum exchange in the recollision event are in the perpendicular plane, not masked by the large momentum transfer from the field. Figure 22 shows the momentum correlation between the two electrons in the plane perpendicular to the polarization (Weckenbrock *et al* 2003). The first electron is emitted upwards along the arrow; the momentum of the second electron is shown. Both electrons are found to be emitted slightly back-to-back. The momentum distribution of the doubly charged ion is very similar and also slightly opposite to one electron (not shown). At first glance one might argue that such behaviour is simply a result of a binary momentum exchange between the rescattered and the second electron to be kicked out. Astonishingly, S-matrix calculations proof this simple mechanism wrong and suggest that the back-to-back emission in the perpendicular plane is not a result of the binary momentum exchange in the recollision event but is created after the second electron is set free by the long range final state interaction. Figure 22(*b*) shows the full S-matrix calculation including binary momentum exchange and final state interaction while in figure 22(*c*) the final state interaction is neglected but the recollision momentum exchange is still active. The same calculation however does not reproduce the observed ion momenta (not shown, see Weckenbrock *et al* (2003)). At present, the study of the transverse momentum exchange highlights once more how far from final conclusions the dynamics of NS double ionization really is.

4.3. Electron impact ionization

While for ion impact kinematically complete experiments for single ionization could be realized only with the advent of reaction-microscopes, for electron impact the first so-called (e,2e) experiments were already performed in the late 1960s by Ehrhardt *et al* (1969) and others. These and the following numerous (e,2e) experiments contributed substantially to our understanding of the dynamics of the three-body Coulomb problem. On the other hand, due to the small acceptance angle, this technique reaches its limits for multiple coincidence experiments as they are required for the study of double ionization, excitation–ionization and molecular fragmentation. This is also the case for experiments requiring short pulsed projectile beams as, e.g. the study of electron collisions which take place in strong light fields. The light intensities required for such laser-assisted collisions ($I > 10^{12}\,\mathrm{W\,cm^{-2}}$) can be realized only by pulsed laser beams.

Therefore, despite the huge amount of data which has been collected using conventional electron spectroscopy the application of the reaction-microscope enables a variety of new and unprecedented experiments for electron collision processes. This is due to the large phase space acceptance of the spectrometer, the strongly relaxed beam time restrictions for simple electron sources compared to synchrotron or ion beam facilities and the pulsed-mode operation of the projectile beam which allows synchronization with other beams as, e.g. short laser pulses. In the following, a few examples are presented which have been realized recently or are under way.

4.3.1. Single and double ionization. The first measurements using RIMS for electron impact single and double ionization were performed by Jagutzki *et al* (1996). The electrons in the final state were not detected. From the good agreement of the recoil-ion momentum distribution with experimental and theoretical electron momentum distributions for single ionization, the authors concluded that collisions with small momentum transfer dominate. For double ionization the recoil-ion momentum distribution was observed to be much broader. This was attributed in the first instance to the broader two-electron Compton profile. The authors pointed out that kinematically complete measurements for double ionization (so-called (e,3e) experiments) would become feasible if two final state electrons would be observed in coincidence with the recoiling ion. Such experiments were realized in the following using a reaction-microscope for the additional detection of one or two slowly ejected electrons for single or double ionization, respectively (Dorn *et al* 1999).

Using the combined recoil-ion and electron momentum spectrometer which is briefly described in section 3.1 for electron projectile beams is not straight forward. In contrast to essentially all other projectiles used in connection with reaction-microscopes (ions, synchrotron and laser photons) electrons are strongly deflected by the magnetic field which serves to guide the secondary electrons to the detector. The configuration with the projectile beam collinear to the magnetic field lines which would be optimal for guiding the projectile electron beam into the target is not practicable since in this case the primary electrons would impinge on the electron detector after passing the target. Despite the small beam current which is in the order of 60 pA, this would correspond to a few hundred MHz count rate, a value far beyond the dynamical range of the detector. Therefore, a different operation mode was used where the primary beam emitted on the apparatus axis is deflected off the axis and passes through a full cyclotron revolution before it returns to the axis in the target volume (Dorn *et al* 2002). After another half of a complete revolution it has the maximum deviation from the spectrometer axis and therefore it passes by the electron detector and is dumped in a Faraday cup. While this arrangement enables experiments for electron impact using the reaction-microscope, the projectile velocity determines the required magnetic field strength. Thus, the highest energy of the ejected electrons which is accepted over the full solid angle is restricted. For $E_0 = 2000$ eV, the required field of $B = 12$ Gauss results in full efficiency for electrons up to 25 eV only. Nevertheless, with the restriction that free zooming of the fragment particle imaging properties is not possible, kinematically complete experiments for electron impact can be performed. In future, this limitation will be removed by using an electron detector with a central bore which allows one to reach the ideal geometry for the projectile beam trajectory which will be on the axis of the magnetic field $\vec{B}$ and therefore $\vec{B}$ and the projectile energy E_0 will be decoupled.

The large phase space acceptance of the apparatus is demonstrated in figure 23 for single ionization. In accordance with most (e,2e) experiments performed with conventional electron spectrometry only events with co-planar geometry are displayed for which the ejected electron moves in the scattering plane defined by the incoming and scattered projectile. The cross section is plotted as function of the electron emission angle Θ_b (x-axis) and, simultaneously,

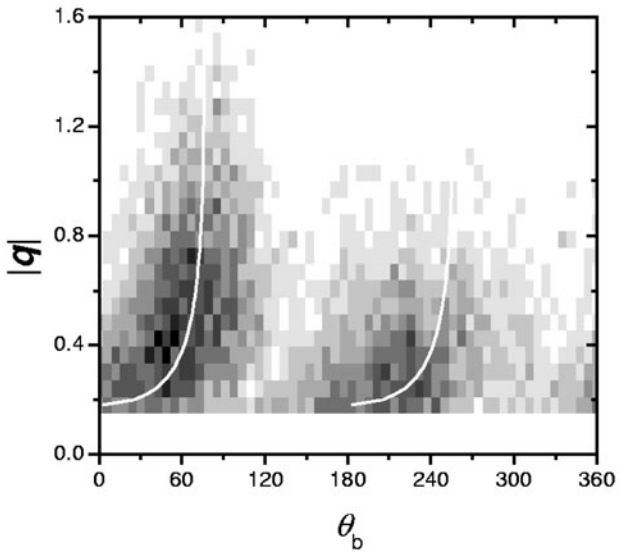

Figure 23. Triple differential cross section (TDCS) in co-planar scattering geometry for single ionization of helium by 500 eV electron impact as a function of the emission angle Θ_b and the momentum transfer $|\vec{q}|$ of the ionized electron ($E_b = 5$ eV). White curves: direction of the momentum transfer $|\vec{q}|$ (left) and $-|\vec{q}|$ (right).

as a function of the momentum transfer $|\vec{q}|$ (y-axis). This representation nicely reveals the behaviour of the so-called binary and the recoil peak, namely their magnitude and angular position in dependence on the momentum transfer. The binary peak around $\Theta_b \approx 60^\circ$ is generally attributed to a binary knock-out collision where the target electron is emitted along $\vec{q}$, while for the recoil peak the ejected electron undergoes an additional scattering process in the ionic potential and is emitted into the backwards direction $-\vec{q}$ around 240°. The kinematical shift of the cross section maxima to smaller Θ_b for decreasing $|\vec{q}|$ is visible as well as the known behaviour, namely that the recoil peak decreases much faster in intensity compared to the binary peak for increasing momentum transfer. Although the data shown represent only a small fraction of the full final state phase space covered experimentally it would constitute a large number of experimental runs for a conventional set-up. Furthermore, these do not allow covering the full angular range of Θ_b from 0° to 360°. In figure 24, the momentum distribution of the ejected electron is presented for fixed momentum transfer of $|\vec{q}| = 0.6$ a.u. revealing a strong binary emission peak along $\vec{q}$ and a weaker recoil peak in the opposite direction. The momentum distribution around the tip of the arrow indicating the size and direction of the momentum transfer represents essentially the bound electrons Compton profile.

The logical next step which is of prime importance for the understanding of the correlated electron dynamics is the kinematically complete investigation of electron impact double ionization. The first (e,3e) experiment was performed by Lahmam Bennani *et al* (1989) for the argon target. First experiments for the fundamental helium target were performed essentially simultaneously with conventional electron spectrometry for $E_0 = 5500$ eV by Taouil *et al* (1998) and with the reaction-microscope by Dorn *et al* (1999) for $E_0 = 3000$ eV. While the former, conventional experiment was restricted to a single projectile scattering angle close to the optical limit ($|\vec{q}| = 0.24$ a.u.), to a particular energy of the ejected electrons e_b and e_c ($E_b = E_c = 10$ eV) and to co-planar scattering geometry, the latter experiment allowed a global view of the final state momentum space. While the statistics of these first measurements did not allow definite statements for the fully, fivefold differential cross section (FDCS), new

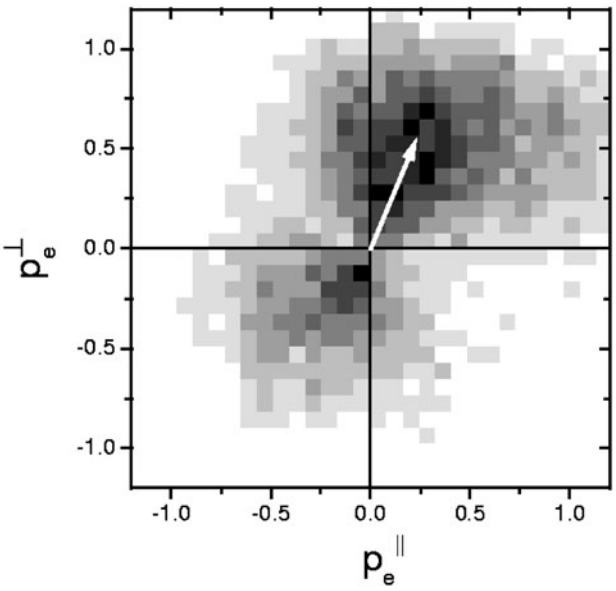

Figure 24. TDCS for $|\vec{q}| = 0.6$ a.u. (direction of $\vec{q}$ indicated by an arrow) as a function of the longitudinal and transversal momentum of the ejected electron.

insight into the direct impact (DI) collision could be obtained for partially integrated cross sections. Examining the angular correlation of the ejected electron pair, both experiments could confirm close similarities to photo double ionization for small momentum transfer with the most probable relative emission angle of 135°. For larger $|\vec{q}|$, smaller relative angles of the ejected electron pair were observed by Dorn *et al* (1999) which was interpreted as a signature of a first order binary collision process. In subsequent experiments for $E_0 = 2000$ eV ($v = 12$ a.u.) FDCSs could be obtained which allowed a detailed examination of the cross section and quantitative tests of theoretical calculations (Dorn *et al* 2001, 2002). For $v = 12$ a.u. the projectile generally can be treated as a small perturbation. On the other hand, the ionized electrons most probably are slow and, therefore, they strongly interact with each other and the residual ion. The examination of the FDCS pattern reveals that the subtle details of this correlated emission strongly depend on the amount of momentum $|\vec{q}|$ transferred by the projectile to the target. In the optical limit, namely for small projectile scattering angle and therefore small $|\vec{q}|$, the cross section pattern is dominated by dipole selection rules and the strong Coulomb repulsion between the electrons. This is illustrated in figure 25(*a*) where the FDCS is plotted for $|\vec{q}| = 0.5$ a.u.. Events are chosen where the ionized electrons have energies E_b and E_c of 5 eV each and move in the projectile scattering plane. The FDCS is plotted versus the emission angles Θ_b and Θ_c of the ejected electrons with respect to the incoming projectile beam forward direction. The solid circular lines in the diagrams indicate the angular range accessible by the apparatus. For angular combinations outside the circles the time difference between the arrival of the electrons on the detector is less than the detector dead time of 15 ns and, therefore, the second electron is not registered.

The cross section shows a pronounced structure with four strong peaks indicating that particular angular combinations (Θ_b, Θ_c) are strongly favoured. The agreement with photo-double ionization data shown in figure 25(*b*) is very good if the light polarization axis $\vec{E}$ is aligned along the corresponding momentum transfer direction $\vec{q}$. Peak (A) in figure 25(*a*) corresponds to emission as sketched in figure 25(*b*) with the sum momentum of the ionized

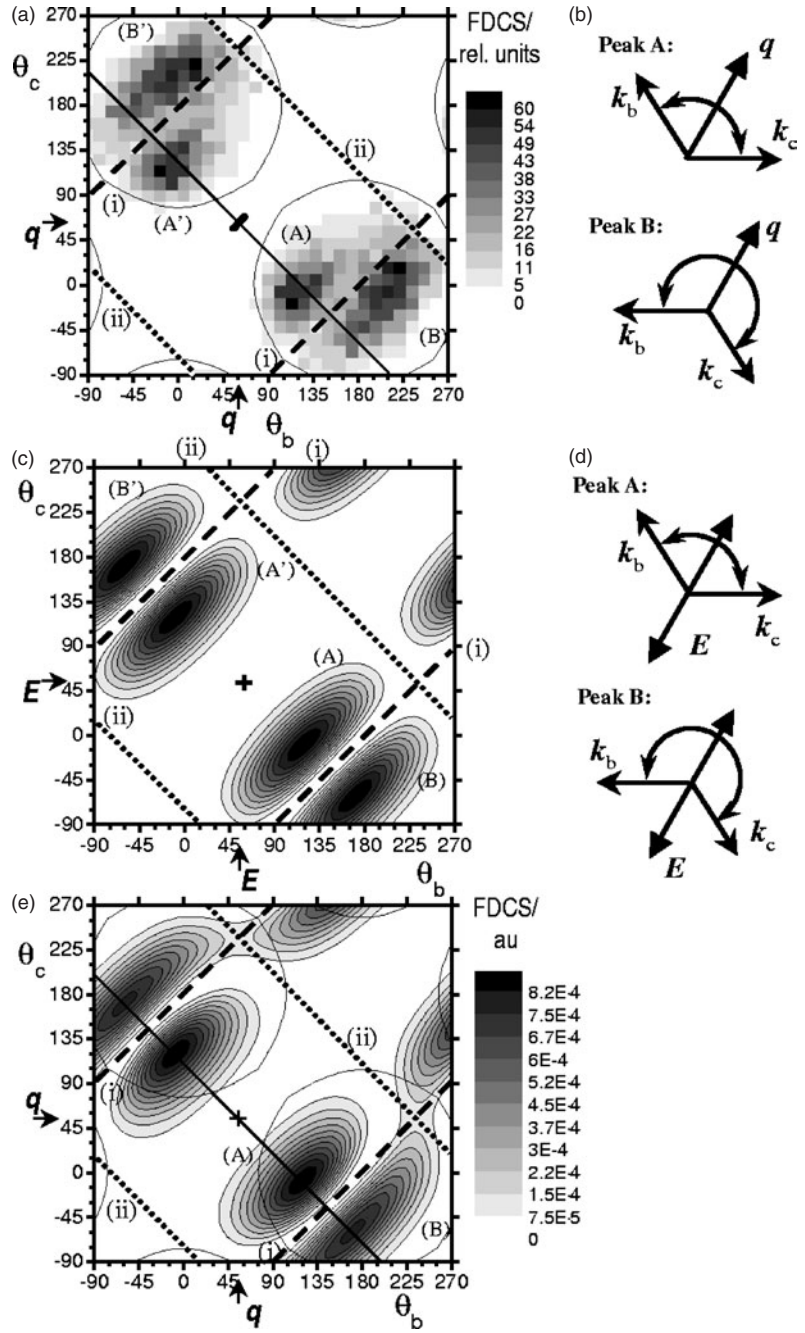

Figure 25. FDCS in co-planar scattering geometry as a function of the ejected electron emission angles Θ_b and Θ_c relative to the primary beam forward direction. The ejected electron energies are $E_{b,c} = 5 \pm 2$ eV. (*a*) Experimental cross section for $E_0 = 2$ keV, $|\vec{q}| = 0.5 \pm 0.2$ a.u.. (*b*) The electron emission configurations for the cross section maxima (A) and (B) in (*a*). (*c*) Photo double ionization cross section for $E_{b,c} = 5$ eV. (*d*) The electron emission configurations for the cross section maxima (A) and (B) in (*c*). (*e*) CCC calculation for $|\vec{q}| = 0.5$ a.u.. The direction of the momentum transfer $\vec{q}$ is marked by arrows. In both diagrams the angular range which is not affected by the experimental detector dead time is encircled by solid lines (see text) (from Ullrich and Shevelko (2003)).

electrons going along $\vec{q}$. Respectively, peak (B) corresponds to emission with the sum momentum of the electrons being reversed. For equal energy sharing the cross section is symmetric with respect to the main diagonal of the diagram since both electrons are indistinguishable. Dipole selection rules suppress electron emission along the dashed and dotted lines. In addition, electron–electron repulsion gives rise to the broad cross section minimum around $\Theta_b = \Theta_c$. Deviations of the electron impact data from the strict symmetries visible in figure 25(*b*) for photo double ionization are due to the finite momentum transfer $|\vec{q}|$ which can lead to differences in shape and intensity of peaks (A) and (B). The shift of peak (B) to the top right part of the diagram is due to contributions of higher order collisions.

While various successful theoretical models exist to describe photo double ionization, which has been attributed partly to the strong restrictions imposed by selection rules (Briggs and Schmidt 2000), theory is in a far less developed shape for electron impact double ionization. In figure 25(*e*) theoretical results obtained with the CCC approach are shown (Dorn *et al* 2001). While this method treats the interaction of the two slowly ejected electrons non-perturbatively, the projectile–target interaction is described in first order by applying the first Born approximation (FBA). Comparing with the experimental cross section the agreement is reasonably good in shape and in the relative peak heights. Clearly, the finite momentum transfer gives rise to higher multiple contributions to the cross section which can be identified as a finite cross section for angular combinations where the dipole selection rules would strictly enforce a zero value, namely at the intersection points of the dashed and dotted lines. Disagreement between experiment and theory is present for the node for back-to-back emission (dashed lines) which, differently from theory, is partially filled in the experimental data. A further disagreement is the shift of the peaks marked (B) to larger angles for both emitted electrons. As mentioned above this can be explained by higher order projectile–target interactions which are not within the scope of a first Born treatment.

The fragmentation pattern is strongly modified if collisions with larger momentum transfers are investigated where dipole selection rules do not act (Dorn *et al* 2002). For $|\vec{q}| = 2$ a.u. and low energies of $E_b = E_c = 5$ eV the repulsion of the ejected electrons is dominant and gives rise to a Wannier-like back-to-back emission. For larger energies of $E_b = E_c = 20$ eV a cross section peak is observed for conditions where the Bethe ridge condition is fulfilled: the full momentum transfer $\vec{q}$ is carried by the ejected electron pair while the residual ion has only little momentum. This peak was attributed mainly to the TS1 ionization mechanism where the electron ionized in a first binary collision with the projectile collides on the way out of the atom with the second electron. This picture is also consistent with the observed most probable relative ejection angle close to 90°.

For a quantitative comparison with theory, a particular cut of the experimental data is shown in figure 26 where the emission angle of one ejected electron ($E_b = 25$ eV) is fixed to $\Theta_c = 0°$ and the emission angle of the second electron ($E_c = 5$ eV) is scanned (Dorn *et al* 2002a). The calculations shown, the CCC theory (solid line) and the calculation using the analytical 3C or BBK wave function (dashed line) differ strongly from each other and only the CCC calculation is in fairly good agreement with the experiment. This demonstrates that the (e,3e) reaction, in particular in the large momentum transfer regime where no dipole selection rules act, is a critical test for theory.

From the above discussion the expectation is confirmed that fast collisions can be understood essentially in terms of a first order projectile–target interaction with only minor contributions from higher order processes. This is expected to change for reduced projectile velocity and therefore increased perturbation. Indeed, results for 500 eV electron impact ($v = 6$ a.u.) show strongly modified cross sections in particular for low momentum transfer (Dorn *et al* 2003). In figure 27, an example is shown for $|\vec{q}| = 0.6$ a.u. and the same energies

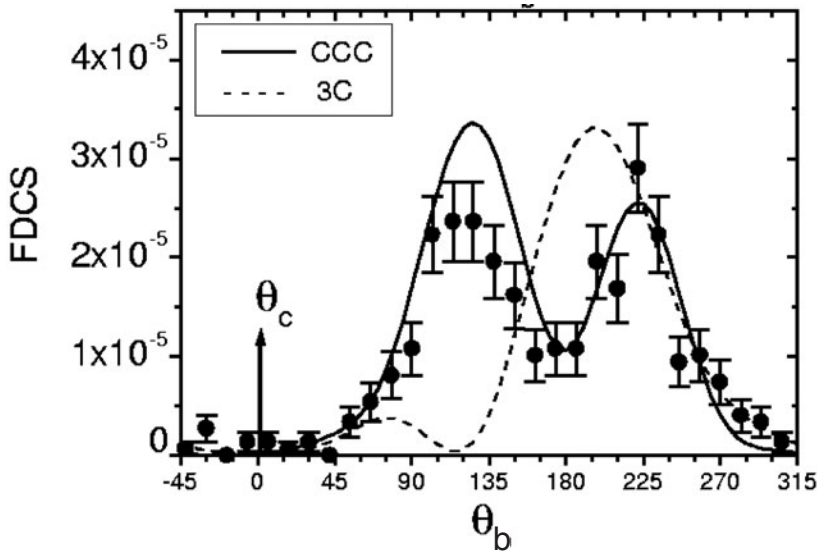

Figure 26. FDCS for $E_0 = 2\,\mathrm{keV}$, $|\vec{q}| = 2\,\mathrm{a.u.}$ and fixed emission angle $\Theta_c = 0^\circ$ ($E_b = 5\,\mathrm{eV}$, $E_c = 25\,\mathrm{eV}$). ——: CCC calculation. - - - -: calculation using the 3C final state wave function (from Dorn *et al* (2002a)).

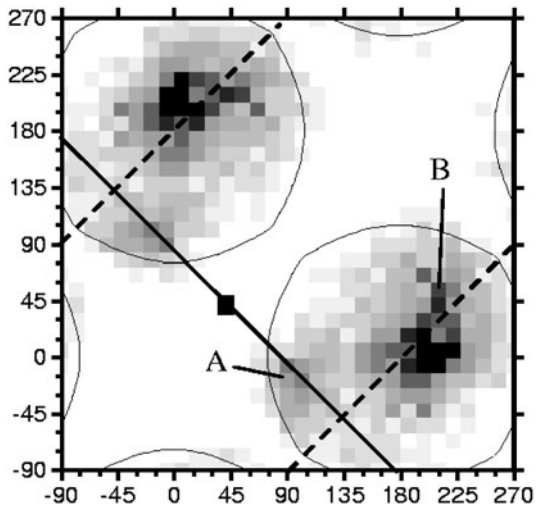

Figure 27. FDCS for DI by $E_0 = 500\,\mathrm{eV}$ electron impact and $|\vec{q}| = 0.7 \pm 0.2\,\mathrm{a.u.}$ but otherwise unchanged conditions as for figure 25(*a*). The full square on the diagonal line indicates the momentum transfer direction (from Dorn *et al* (2003)).

of the ejected electrons as for figure 25(*a*) ($E_{b,c} = 5\,\mathrm{eV}$). There is no resemblance to the photoionization pattern of figure 25(*b*) any longer and the symmetry with respect to the momentum transfer direction, present for fast collisions, is completely lost. This indicates that second order collisions or the so-called two-step 2 (TS2) mechanism is important. Therefore, any calculation describing the collision in first order must fail. First, attempts to reproduce these data with a CCC calculation including the second Born amplitude are encouraging (Dorn *et al* 2003). On the other hand, it is to be expected that in general,

a perturbation expansion of the exact transition amplitude fails if the higher order contributions become of comparable magnitude to the first order contribution. In future, investigations of (e,3e) reactions in the non-perturbative regime are envisaged where all three final state electrons have comparable velocity. Then, the full complexity of the four body dynamics is expected to show up.

4.3.2. Ionization-excitation. Simultaneous excitation of one target electron and ionization of a second electron in many aspects resembles the double ionization process. In both reactions, electron correlation and higher order projectile–target interaction play a dominant role. On the other hand, for excitation–ionization the final state contains only two continuum electrons, compared to three for double ionization. Therefore, the theoretical treatment is much simpler since, in particular for very asymmetric energy sharing reactions, calculations can neglect the long range final state interaction of the continuum electrons and focus on modelling the short range collision dynamics in a more accurate way. On the experimental side, up to now there has been no 'perfect' (e,γ 2e) experiment (Balashov and Bodrenko 1999), which would imply determining the ionization process, kinematically complete, and measuring simultaneously the excitation amplitudes and their relative phases for the excited ionic state. For the helium target such an experiment could be performed for the $He^{*+}(np)$ final state if both continuum electrons and the photon emitted in the decay are detected. In addition, the measurement of the polarization parameters or of the angular distribution of the photons is required. So far such a triple coincidence detection was not feasible and experiments were restricted to recording only two final state particles, either two electrons (Dupré *et al* 1992, Avaldi *et al* 1998) or one electron and the photon (Hayes and Williams 1996, Dogan and Crowe 2002), integrating over the observables of the particle which had not been observed.

Recently, a triple coincidence (e,γ 2e) experiment has been performed, using a reaction-microscope that was additionally equipped with two large area MCP detectors for the detection of VUV photons (Dorn *et al* 2002a). The following reaction was investigated:

$$e^-(E_0 = 500\,\text{eV}) + He(1s^2\,{}^1S) \rightarrow 2e^- + He^{+*}(np\,{}^2P) \rightarrow 2e^- + He^+(1s\,{}^2S) + \gamma(\lambda \leqslant 30.4\,\text{nm}).$$

Experimentally, a slowly ejected electron, the recoiling singly charged ion and the fluorescence photon emitted by the residual ion were detected in a triple coincidence. The experimental resolution for the Q-value of the reaction did not allow resolution of the different excited np-states. Thus, despite the fact that the $He^+(2p)$ state gives the main contribution with more than 80% relative probability, the experiment is so far not fully resolved where the final state is concerned. For reduced projectile energies at around 100 eV which are envisaged for the future, the Q-value resolution will allow us to separate the 2p state from higher states.

In figure 28, transversal momentum distributions for electrons and ions are shown for the (e,γ 2e) reaction and compared with corresponding distributions for (e,2e) and (e,3e) processes, respectively. All three experiments have been performed for $E_0 = 500$ eV and with identical values for the extraction fields at the reaction-microscope.

While the observed recoil-ion momentum distribution for (e,γ 2e) is very similar to the one for (e,3e), which one might have expected, significant differences occur in the electron momentum distribution which is closer to the one for (e,2e). This clearly indicates, that different dynamic mechanisms dominate for (e,3e) compared to (e,γ 2e) which is quite surprising. Presently, the data are further analysed in order to extract higher differential cross sections which might possibly clarify the reasons for the observed differences.

4.3.3. Laser-assisted collisions. Laser-assisted collisions between atoms and charged particles are interesting from different points of view: first, as discussed in section 4.2, these

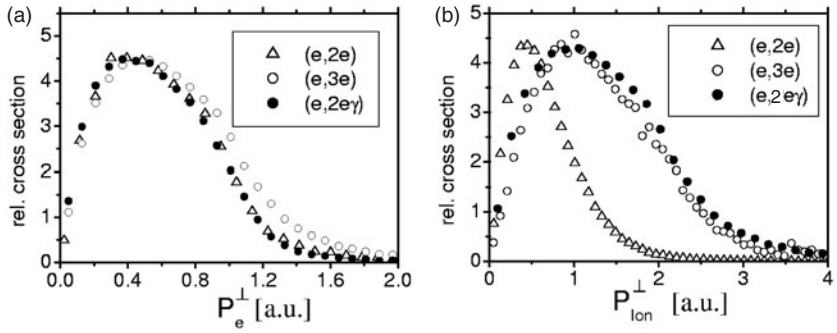

Figure 28. Transversal momentum distributions of the ionized electrons (*a*) and the recoiling ions (*b*) for single ionization (e,2e), excitation–ionization (e,γ2e) and double ionization (e,3e).

processes play a central role in the double ionization reaction induced by ultra-short fs-laser pulses in the NS intensity regime. Here, an electron ionized in the laser pulse is accelerated in the oscillating electric field and re-collides with the parent ion giving rise to the emission of a second target electron. It is expected that laser-assisted (e,2e) experiments where the collision parameters are under full control will give detailed insight into this process. Second, it might be possible to control the interaction pathways in ion–atom collisions, i.e. to enhance the population of favoured final states and to suppress the production of undesired ones by a suitable choice of the laser parameters (Kirchner 2002). This might be a first step to controlling molecular reactions. Third, there are a number of theoretical studies aiming at modelling the laser-assisted ionization process in different approximations (see, e.g. Khalil *et al* (1997)). Phenomena which have to be considered are the dressing of the initial and final target states as well as the interaction of the charged continuum particles with each other and the laser field. The electromagnetic field can act as a reservoir of energy and its polarization vector introduces a new axis of symmetry. As a result, the (e,2e) cross sections for laser-assisted collisions differ strongly in shape and magnitude from the field-free cross sections as predicted in several theoretical papers on this topic (Khalil *et al* 1997, Makhoute *et al* 1999, 2002). On the other hand, little is known about the validity and the accuracy of these treatments simply due to the lack of experimental data.

Experiments with the aim of realizing such investigations are presently under way using a reaction-microscope. In this set-up a pulsed Nd : Yag laser beam ($\lambda = 1064$ nm, pulse duration $\tau_l = 7$ ns, $I \approx 10^{12}$ W cm^{-2}) has been synchronized in time and collinearly superimposed in space with the pulsed projectile electron beam ($E_0 = 1000$ eV, $\tau_e = 1.5$ ns) at the position of a target gas jet. By alternating measurements with and without the laser beam, kinematically complete data can be obtained for the laser-assisted process as well as for the field-free case. As an example in figure 29 the longitudinal momentum distribution of the residual ions is shown for electron impact ionization of helium. Compared to the field-free situation without the laser field the cross section for laser-assisted collisions is increased significantly at small momentum transfers for $|P_\parallel| < 0.4$ a.u.. On the other hand, for $|P_\parallel| > 0.4$ a.u. the cross section is unchanged. This can be understood in terms of a two-step process where the helium atom is excited in a first step by electron impact to He*(1s nl) states and the excited state is subsequently ionized by the laser radiation with a photon energy of 1.1 eV, a process which has been discussed and seems to strongly contribute in double ionization of argon and helium in strong laser fields (see section 4.2). For this photon energy, ionization by a single photon is possible for $n = 4$ and higher principal quantum numbers. Since the longitudinal ion momentum distribution essentially reflects the Compton profile of the bound electron,

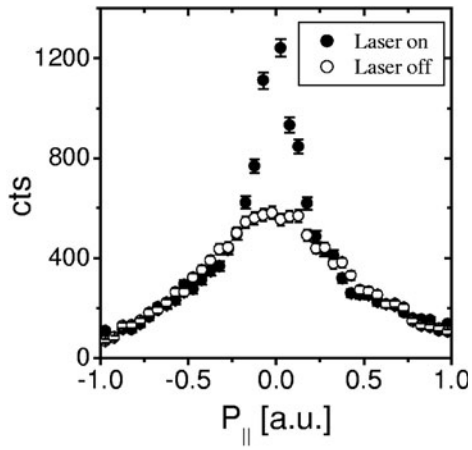

Figure 29. Cross section for electron impact ionization of helium differential in the longitudinal momentum of the residual He^+ ions parallel to the incoming projectile beam for the laser beam on and off.

the narrow momentum distribution is consistent with photoionization of excited states. The transversal momentum distribution, on the other hand, is observed to be broad due to the momentum transfer of the scattered projectile.

This two-step process might open the novel possibility of investigating even excitation processes in a kinematically complete way using the reaction-microscope by controlled ionization of the excited state after its creation. For the highest intensities reached so far of 4×10^{12} W cm^{-2}, the relative increase of the ionization probability with the laser beam on is about a factor of two higher than expected for the discussed two-step model. This can be due to high-intensity phenomena which are the objects of interest of this investigation. More detailed results are expected if ejected electron momentum distributions are analysed in addition to the ion momentum distributions.

4.4. Ion collisions

Originally RIMS and now reaction-microscopes have been developed with the intention of investigating the dynamics of ion–atom collisions. Therefore, an enormous amount of experimental data exists using ions as projectiles. From the kinematical point of view the most simple reactions are bound to bound one-electron transitions from the target to the projectile (single electron capture) because in this case only two particles are in the final continuum state. The first high-resolution capture measurements, where the finally populated electronic states of the projectile could be distinguished by means of a recoil-ion longitudinal momentum measurement, succeeded in the mid 1990s (Mergel *et al* 1995, Wu *et al* 1995, Cassimi *et al* 1996) using a cold supersonic jet as a target (COLTRIMS). Since then the technique has been improved considerably with respect to both the quality of the target and the spectrometer performance (see also Dörner *et al* (2000)). As a result, capture measurements with unsurpassed recoil-ion momentum resolutions have been reported using atoms trapped in a MOT as a target (Flechard *et al* 2001, Turkstra *et al* 2001, van der Poel *et al* 2001). Recently, results for electron capture accompanied with excitation of a bound electron of either the target (Weber *et al* 2001) or the projectile (Kamber *et al* 2000, Fischer *et al* 2002) have been published. With highly charged projectiles at low collision velocities (below 10 keV u^{-1}) the simultaneous capture of several electrons by the projectile contributes considerably to the total

cross section. Double and triple electron capture from the target into bound (excited) states of the projectile were studied (for recent results see, e.g. Flechard *et al* (2001a), Zhang *et al* (2001), Abdallah *et al* (1998a)) or even in coincidence with Auger-electrons, which are emitted from the highly excited projectile after the collision (Hasan *et al* 1999).

At high velocities (above $100\,\mathrm{keV\,u^{-1}}$) electron capture is often associated with the simultaneous ionization of another target electron (TI). Here, the application of COLTRIMS enabled the disentanglement of different reaction pathways (Mergel *et al* 1997, Schmidt *et al* 2002). A selection of some of the most recent results and developments concerning electron capture reactions will be presented in section 4.4.1. We will then report on the latest data on projectile ionization in section 4.4.2, another subject where measurements with reaction-microscopes made significant contributions to our understanding of the reaction dynamics. Though one-electron transitions, i.e. those where only the projectile is ionized or excited, are not accessible because no target ion is produced, experiments on the ionization of both, the projectile and the target, however, allowed separation of different reaction mechanisms which are not distinguishable by other methods (Dörner *et al* 1994, Wu *et al* 1994, Kollmus *et al* 2002).

Finally, emphasis is given to studies of single and multiple target ionization using reaction-microscopes. Over the last ten years many data have been published covering a large range of projectile energies and charge states, from $\mathrm{keV\,u^{-1}}$ protons and low charged ions (Dörner *et al* (1996a), Abdallah *et al* (1998), see also Dörner *et al* (2000)) via $\mathrm{MeV\,u^{-1}}$ velocities (Unverzagt *et al* 1996, Jardin *et al* 1996, Schulz *et al* 1999, Weber *et al* 2001) up to $\mathrm{GeV\,u^{-1}}$ bare uranium (Moshammer *et al* 1997). In several experiments the kinematically complete information has been obtained for single (Weber *et al* 2000c, Moshammer *et al* 2001), double (Perumal *et al* 2002, Fischer *et al* 2003) and even triple ionization (Schulz *et al* 2000) of the target atom. FDCSs for ionization by ion impact are available for the very first time (Schulz *et al* 2003), which serve as ultimate tests of theories. Some of the most recent results in the two regimes, i.e. ionization at low and at high velocities, respectively, where ionization proceeds via completely different reaction mechanisms, will be reviewed in the last two subsections of section 4.4.

4.4.1. Electron capture: dynamics and spectroscopy. In capture reactions, i.e. when the electron is bound in the initial target as well as in the final projectile state, the Q-value of the reaction is accessible by the measurement of the longitudinal momentum $P_{\mathrm{R}\parallel}$ of the recoiling target ion (see section 2.2). The discrete values of electronic binding energies in both projectile and target lead to discrete values for $P_{\mathrm{R}\parallel}$ corresponding exactly to the longitudinal momentum change of the projectile. Thus, the measurement of $P_{\mathrm{R}\parallel}$ is equivalent to projectile energy gain or loss spectroscopy. However, the recoil-ion momentum determination is almost completely independent on the quality and on the absolute velocity of the incoming beam. As a result, COLTRIMS allows energy gain measurements with typical resolutions in the order of $\Delta E_{\mathrm{P}}/E_{\mathrm{P}} \approx 10^{-5}$ even at $\mathrm{MeV\,u^{-1}}$ impact velocities, whereas already the preparation of ion beams with correspondingly small momentum spread is hard to achieve. A further advantage is that projectile scattering angles in the μrad regime or even below become accessible by the determination of the recoil-ion transverse momentum with almost no limitations posed by the divergence of the incoming projectile beam. Thus, in contrast to traditional experimental methods such as electron and photon spectroscopy, COLTRIMS allows the measurement of state selective capture cross sections differential in the projectile scattering angle. The obtained data contain valuable information about the collision dynamics and the level energies of populated states.

At projectile velocities v_{P} which are small compared to the target electron velocity ($v_{\mathrm{P}} < 1$ a.u.) it is well established that single electron capture takes place at large internuclear

distances at localized crossings of the Coulomb potential curves in the incident and exit channels. This energy matching condition leads to a narrow range of finally populated projectile states. In contrast, at very high projectile velocities ($v_P \gg 1$ a.u.) the matching of the electron momentum in the initial and final state determines the characteristics of the capture process which predominantly leads to transfer into low lying projectile states. Abdallah *et al* (1998a) used COLTRIMS to investigate the change in the energy range of populated states during the transition from low to high velocities for single and double electron capture in Ar^{16+} on He collisions at various velocities between 0.3 and 1.5 a.u.. With a recoil-momentum resolution of 0.2 a.u. the finally populated projectile states could be resolved with respect to their principal quantum number n.

Figure 30 shows density plots of the longitudinal versus transverse recoil momenta for single electron capture at projectile velocities of 0.3 a.u. and 1.5 a.u., respectively. The $P_{R\parallel}$ values are already converted into Q-values using equation (4). They found, that with increasing velocity the reaction window (the range of populated states) spreads. Moreover, and in contrast to expectations based on simple models, an increasing population of higher n-states has been observed as the projectile velocity is raised. The authors speculated that this behaviour is partly due to the increasing angular momentum transfer in collisions at larger v_P enabling the population of states with both high n and angular momentum l, which have a high statistical weight. The projectile scattering angle for a given Q-value was found to be centred on the 'half Coulomb angle' $\theta_C = Q/(2E_P)$ for the lowest velocity (E_P: projectile energy). The angle θ_C separates regions of capture on the way in, leading to small scattering angles, from those on the way out giving rise to larger deflections. Thus, this indicates an approximately equal probability for transfer on the way in and out. However, at 1.5 a.u. velocity the projectile angular distributions are shifted to significantly larger angles than θ_C (figure 30).

With an improved apparatus Fischer *et al* (2002) demonstrated that COLTRIMS can be used to obtain spectroscopic information about energy levels in highly charged ions which are not directly accessible by other methods. They measured state resolved differential cross sections for single electron capture from He in collisions with 3.15 keV u^{-1} Ne^{7+} ions extracted from an EBIT. In contrast to previous measurements and in order to obtain a very high momentum resolution the recoil-ions were extracted in the longitudinal direction (i.e. along the ion beam) and deflected with a pulsed kicker onto the recoil detector placed beneath the incoming projectile beam. The finally obtained recoil-momentum resolution of 0.07 a.u., which was limited only by the residual thermal spread of the gas-jet target, resulted in a Q-value resolution of 0.7 eV, which is sufficiently high to obtain spectroscopic information about the principal quantum number, subshell level and spin state of the captured electron. The recoil-ion $P_{R\parallel}$ distribution, converted into Q-values and level energies of Ne^{6+} ions following single electron capture from He at $v_P = 0.35$ a.u., is shown in figure 31. The spectrum consists of three groups of lines corresponding to the 2s4l, the 2s3l and the doubly excited states 2p3l of Be-like Ne-ions. A line-fitting procedure has been applied after calibration of the Q-value axis resulting in accurate values for, in total, 22 level energies in the range from 121 to 166 eV with an absolute precision between 3 and 100 meV. The experimental level energies are in excellent agreement with calculated ones, except for the $2p3p\ ^{1,3}S$ and the $2p3s\ ^{1}P$ states, where the theoretical values deviate among each other and from the measured result by more than 0.5 eV.

During the last two years a new generation of spectrometers has been developed making use of laser cooling techniques for the target preparation, mainly because of two reasons. First, to extend the range of atomic targets accessible with COLTRIMS and, second, to further increase the recoil-momentum resolution. Target atoms trapped and cooled in a MOT have been used to study ion–atom collisions at keV energies. Turkstra *et al* (2001) applied this MOTRIMS technique to study multi-electron capture processes in collisions of 3 keV u^{-1} O^{6+}

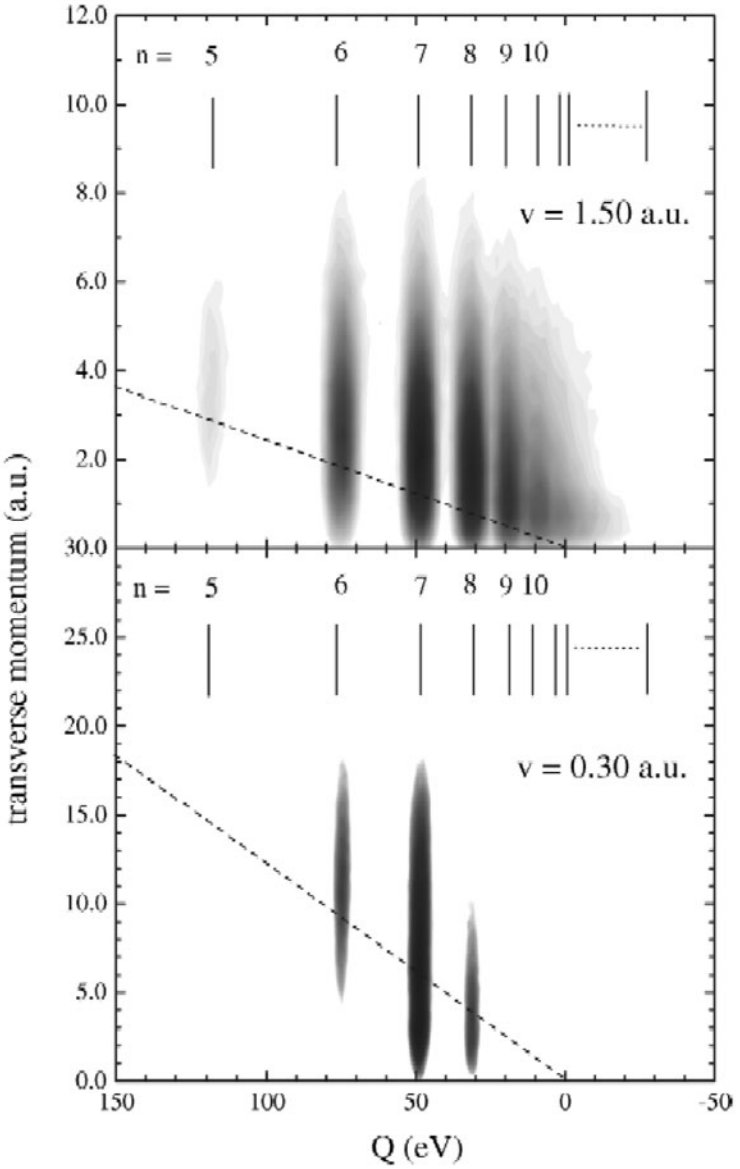

Figure 30. Transverse momentum transferred to the recoil-ion versus Q-value for single electron capture in Ar^{16+}–He collisions at different projectile velocities. The principal quantum numbers n of populated states are marked as vertical lines. The transverse recoil momenta correspond to projectile scattering angles $\theta_P = P_{R\perp}/P_0$, with P_0 the initial projectile momentum. The dashed lines indicate $\theta_P = \theta_C$ (half Coloumb angle) (from Abdallah *et al* (1998a)).

with Na atoms. Van der Poel *et al* (2001) measured angle differential electron transfer cross sections in collisions of keV Li^+ ions with laser cooled Na atoms. As shown in figure 32 they obtained Fraunhofer-type diffraction patterns for the scattered projectile angular distributions in agreement with semi-classical impact parameter models. Lee *et al* (2002) reported on state selective capture measurements for 6 keV Cs^+ colliding with rubidium in 5s and 5p states, with a so far unprecedented recoil resolution of 0.03 a.u. (or a recoil velocity resolution

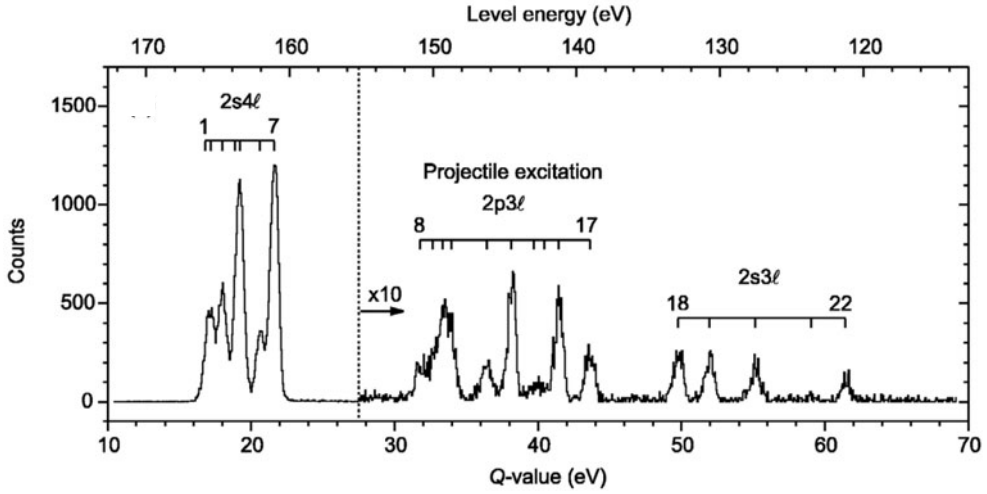

Figure 31. Q-value spectrum and level energies relative to the GS of Ne^{6+} following single electron capture in Ne^{7+}–He collisions at 63 keV (from Fischer *et al* (2002)).

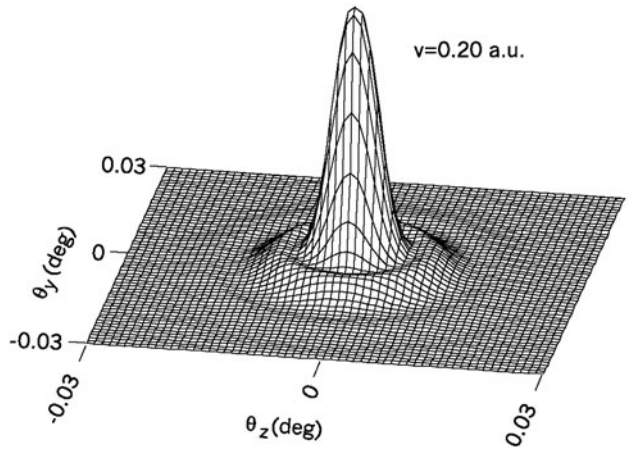

Figure 32. Angular scattering pattern $\sigma(\theta)$ of Li-atoms emerging from electron transfer collisions at 6 keV with cold Na, deduced from the measured transverse recoil-ion momentum distribution. Fraunhofer-type rings in the angular distribution are clearly resolved (from Van der Poel *et al* (2001)).

well below $1\,\mathrm{m\,s^{-1}}$). For the future, it can be anticipated that MOTRIMS will become an important tool, complementary to traditional methods, for precision spectroscopy of highly charged ions.

Reactions where two electrons are transferred from the target to the projectile contribute significantly to the total capture cross section at low projectile velocities. The ratio of double to single electron capture is about 20% for Ne^{10+}–He collisions at impact energies between 50 and 150 keV (Flechard *et al* 2001a). Usually, the capture of two electrons by slow, highly charged ions leads to the population of doubly excited states in the projectile. They can decay either radiatively resulting in true double capture (TDC) or through autoionization processes leading to a projectile which has kept only one electron and a doubly charged recoil-ion

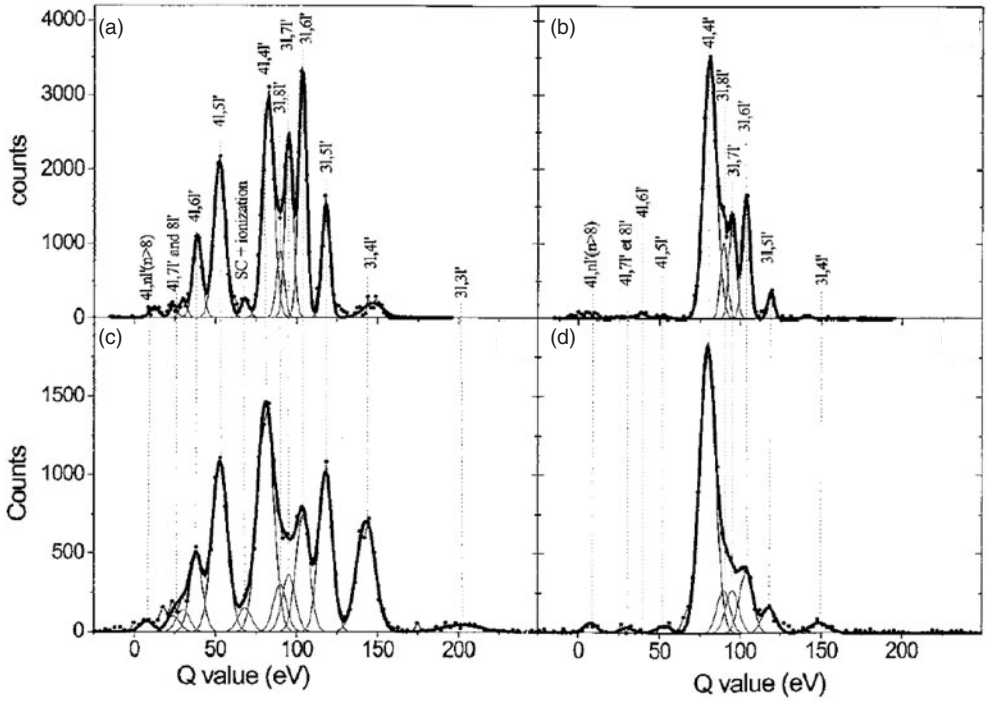

Figure 33. Recoil-ion longitudinal momentum distributions converted into Q-values for double electron capture from He in collision with Ne^{10+} at 50 keV (upper part) and 150 keV (lower part). The result for TI is plotted on the left and TDC on the right side. The labels denote the quantum numbers (nl, n′l′) of populated doubly excited states (from Flechard *et al* (2001a)).

(TI or autoionizing double capture). Flechard *et al* (2001a) measured the corresponding Q-value distributions for double capture from He in collisions with Ne^{10+} at impact energies of 50 keV and 150 keV (figure 33), to gain information about the underlying capture mechanisms, which are still under discussion. The two electrons can be transferred either sequentially through two single capture channels or in one step through a correlated two-electron transition as proposed by Stolterfoht *et al* (1986) and others. Based on the analysis of state selective angular distributions and the good agreement with semi-classical coupled-channel calculations, Flechard *et al* (2001a) concluded that double capture in Ne^{10+}–He collisions proceeds predominantly in two steps by independent electron interactions and not by processes involving the electron–electron interaction. The importance of two-step processes in populating doubly excited states has already been mentioned earlier by Abdallah *et al* (1998a) for Ar^{16+}–He collisions.

The autoionizing channel in multiple-electron capture collisions of slow ions with many-electron atoms has been studied further by means of coincident Auger-electron COLTRIMS by Hasan *et al* (1999). Here, the recoil-momentum delivers information about the collision dynamics and the binding energies (i.e. the Q-value) of populated states while the coincident Auger-electron spectra contain information about the subsequent relaxation pathways of highly excited projectile states. For slow N^{7+} (28 keV) on Ar impact it was found that double electron capture is accompanied by simultaneous excitation of the target atom with high probability (between 40% and 60%) in overall agreement with the classical overbarrier model (see, e.g. Niehaus (1986)).

Recently, ion-molecule collisions and the dynamics of molecular fragmentation have been studied (Adoui *et al* 1999, 2001, Frémont *et al* 2002, Wolff *et al* 2002). At low velocities one or several electrons are captured by the highly-charged projectile and then, in a second step, fragmentation of the molecular ion occurs which is imaged using RIMS. For the fragmentation of CO^{2+} as a consequence of electron capture reactions with keV O^{7+} projectiles, Tarisien *et al* (2000) were able to distinguish different fragmentation channels by means of measured kinetic energies released during the Coulomb dissociation. For molecules aligned along the beam direction they found KERs shifted systematically to larger values which, in agreement with theoretical predictions (Wood and Olson 1999), is due to the interaction between the molecular fragments and the outgoing projectile. Fragmentation of D_2 following double electron capture in collisions with Xe^{26+} projectiles at low velocities (0.2–9.5 keV u^{-1}) has been studied in a kinematically complete experiment by DuBois *et al* (2000) and Ali *et al* (2001). At the lowest velocity the projectile remains in the vicinity of the molecule during fragmentation leading to a transfer of internal energy from the molecule to the projectile. The fragments were found to be less energetic in the centre-of-mass (CM) system of the molecule. Hence, the separation of the reaction into two steps, electron capture and subsequent fragmentation, breaks down for very slow collisions. The experimental results are in good agreement with five-body classical trajectory Monte Carlo (CTMC) calculations (Wood and Olson 1999, Feeler *et al* 1999).

The electron capture cross sections are rapidly decreasing as the projectile velocity is increased (for $v_P \gg 1$ a.u.) while the capture mechanisms differ significantly from those at low velocities. The first kinematically complete experiment on electron capture accompanied by ionization of another target electron (TI) in 0.5–1.4 MeV proton on He collisions, has been performed by Mergel *et al* (1997), where different mechanisms contributing to TI could be separated. In this case, three particles are in the final continuum state (corresponding to nine momentum components) demanding the determination of five momentum components to obtain the complete information. This has been achieved by measuring the recoil-ion momentum vector in coincidence with the transverse scattering of the projectile. Two reaction mechanisms could be distinguished according to their different kinematical signatures. Kinematical capture, where one electron is captured as a result of velocity matching between initial state and projectile velocity, leads to a backward emission of the recoil-ion because it has to compensate the electron forward momentum. The second target electron is ionized independently in a second step due to, e.g. SO. In contrast, in electron capture based on the e–e Thomas mechanism (Thomas 1927) the recoil-ion acts as a spectator and remains basically at rest. There, one electron is knocked by the projectile to an angle of 45° and then, in a second step, it may bounce off the other target electron into the forward direction with a velocity equal to that of the projectile, such that it can be captured easily. In this case, the other electron is emitted perpendicular to the beam with a velocity v_p. The e–e Thomas mechanism leads to a scattering angle of 0.55 mrad for the proton. Figure 34 shows the longitudinal momentum distribution of He^{2+} ions for different proton energies and scattering angles. The left vertical lines show the expected values of $P_{R\|}$ for kinematical capture at the given projectile energies. The full curves are results of a calculation where the two-electron transition is treated as two independent one-electron transitions for transfer and ionization. Thus, the e–e Thomas mechanism is not taken into account in this independent electron approximation. The appearance of an additional structure in the recoil-ion momentum distribution centred around $P_{R\|} = 0$ for 0.55 mrad scattering angles has been interpreted as a clear signature for capture due to the e–e Thomas mechanism.

In a later publication, Mergel *et al* (2001) and Schmidt-Böcking *et al* (2002, 2003, 2003a) analysed the electron emission characteristics for the same collision system at small scattering

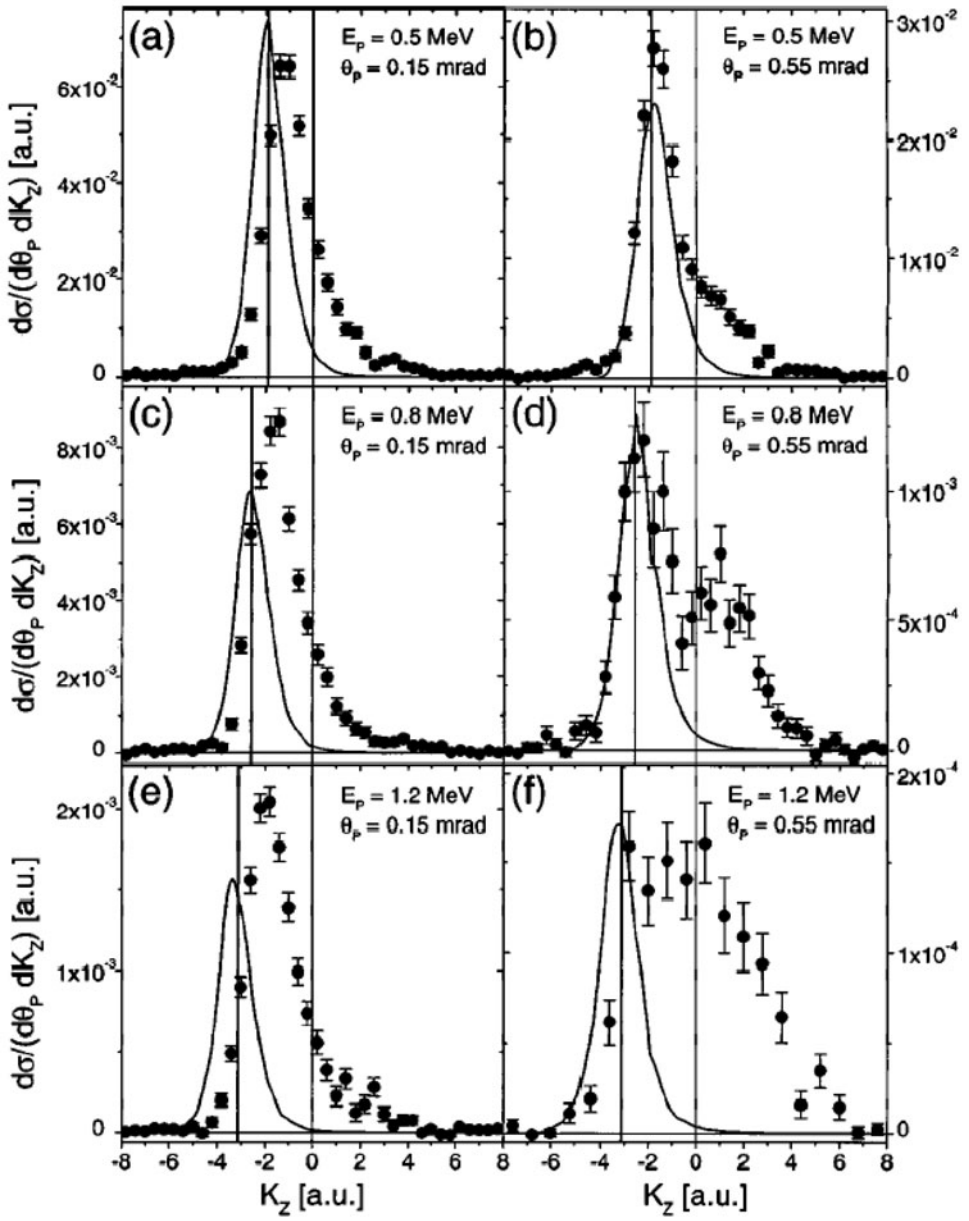

Figure 34. Longitudinal momentum distributions of recoil-ions at fixed scattering angles for simultaneous transfer and ionization in proton He collisions (doubly differential cross section $d\sigma/(d\theta_P\, dP_{R\parallel})$). The scattering angle θ_P is 0.15 (left column) and 0.55 mrad (right column). Left vertical lines: expected $P_{R\parallel}$ for kinematical capture. Solid curves: results of an independent electron approximation (from Mergel *et al* (1997)).

angles. In this case, TI is expected to be well described as a two-step process. One electron is captured due to kinematical capture and the second electron is ionized due to either a SO process or due to ionization by an independent encounter with the proton. The slow ionized electron is expected to be emitted either isotropically or preferentially in the transverse direction. However, most of the electrons were found to be emitted in the backward direction in

a narrow cone around the H^0 scattering plane. This is surprising, because for two independent scattering events the transverse momentum transfer would be randomly oriented with respect to the scattering plane. Moreover, the measured transverse momenta of both, the electron and the recoil-ion, never coincided with the locations expected for a two-step process. From these observations the authors concluded that the correlated electron momenta in the initial He GS play a crucial role. The capture process picks out, by velocity matching, components of the initial state wave function for which one electron has a large forward directed momentum equal to v_P. In a correlated initial state, however, a large forward momentum of one electron might correspond to a high backward momentum of the second electron, which appears in the continuum after ionization.

Recently, Schmidt *et al* (2002) succeeded in applying COLTRIMS for the study of electron capture and TI in 2.5–4.5 MeV p–He collisions. Using an intense beam of the ion storage and cooler ring CRYRING and a novel switching technique for the recoil spectrometer with an electrically gated recoil-ion drift path, they were able to measure cross sections as small as $10^{-26}\,\mathrm{cm}^2$. A close connection between TI and photoionization has been found. The probability for electron emission in kinematical capture decreases with increasing velocity and approaches the photoionization SO value of 1.63%. In both cases (TI and photoionization), very little momentum is transferred to the first removed electron, which leaves the target with a velocity determined by the projectile, while the second electron is ionized via SO. In the same experiment, the high-velocity dependency of the e–e Thomas cross section has been measured which is found to be in agreement with the theoretically predicted v_P^{-11}-scaling.

4.4.2. Projectile ionization: a novel approach to (e,2e)-experiments on ions. The ionization of a non-bare projectile in an ion–atom collision may proceed via an interaction of the projectile electron with an electron (e,e) or the nucleus (e,n) of the target as illustrated in figure 35. Interest arises on the one hand since projectile ionization represents the cleanest situation to study dynamical electron–electron correlation in a challenging, still fundamental four-body process involving two heavy and two light particles. On the other hand, a strict experimental separation of both contributions to projectile ionization might pave the way to performing differential experiments on the ionization of ions by electron impact, one of the most fundamental processes in atomic collision physics.

The importance of effective electron–ion collisions in energetic ion–atom collisions was pointed out very early by Bates and Griffing (1953, 1954, 1955). Driven by the motivation mentioned above, numerous theoretical (see, e.g. McGuire *et al* (1981), Hippler *et al* (1987), Lee *et al* (1992), Fiol *et al* (2001)) as well as experimental studies have been reported in the literature. A first experimental identification of the (e,e) contribution by Montenegro *et al* (1992) exploited its threshold behaviour by measuring the velocity dependence of total projectile ionization cross sections. Further investigations concentrated on identifying this contribution by the appearance of characteristic transition lines in high-resolution zero-degree electron spectra (Zouros 1996) or by its specific kinematical signatures (Montenegro *et al* 1993). Calculations by Montenegro and Meyerhof (1992) indicated that the (e,e) interaction dominates the cross section for projectile ionization at large inter-nuclear distances b since the nuclear potential of the target, that might cause ionization of the projectile in an (n,e) interaction as well, is effectively screened by the target electrons as illustrated in figure 35. In addition, the (e,e) contribution ('anti-screening') leaves the target nucleus as a spectator without any significant final momentum, whereas it noticeably recoils if the screened target nuclear potential takes over the active part in the (n,e) reaction at smaller b ('screening').

Substantial progress was achieved about ten years ago using RIMS. Measuring the target (recoil)-ion momentum distribution, two maxima in the doubly differential cross sections as

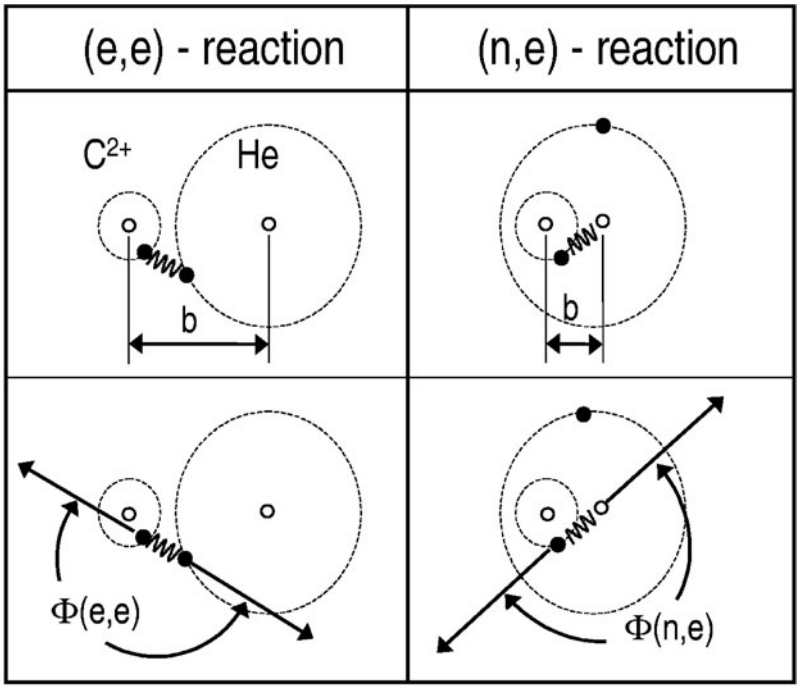

Figure 35. Schematic illustration of the kinematics for (e,e) and (n,e) contributions to projectile ionization (from Kollmus *et al* (2002)).

a function of recoil-ion momentum were identified by Dörner *et al* (1994) and Wu *et al* (1994). Their projectile velocity dependent relative locations were closely related to those expected from target-ion kinematics for each of the processes and essentially reproduced by n-electron CTMC (nCTMC) calculations with two active electrons. Surprisingly, close to threshold, where the two maxima were observed, the calculations were only found to be in quantitative agreement with the experiments if an additional reaction channel, double target ionization plus electron exchange, was taken into account.

Very recently, the first kinematically complete measurement has been reported on simultaneous single ionization of the projectile and of the target in C^{2+} on He collisions at 3.6 MeV u^{-1} by Kollmus *et al* (2002). Projectile ionization was identified by separating the emerging C^{3+} ions in a magnet and detecting them with a fast scintillation counter. In a reaction-microscope, the vector momenta of all other collision fragments have been detected in coincidence with the emerging C^{3+} ions covering the major part of the twelve-dimensional 4-particle final-state momentum space.

As is pointed out by Kollmus *et al* (2002) and illustrated in the lower part of figure 35, (e,e) and (n,e) contributions to projectile ionization are expected to differ in the correlated dynamics of the active particles: whereas the active target electron should dominantly compensate the major part of the momentum transfer $\vec{q}$ to the C^{2+} projectile in an (e,e) ionization event, this role is taken by the target nucleus if the (n,e) interaction dominates. Since $\vec{q} = -(\vec{P}_R + \vec{P}_e)$ with $\vec{P}_e$ being the momentum of the emitted target electron, the criterion that $|\vec{P}_R| \geqslant |\vec{P}_e|$ or vice versa was used to identify the active role of one or the other emerging target fragment (the upper index 'f' for final is omitted for convenience). As illustrated in the lower part of figure 35, the particular fragment taking over the active role in a certain collision is expected to be scattered predominantly opposite to the ionized projectile electron in the azimuthal plane.

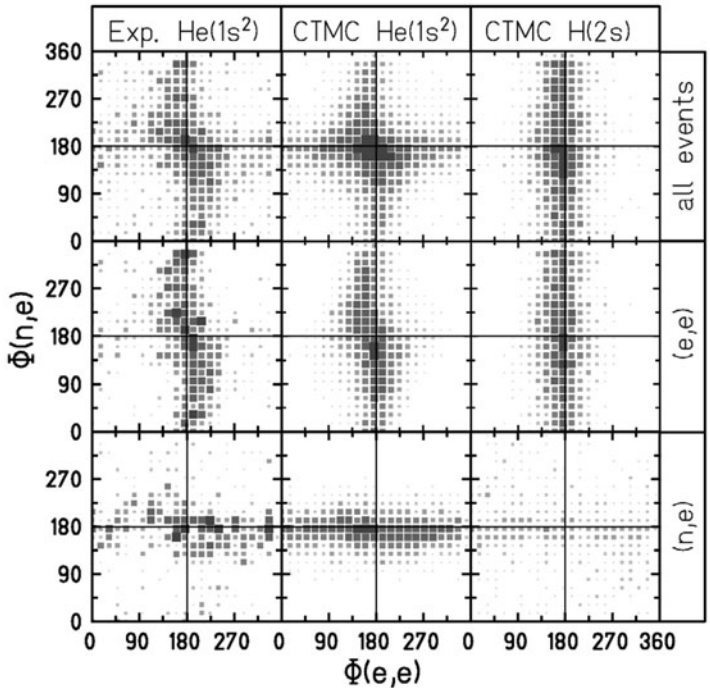

Figure 36. Azimuthal angle between projectile electron and target He^{1+} recoil-ion Φ(n,e) versus azimuthal angle between emitted target and projectile electrons Φ(e,e) for 3.6 MeV u^{-1} C^{2+} on He($1s^2$) collisions (left column: experiment; middle column: CTMC) and for 3.6 MeV u^{-1} C^{2+} on H(2s) collisions (right column: CTMC). Z-scale is logarithmic with ten steps from the minimum to the maximum cross section in each column represented by different sizes of the symbols. Upper row: All events. Middle row: $|\vec{P}_e| \geqslant |\vec{P}_R|$. Lower row: $|\vec{P}_e| \leqslant |\vec{P}_R|$ (from Kollmus *et al* (2002)).

In figure 36 measured as well as calculated angles Φ(e,e) are plotted versus Φ(n,e) for all events (upper row), for events with $|\vec{P}_e| \geqslant |\vec{P}_R|$ where the (e,e)-process is expected to dominate (middle row) and for $|\vec{P}_e| \leqslant |\vec{P}_R|$ (lower row) where the target nucleus might take over the active part. Even without any conditions (left upper frame), a significant pattern was observed. Moreover, it was found that a major part of all events was divided into two clearly separated regimes where either Φ(e,e) or Φ(n,e) is close to 180° for $|\vec{P}_e| \geqslant |\vec{P}_R|$ (left column, middle) or $|\vec{P}_e| \leqslant |\vec{P}_R|$ (left column, bottom), respectively. These two regimes can be uniquely related to collisions where either the (e,e) or the (n,e) process dominates the projectile ionization. The experimental results (left column) were observed to be in excellent agreement with theoretical predictions of six-body CTMC calculations that include the two nuclei, the He electrons and the L-shell electrons on C^{2+} (middle column). Even details observed in the experimental data, like systematic variations of the mean value for Φ(n,e) and Φ(e,e) around 180° or the Φ(n,e)-dependent variation in intensity for the (e,e)-events were found to be reproduced by theory.

The latter features clearly demonstrate that three- or four-body interactions are still important. In order to investigate whether this influence can be reduced, another Monte Carlo calculation has been performed for more asymmetric initial conditions, namely for 3.6 MeV u^{-1} C^{2+} on H collisions with the active target electron in an excited $n = 2$ state (right column). Now, the importance of the (n,e)-reaction was found to be drastically reduced, the Φ(e,e) angular distribution is always exactly peaked at 180° independent of Φ(n,e) and the

recoiling-target ion is isotropically scattered with respect to the projectile electron. The latter two indicate that the recoil-ion now has perfectly taken over the role of a spectator (see also Olson *et al* (2003)).

In a further step, the authors were able to demonstrate that the subset of events which fulfilled the condition $|\vec{P}_e| \geqslant |\vec{P}_R|$ closely reflected the dynamics expected for the ionization of C^{2+} by 2 keV electron impact, i.e. for the kinematically inverted electron–ion collision system. This is illustrated in figure 37, where the scaled momentum transfer $|\vec{q}^*| = q \cdot (2 \cdot I_{e_b})^{-1/2}$ is plotted versus the emission angle ϑ_e of the C^{2+} electron with respect to the momentum transfer direction for electron-impact ionization of C^{2+} (upper part) and for 2 keV electron on He collisions (lower part) in a co-planar geometry. The momentum transfer has been scaled to take into account the different ionization potentials I_{e_b} in both systems. In both panels, the major part of the electrons is seen to be emitted along $\vec{q}$ in binary collisions with the projectile electron, forming the well-known 'binary peak'. Around 180° and for small momentum transfers, another characteristic structure becomes visible, the so-called 'recoil-peak'. Here, the electron is found to be emitted into the $-\vec{q}$-direction due to its interaction with the recoiling

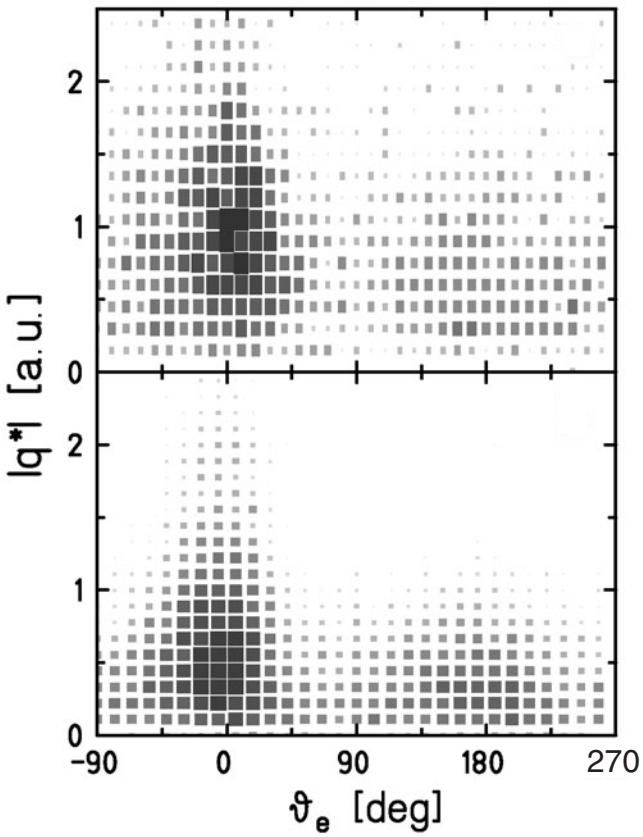

Figure 37. Scaled momentum transfer q^* (see text) versus angle between $\vec{q}$ and the emitted electron ϑ_e in co-planar geometry for C^{2+} ionization (upper part) in inverse kinematics for simultaneous projectile and target ionization with $|\vec{P}_e| \geqslant |\vec{P}_R|$ and He ionization (lower part) by 2 keV electron impact (see text). Z-scale is logarithmic with ten steps from the minimum to the maximum cross section in each panel represented by different sizes of the symbols (from Kollmus *et al* (2002)).

target nucleus balancing both the momentum transfer and the ejected electron momentum (for electron impact, see also figure 23 in section 4.3).

In summary, exploiting the full capabilities of reaction-microscopes in a quadruple coincidence, it was finally demonstrated, nearly 50 years after its first prediction, that one is indeed able to clearly isolate all collision events where the (e,e) reaction dominantly contributed. It was further shown that these events essentially display all features usually observed in (e,2e) electron-atom collision experiments paving the way to future (e,2e)-investigations for all ions over a large velocity regime in heavy-ion storage rings.

4.4.3. Ionization by slow projectiles: SP electrons. At small projectile velocities, where ionization cannot be treated perturbatively, the production of free electrons has to be explained by other mechanisms. In CTMC calculations (Olson *et al* 1997) for p + H collisions Olson found electrons emitted in the forward direction with nearly half of the projectile velocity. Olson (1983, 1986) and Olson *et al* (1987) assumed that these electrons are ones that are left stranded equidistant between the projectile and target ions and are balanced in place by the attractive Coulomb forces of both ions. In quantum mechanical calculations done by Winter and Lin (1984) the relevance of the SP of the two centre Coulomb potential was demonstrated. These authors used a triple-centre atomic-state method with one centre located at the SP.

The velocity of the SP depends on both the charges, that of the projectile as well as that of the target nucleus. In the late 1980s several measurements at collision energies between 50 and 100 keV u^{-1} done at Rolla (Irby *et al* 1988, Gay *et al* 1990) and Bariloche (Bernardi *et al* 1989, 1990) searched for that dependency to demonstrate the existence of the SP mechanism. These measurements at only slightly different acceptance angles, performed with dispersive electron spectrometers, yielded conflicting results. Furthermore, it was controversial which one of the two differential cross sections, $d\sigma/(dv\, d\Omega)$ or $d\sigma/dv$, has to be used to observe a peak at the SP velocity (Meckbach *et al* 1991). Only the Rolla group claimed evidence for the SP mechanism from their experimental data.

Theoretical progress was made by investigating the electron trajectories in CTMC calculations during the collision (Bandarage and Parson 1990, Illescas *et al* 1998). For a more precise classification it was suggested to call only those electrons SP electrons which reach a positive electronic energy slowly, at large internuclear distances R. In contrast, the competing DI ionization causes an abrupt transfer to the continuum. Sidky *et al* (2000) found that the electrons, which already have positive energy at small R, are also preferentially emitted with the SP velocity and concluded that no experimental findings at all are qualified to substantiate the SP mechanism. To avoid all of this controversy we here use the term 'SP electrons' not in the sense of the 'SP process' but referring to the location in momentum space close to the SP.

In quantum mechanical calculations within the semi-classical approximation using adiabatic molecular eigenstates the ionization has to be described by an infinite series of transitions between these states. At complex R the states of the same symmetry are connected by branch points. The Hidden Crossing theory (Solov'ev 1986, Pieksma and Ovchinnikov 1991) determines the ionization probability for p + H collisions by integration in the plane of complex R. Different pathways circumventing the branch points had been found. The so-called S promotion occurs at small R and can be related to the DI ionization, while the T series branch points involve increasing R and are associated with electrons located at the SP. The T series starts out with σ as well as π states. The π states are populated by rotational coupling from the σ initial states. Both molecular symmetries result in a broad maximum in the longitudinal electron momentum distribution centred at half of the projectile velocity. The π states, however, cause a nodal-line for electron emission along the projectile axis which includes the SP (Pieksma and Ovchinnikov 1994, Ovchinnikov and Macek 1995).

Because of the nodal-line structure, spectrometers with small acceptance angle are not qualified to explore π-state dominated SP emission. Therefore, Pieksma *et al* (1994) used a TOF-spectrometer with large acceptance angle to measure the longitudinal electron momentum distribution at 1–6 keV p + H collisions. They found agreement with the theoretical results (Pieksma and Ovchinnikov 1991) but did not resolve the transversal momentum. The first two-dimensional momentum distributions of SP electrons were measured by Kravis *et al* (1996) and Abdallah *et al* (1997) by projecting the electrons and recoil-ions with a high electric field onto position sensitive detectors. Due to the large extraction fields used in the experiment in order to efficiently collect electrons, the recoil-ion momentum and, thus, the nuclear scattering plane was not resolved and a π-state dominated structure could not be observed.

For slow collisions, the momentum exchange between the projectile and target nucleus is typically much larger than the emitted electron momentum (see, e.g. Dörner *et al* (1997)). Thus, the nuclear motion in the semi-classical approximation proceeds in a plane ('nuclear scattering plane'). As a result of the symmetry of the system any π states populated from σ initial states are lying in this plane. The first experiment which was able to determine the scattering plane by using COLTRIMS in combination with slow electron detection was reported by Dörner *et al* (1996a). For 5–15 keV p + He collision they observed the electron momentum distribution projected onto the scattering plane. Most electrons were found in two jets in the forward direction with a minimum at the SP in between (see figure 38(*a*)). This node on the SP is expected for π states. The relative weight of the two jets changes with the collision energy. This was interpreted as a coherent superposition of π and σ contributions with a phase depending on the projectile velocity. Macek and Ovchinnikov (1998) pointed out that these experimental data can be used to extract information about the quasi-molecule formed during the collision, e.g. the potential energy curves of the states coupled to the continuum.

Further experiments using COLTRIMS have been reported by Abdallah *et al* (1998, 1998b, 1999) using He^+, He^{2+} and Ne^+ as projectile and He and Ne as targets. While the two-finger structure found for the p + He system was also observed for He^+ and He^{2+} projectiles, in Ne^+ + Ne collision two spiral arms were emanating from the target and the projectile 'position' in opposite directions (see figure 38(*b*)).

None of these experiments has measured the full electron momentum vector. The projection onto two-dimensional planes always contained the beam axis while the π characteristic can be visualized best in the plane perpendicular to the beam axis. Such a distribution has been measured by Schmidt (2000). He studied the TI in He^{2+} + He collisions, where one of the target electrons is captured by the projectile. In this perspective, the dipole pattern of the π states can clearly be seen lying in the scattering plane (see figure 38(*c*)). For TI in He^{2+} + He as well as He^{2+} + H_2 collisions Afaneh *et al* (2002) extended the acquired range of longitudinal electron velocity and observed a noticeable fraction of electrons moving about 1.2 times faster than the projectile velocity (see figure 38(*d*)).

The tremendous experimental progress motivated further semi-classical calculations. Sidky and Lin (1998, 1999) calculated electron distributions for p + H collisions using the two-centre momentum space discretization (TCMSD). In comparison with the experimental data for p+He (Dörner *et al* 1996a) only a qualitative agreement was found. For p+He collisions at higher impact energy up to 100 keV Edgü-Fry *et al* (2002) compared experimental results to TCMSD calculations, which also treat only one active electron but at an adapted target potential. Only for the longitudinal electron velocity distributions was reasonable agreement obtained. For the p + H system further theoretical work solving the time-dependent electronic Schrödinger equation on a Cartesian grid in configuration space was reported by Schultz *et al* (2002). Chassid and Horbatsch (2002) used the Fourier collocation method, which switches between grids based on coordinate or momentum space representation during the time

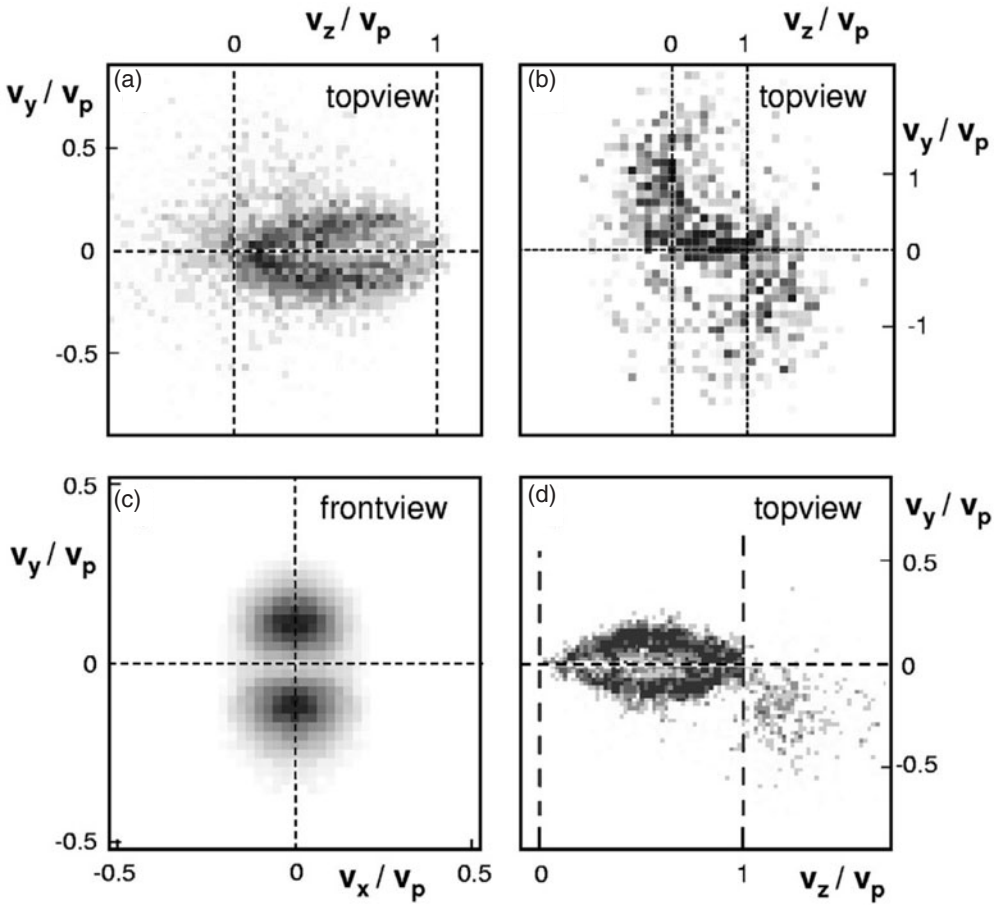

Figure 38. Electron velocity distributions in different planes normalized to the projectile velocity v_P. The Cartesian coordinate system is defined by the beam axis (z), the transversal momentum transfer to the recoil-ion ($-y$) and the direction perpendicular to the nuclear scattering plane (x). (*a*) Projection onto the scattering plane (y, z), 'topview' for the reaction p+He $\rightarrow$ p+He^++e at v_P = 0.63 a.u. (Dörner *et al* 1996a). (*b*) Topview projection for the reaction $Ne^+ + Ne \rightarrow Ne^+ + Ne^+ + e$ at $v_P = 0.35$ a.u. (Abdallah *et al* 1998b). (*c*) Projection of a slice with $0.3 < v_z/v_P < 0.7$ onto the plane perpendicular to the beam direction (recoil-ion moving downward), 'frontview' for the reaction $He^{2+} + He \rightarrow He^+ + He^{2+} + e$ at $v_P = 0.84$ a.u. (Schmidt 2000). (*d*) Topview projection for the reaction $He^{2+} + H^2 \rightarrow He^+ + p + p + e$ (Afaneh *et al* 2002).

propagation. These most recent theoretical results on atomic hydrogen cannot be compared with experimental momentum space images because the COLTRIMS method requires an internally cold gas target, which is not available for atomic hydrogen.

While impressive theoretical progress has been achieved in the treatment of electron transfer reactions in slow collision even for highly excited states of multi-electron systems (see, e.g. Fritsch (1994)), the understanding of the ionization processes at slow projectile velocities is far from satisfactory. All calculations for such collisions performed so far are effective one-electron approximations treating either the p + H collision system or simulating the He target by an effective potential. The fully differential experimental results available today for multi-electron systems have only been understood qualitatively and, therefore, provide a major challenge for the future.

4.4.4. Ionization by fast projectiles: attosecond pulses. This section summarizes a wealth of new results on single and multiple ionization of atoms by fast ionic projectiles. Due to the large number of very recent data, we concentrate to exclusively report on those that have been obtained since the last review. Readers interested in total cross sections, single or double differential data (Cocke and Olson 1991, Ullrich 1994), in electron emission cross sections (Stolterfoht *et al* 1994), in previous reviews (Ullrich *et al* 1994, 1997, Dörner *et al* 2000) or in a comparison with ionization by strong laser pulses (Ullrich and Voitkiv 2002) are referred to the cited literature.

Section 4.4.4.1 concentrates on describing recent results obtained for single ionization at small and large perturbations. In section 4.4.4.2, new double ionization data are presented followed by a short discussion on multiple ionization processes in section 4.4.4.3.

4.4.4.1. Single ionization at small and large perturbations. Single ionization at small perturbations $Z_P/v_P < 1$ (Z_P, v_P: projectile charge and velocity, respectively) was explored in great detail over more than three decades for electron impact in kinematically complete investigations (see section 4.3; for recent reviews see McCarthy and Weigold (1991), Lahmann-Bennani (1991), also Coplan *et al* (1994) and references therein). Here, the FBA has been successfully used to theoretically describe the experimental data, mostly measured in 'co-planar' geometry where the ionized target electron is detected in the scattering plane of the fast electron. In the FBA, all cross sections scale with Z_P^2. Hence, no differences are expected for positively charged ion impact, where kinematically complete experiments have only become feasible since 1994 (Moshammer *et al* 1994) and FDCS had not been reported before 2001 (Schulz *et al* (2001, 2002) for unpublished data, see Weber (1998)).

In figure 39, the main characteristics of the three-particle momentum balance at small perturbations ($Z_P/v_P = 0.06$) are illustrated for single ionization of He for 6 MeV proton impact. Here, the final state momenta of the electron, the recoiling He^{1+} target ion, as well as the momentum change of the scattered projectile are shown (see also Moshammer *et al* (1997) for 1 GeV u^{-1} U^{92+} impact). Exploiting azimuthal symmetry, all momenta are projected onto a plane defined by the incoming projectile momentum vector $\vec{P}_P^{\,i} = P_{P\|}$ and the momentum vector of the recoiling ion $\vec{P}_R = (-P_{Rx}, P_{R\|})$. The momentum change of the projectile in the longitudinal direction is small $q_\| = \Delta E_P/v_P \leqslant 0.4$ a.u. for typical electron energies $E_e < 200$ eV ($\Delta E_P \approx E_e + E_{e_b}$: projectile energy loss). The experimental $\Delta P_{P\|}$-resolution in figure 39 was about 0.1 a. u.. Thus, essentially 'no' momentum is transferred to the target in the longitudinal direction and the transverse momentum transfer is found to be mainly directed opposite to the recoiling target ion, indicating the importance of nuclear scattering.

Deeper insight into the collision dynamics has been obtained by investigating FDCSs as illustrated in figure 40 for single ionization of helium in collisions with 100 MeV u^{-1} C^{6+} projectiles at $Z_P/v_P = 0.1$ (Schulz *et al* 2001, 2002, 2003, Madison *et al* 2002). Here, the FBA is assumed to perfectly describe the data. In figure 40(*a*) is shown the experimental and in figure 40(*b*) the theoretical complete three-dimensional emission patterns for target electrons with defined energy ($E_e = 6.5$ eV) at a fixed momentum transfer $\vec{q}$ with $|\vec{q}| = 0.75$ a.u. as a function of the azimuthal (φ_e) and polar (ϑ_e) electron emission angles. The initial projectile momentum $\vec{P}_P^{\,i}$ directed along the z-axis in figure 39, now points upwards for better three-dimensional illustration of the emission pattern.

The electron emission in three-dimensions exhibits a characteristic double peak structure with two maxima. One is along the momentum transfer direction and the second opposite; the well-known 'binary' and 'recoil' peaks, respectively (for their interpretation see the detailed description in section 4.3 and, e.g., Stefani *et al* (1990), Whelan *et al* (1993)). The theoretical results, which include higher order contributions in the interaction of the projectile

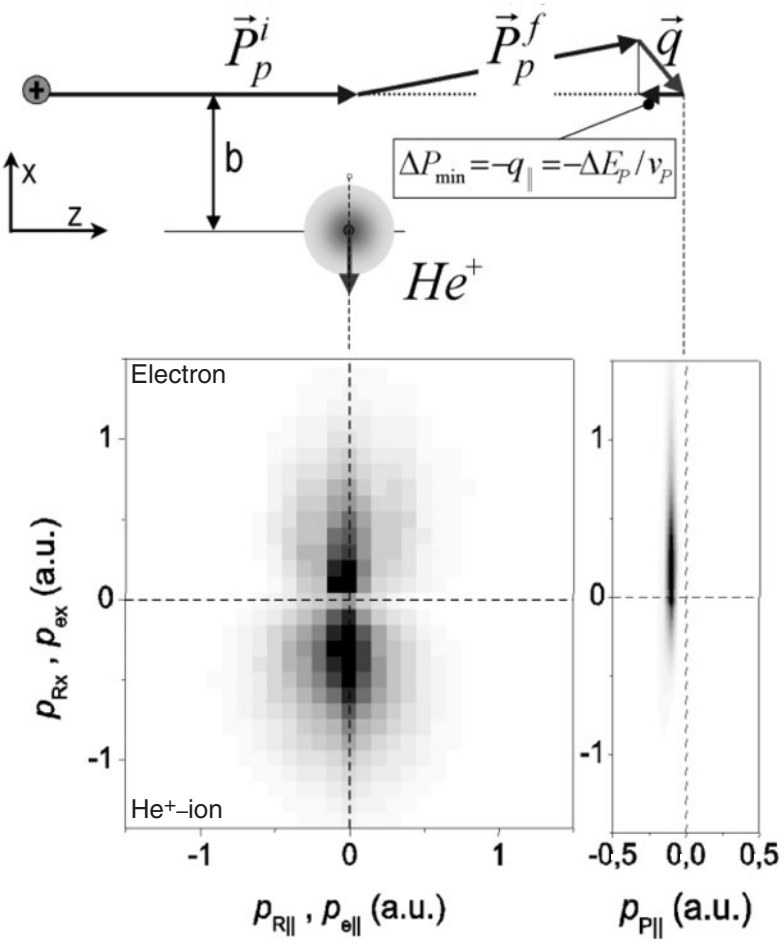

Figure 39. Dynamics for 6 MeV proton on helium collisions. (*a*) Schematic illustration. $\vec{P}_{\rm p}^{\rm i}$, $\vec{P}_{\rm p}^{\rm f}$: incoming and scattered ion momentum, respectively, with momentum transfer $\vec{q} = \vec{P}_{\rm P}^{\rm i} - \vec{P}_{\rm P}^{\rm f}$ and $q_{\rm min} = q_{\parallel} = \Delta E_{\rm P}/v_{\rm P}$ the minimum momentum transfer ($\Delta E_{\rm P}$: projectile energy loss). (*b*) Experimental results: two-dimensional final-state momentum distributions for the recoiling He^+ target ion, the electron and momentum change of the projectile in singly ionizing collisions (logarithmic *y*-scale). The projectiles propagate along the *z*-direction; their field mainly acts along the *x*-axis.

with the target beyond the FBA (for details see Madison *et al* (2002)) were found to be nearly cylindrically symmetric around the $\vec{q}$-axis, a feature characteristic of any first order approach. The sharp three-dimensional minimum at the origin indicates both the absence of higher order processes and the dominance of dipole transitions. Whereas the experimental data were observed to be in close agreement with the predictions in co-planar geometry, i.e. for a cut of the three-dimensional pattern along the plane defined by $\varphi_{\rm e} = 0^\circ$, dramatic deviations were observed out-of-plane. Here, the experimental FDCSs do not shrink to zero close to the origin but exhibit a distinct structure with two maxima in their $\vartheta_{\rm e}$-distribution (counted within the plane tilted by $\varphi_{\rm e}$) at $\vartheta_{\rm e} = 90^\circ$ and 270°. In the plane perpendicular to the scattering plane and containing the initial momentum $\vec{P}_{\rm P}^{\rm i}$, i.e. for $\varphi_{\rm e} = 90^\circ$ the two maxima are of equal size, whereas theory predicts an angular independent, constant behaviour.

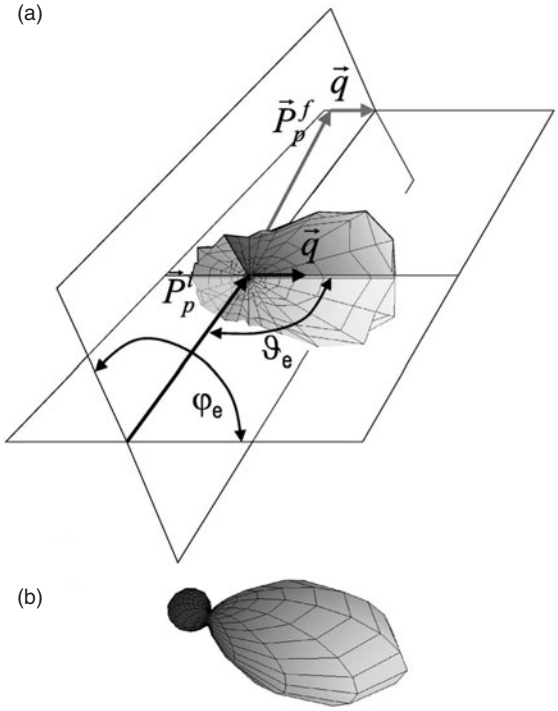

Figure 40. FDCSs in arbitrary units for target electrons with defined energy ($E_e = 6.5$ eV) at a fixed momentum transfer $\vec{q}$ with $|\vec{q}| = 0.75$ a.u. as a function of the azimuthal (φ_e) and polar (ϑ_e) electron emission angles (Schulz *et al* 2003). The initial projectile momentum $\vec{P}_P^{\,i}$ directed along the z-axis in figure 39 now points upwards for better three-dimensional illustration of the emission pattern. (*a*) Experiment. (*b*) Theory (see text).

Two potential reasons have been discussed in the literature for these surprising features in out-of-plane geometry at low perturbations, where the applicability of the FBA was taken for granted on the basis of electron impact FDCSs (nearly exclusively investigated in co-planar geometry). First, in a kind of two-step higher order process the projectile might be deflected by interacting with the ionized target electron in one step (Schulz *et al* 2003). In another step, the projectile elastically scatters off the residual target ion resulting essentially in a rotation of the scattering plane around the azimuthal φ_e angle. Obviously, the details of the projectile deflection then sensitively depend on the relative distance between the passing projectile with respect to the negative electron-charge distribution on the one hand and to the nucleus on the other hand, i.e. on the wave function. This leads to the second possible explanation put forward by Madison *et al* (2003), namely that the scattering wave function used in Schulz *et al* (2003) might not be good enough at small distances relative to the nucleus. (Note added in proof: recent CTMC calculations by Olson and Fiol (2003) using a Wigner distribution for the one-electron GS of the classical He atom essentially reproduced the experimental findings for the first time. Here, the out-of-plane maxima are analysed as resulting from the same dynamics that leads to the in-plane recoil-peak, namely a two-step process where the projectile first interacts with the electron which is then scattered off the nucleus.)

Nuclear scattering in single ionization has been well known to strongly modify differential cross sections at large projectile deflection angles (see DeHaven *et al* (1998) for a recent experiment, discussions in Dörner *et al* (2000), Ullrich *et al* (1997) and references therein).

Its influence at very small momentum transfers, however, came as a surprise, demonstrating that three-dimensional imaging of the ejected electrons, i.e. taking three-dimensional pictures of the final state wave-function square, reveals new insight into the fundamental dynamical three-body problem. Whether or not similar features do occur in electron collisions in out-of-plane geometry is not clear at present, but experiments are underway. Further kinematically complete data have been recorded by Weber (1998) (figures 31 and 32 in Dörner *et al* (2000)) for 0.5 MeV proton on He collisions and FDCSs can be found in Weber (1998).

Relativistic effects for impact ionization of light target atoms (see, e.g. Voitkiv (1996), Voitkiv *et al* (1999)) have never been explored in kinematically complete experiments, since traditional techniques rely on the direct determination of the projectile deflection angle and final energy which is not possible at relativistic velocities. With the advent of reaction-microscopes such studies have become feasible for the first time, since here the momenta of the recoiling target ion $\vec{P}_{\mathrm{R}}$ and of the emitted target electron $\vec{P}_{\mathrm{e}}$ are measured instead, obtaining $\vec{q}$ from momentum conservation $\vec{q} = \vec{P}_{\mathrm{P}}^{\,\mathrm{i}} - \vec{P}_{\mathrm{P}}^{\,\mathrm{f}} = (\vec{P}_{\mathrm{R}}^{\,\mathrm{f}} + \vec{P}_{\mathrm{e}}^{\,\mathrm{f}})$ which, therefore, is accessible for any projectile velocity with the same resolution, presently about 0.1 a.u..

Relativistic effects were first discussed within the context of 'CTMC calculations' (Wood *et al* 1997) in order to explain experimental data for 1 GeV u^{-1} U^{92+} on helium collisions at a relativistic factor $\gamma = (1 - v_{\mathrm{P}}/c)^{1/2} = 2$ (Moshammer *et al* 1997). It was found that the post collision interaction (PCI), a higher order effect that strongly influences the ionization dynamics (see next paragraph), was considerably suppressed due to the relativistic compression of the projectile field along the propagation direction. More recently, relativistic effects and deviations from the dipole-approximation (non-relativistic photon-limit) have been discussed for the same collision system (Voitkiv *et al* 2002, 2002a, 2003). In figure 41, the doubly differential cross section for electron emission is plotted as a function of the longitudinal electron momentum, integrated over certain transverse electron momenta. Clear differences are observed between the dipole-approximation (dotted line), the non-relativistic FBA (dashed

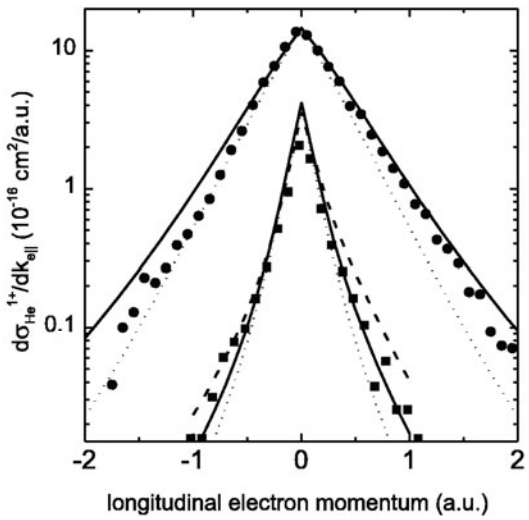

Figure 41. Longitudinal momentum distributions for electrons emitted in singly ionizing 1 GeV u^{-1} U^{92+} on He collision. Circles and squares: experiment; solid and dotted curves: relativistic first Born and dipole-approximation, respectively; dashed curve: non-relativistic FBA ($c \to \infty$). Upper part: emitted electrons with transverse momenta restricted to $p_{\mathrm{e}\perp} < 3.5$ a.u.; lower part: $p_{\mathrm{e}\perp} < 0.25$ a.u. (Voitkiv *et al* 2002).

line) and the relativistic first Born results (full line) being in significantly better agreement with the experiment.

The relationship between single ionization by fast charged particles and photo-ionization, that has been intensively discussed in the past (see, e.g. Bethe (1930), Moshammer *et al* (1997), Stolterfoht *et al* (1999), Ullrich *et al* (2000), Dorn *et al* (2001), Ullrich and Voitkiv (2002) and references therein), has been theoretically explored recently, for the first time, in terms of FDCSs. The fully relativistic treatment (Voitkiv and Ullrich 2001) lead to the 'important conceptual result, that collisions with minimum momentum transfer, which are often termed the optical limit and are regarded to be closest to photo-absorption (Rudd *et al* 1992), in fact can never be photon-like'. Whereas the oscillator strength is the same, directions are just orthogonal with the dipole pattern oriented perpendicular to the photon propagation for photo-absorption and along the projectile direction for charged particle impact. Instead, as has been shown by Voitkiv and Ullrich (2001) the interaction with the charged-particle induced field indeed becomes photon-like, meaning that the absorption of so-called 'transverse' virtual photons dominates for small, but not too small, transverse momentum transfers $\vec{q}_\parallel/\gamma^2 \ll q_\perp \ll \vec{q}_\parallel = \Delta E_P/v_P$.

Deviations from the FBA at strong perturbations $Z_P/v_P \gg 1$ have been extensively discussed in the literature for electron and ion impact (for ions see, e.g. Stolterfoht *et al* (1994) and references therein), in the latter case mostly at large electron energies. With the advent of electron momentum spectroscopy, low-energy electrons became reliably measurable for the first time with meV resolution, and higher order effects were also observed at very low energies in a pioneering experiment by Moshammer *et al* (1994) (see also references therein for previous measurements using conventional spectrometers).

As illustrated in figure 42, single ionization dynamics changes significantly with increasing perturbation for fast, highly charged fast ion impact (for a detailed discussion, see Moshammer *et al* (1994), Ullrich *et al* (1995), Moshammer *et al* (1997a), Olson *et al* (1998), Schmidt *et al* (1998)). Again this is a situation, namely large perturbations at high velocities, that is not accessible for electron impact where $|Z_P| = 1$. While the general characteristics of the dynamics prevail, i.e. small momentum transfers by the projectile still dominate and a pronounced balancing of momenta between recoil-ion and emitted electron is observed, the final-state, however, obviously becomes more and more 'deformed' with increasing perturbation strength. This effect, which was very well described by CDW approaches (see, e.g. Crothers and McCann (1983), Fainstein *et al* (1996), Gulyás *et al* (2000), Fainstein *et al* (2001), full lines in the right-hand panels of the figure: O'Rourke *et al* (1997)), has been interpreted as a 'PCI', an interaction of the receding highly charged projectile ion with the emitted low-energy target electrons and ions in the final state: electrons are dragged behind the projectile whereas the recoil-ion is pushed backwards with about the same force. Reversing the sign of the projectile charge should interchange the role of electrons and ions in the final state, an effect that has been investigated for antiproton impact (Khayyat *et al* 1999).

Even at strong perturbation, only very little momentum is transferred to the target system as a whole into the longitudinal direction for swift collisions. Thus, the width of the momentum distribution along the projectile propagation has been interpreted as a quantity, being inherent to the target itself, namely to the momentum distribution in the GS, the so-called Compton profile (Dörner *et al* 1995). The visibility of bound-state properties has been discussed by Moshammer *et al* (1999). In figure 43, experimental longitudinal electron momentum distributions (DDCS) are shown for different cuts in $P_{e\perp}$ for single ionization of argon (symbols) by 3.6 MeV u^{-1} Au^{53+} impact along with theoretical CDW-EIS predictions (full lines, Fainstein *et al* (1996), Moshammer *et al* (1999)) at a very strong perturbation $Z_p/v_p = 4.4$. Structures were identified near $v_{e\parallel} = \pm 0.5$ a.u. in theory within the error bars of the experimental data. In this first

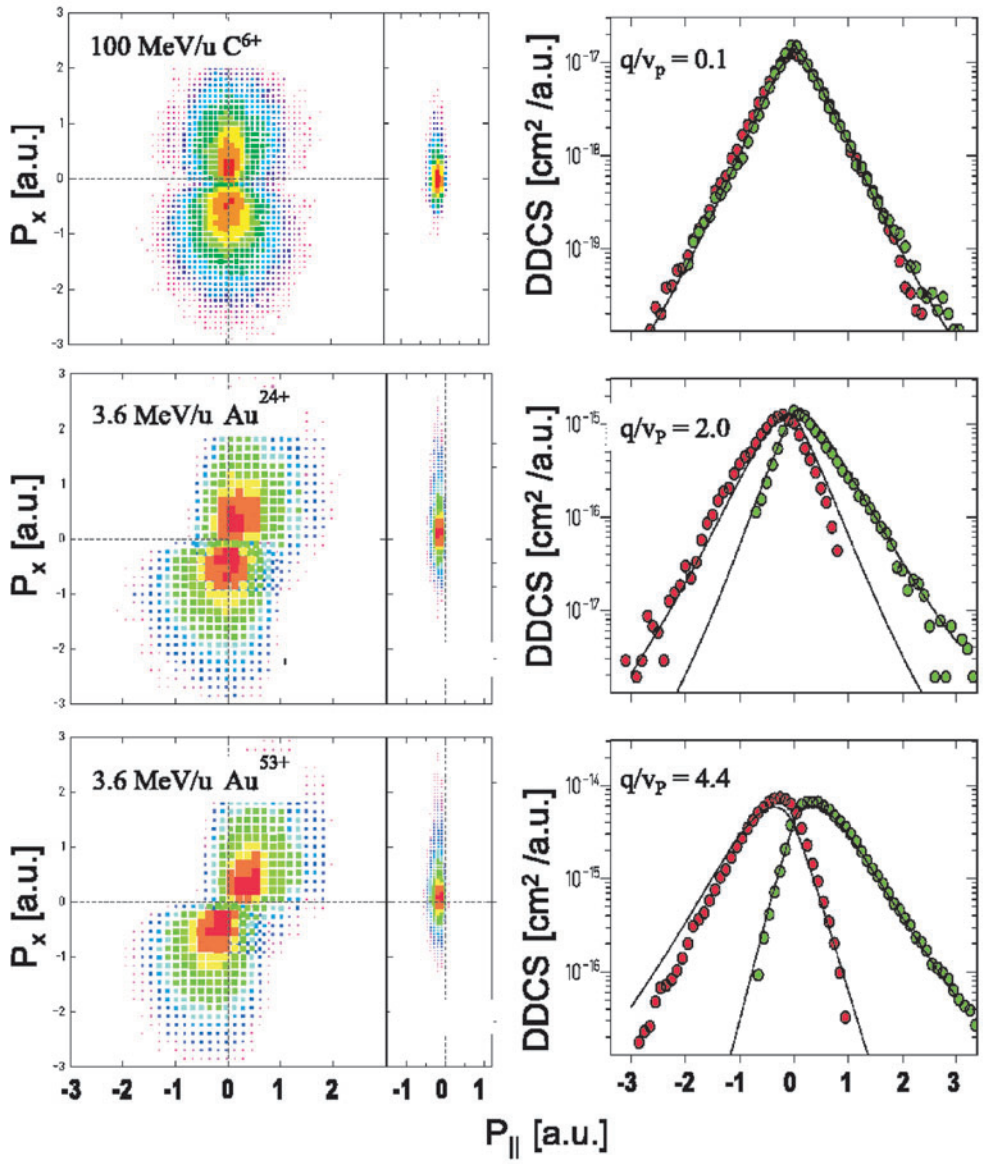

Figure 42. Same as figure 39 (left column) as well as singly differential cross sections for He^+ ions and electrons as a function of the longitudinal momentum (right column) for different projectile charges and impact energies (perturbation strengths as indicated in the figure) in singly ionizing collisions (logarithmic z-scale). The projectile propagates along the $P_{\|}$ direction. ——: CDW-EIS results from O'Rourke *et al* (1997).

calculation, the enhancements were interpreted to be related to the nodal structure of the $3p_0$ state. While this direct signature of the GS momentum distribution (inset) could not be verified in more recent calculations (Gulyás *et al* 2000) it was found, however, to be in agreement with Moshammer *et al* (1999) that different subshells lead to pronounced differences in the longitudinal electron momentum distribution and that all substates have to be considered in order to reproduce the experimental spectrum. Thus, the experiments provided strong evidence

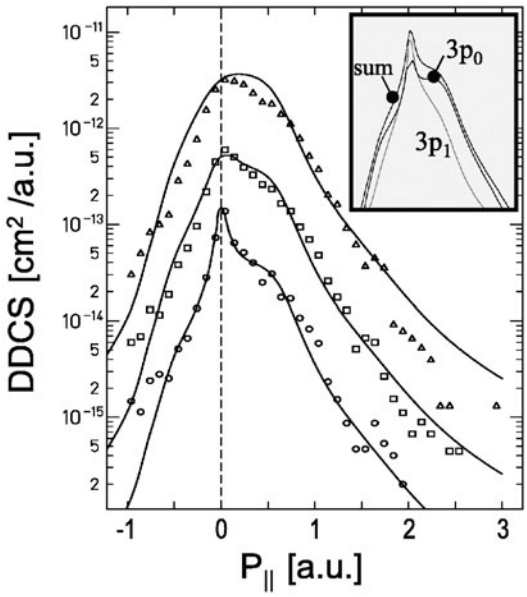

Figure 43. Doubly differential cross sections DDCS $= \mathrm{d}^2/(\mathrm{d}p_\parallel \mathrm{d}p_\perp 2\pi\, \mathrm{d}p_\perp)$ for electron emission in singly ionizing 3.6 MeV u^{-1} ($v_\mathrm{P} = 12$ a.u.) Au^{53+} on Ar collisions as a function of the longitudinal momentum $\mathrm{d}p_\parallel$ for fixed transverse momentum transfers $p_\perp$ as indicated in the figure. Open symbols: experiment. Full lines: CDW-EIS (see text). DDCS at different $p_\perp$ are multiplied by factors of 10, respectively. Inset: theoretical results for different subshells and sum of all contributions (Moshammer *et al* 1999).

that the longitudinal electron momentum distributions reflect the properties of the respective bound-state wave functions.

Recently, multiply or even FDCSs have been reported for strong perturbations as well (Moshammer *et al* 2001, Schulz *et al* 2002, Fischer *et al* 2003a), yielding dramatic disagreement with essentially all non-perturbative theoretical models available. Similar to that for small perturbations, the proper treatment of the full three-body dynamics seems to represent a major challenge for theory (see also Olson and Fiol (2001)). In figure 44, double differential cross sections (DDCSs) for electrons of different energies are plotted as a function of the projectile transverse momentum transfer $p_\perp = P^\mathrm{f}_{\mathrm{P}\perp} = \vartheta \cdot P^\mathrm{i}_\mathrm{P}$ or deflection angle ϑ for 100 MeV u^{-1} C^{6+} (figure 44(*a*)) and 3.6 MeV u^{-1} Au^{53+} (figure 44(*b*)) on helium collisions, i.e. for a perturbative ($Z_\mathrm{P}/v_\mathrm{P} = 0.1$) as well as a strongly non-perturbative ($Z_\mathrm{P}/v_\mathrm{P} = 4.4$) situation, respectively (Moshammer *et al* 2001). At moderate electron energies, $E_\mathrm{e} > 50$ eV, essentially two different dynamical contributions to the spectra can be identified: first, a broad, unstructured shoulder (the only contribution for $E_\mathrm{e} < 50$ eV) at momentum transfers by the projectile $q_\perp = -p_\perp$ smaller than the respective electron energy in a binary projectile-electron collision: $E_\mathrm{e} < p_\perp^2/2m_\mathrm{e}$ (m_e: electron mass). These are electrons that mainly balance their momenta with the recoiling target ions, emitted in a dipole-like interaction with the projectile field without significant momentum transfer. Second, a pronounced shoulder or even a broad peak is observed at transverse projectile momentum transfers that match the respective electron energies $E_\mathrm{e} = p_\perp^2/2m_\mathrm{e}$, the so-called 'binary encounter electrons' (BEE). Whereas the experimental results at small perturbation for fast C^{6+} impact were found to be reasonably well described by an FBA calculation (full line in figure 44(*a*)), dramatic deviations between experiment and theory were observed at large perturbations. A standard CDW calculation

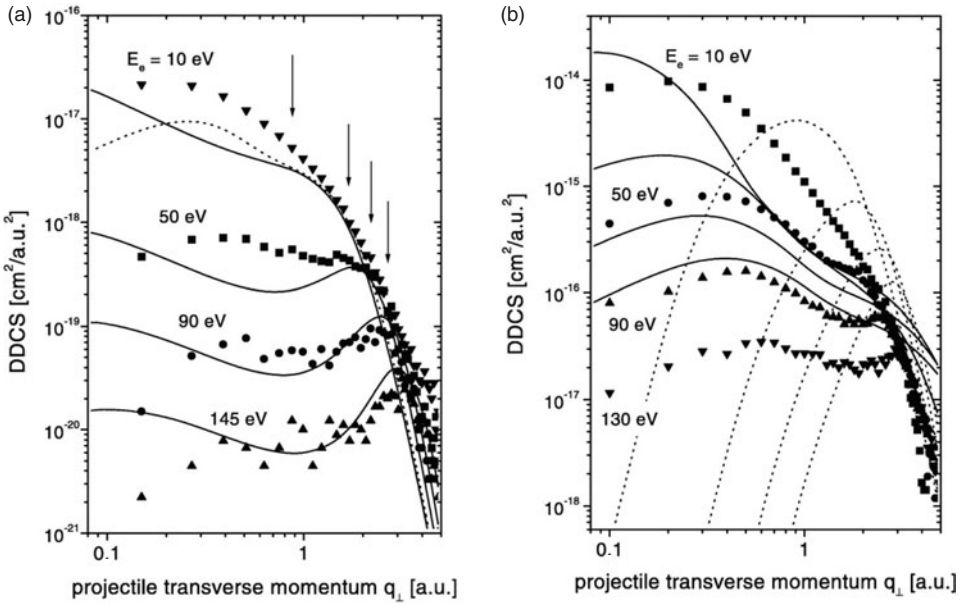

Figure 44. Doubly differential cross sections DDCS $= \mathrm{d}^2/(\mathrm{d}q_\perp\,\mathrm{d}E_\mathrm{e})$ as a function of the projectile transverse momentum transfer for specified electron energies for single ionization of He by (*a*) 100 MeV u^{-1} C^{6+} impact ($Z_\mathrm{P}/v_\mathrm{P} = 0.1$) and (*b*) 3.6 MeV u^{-1} Au^{53+} impact ($Z_\mathrm{P}/v_\mathrm{P} = 4.4$). (*a*) ——: FBA; · · · · · ·: convolution of DDCS for $E_\mathrm{e} = 10$ eV with the experimental resolution $\Delta q_\perp = 0.2$ a.u.. (*b*) ——: CDW-EIS with screened nucleus–nucleus interaction; - - - -: standard CDW-EIS (Moshammer *et al* 2001).

(dashed line in figure 44(*b*)) that does not include the interaction between the nuclei fails completely. Various improvements of theoretical approaches (Olson and Fiol 2001), now implementing the inter-nuclear interaction on different footings and, thus, trying to consider the full three-particle problem, tend to improve the situation (see, e.g., full line in figure 44(*b*)) but, in general, are in surprisingly poor agreement with experiment. Classical calculations that are usually found to describe the many-body dynamics in strong ion-induced fields quite well do not find any binary electrons at all (Olson and Fiol 2001). As in the case for small perturbations, the reasons for these discrepancies are by no means clear at present.

This has been further elucidated recently by Schulz *et al* (2002), who investigated FDCSs for the same collision system, presented in figure 45 for co-planar geometry. Electron emission energies are $E_\mathrm{e} = 17.5$ eV (top) and $E_\mathrm{e} = 55$ eV (bottom) at fixed momentum transfers of 0.65 a.u. (figure 45(*a*)), 1.0 a.u. (*b*) and 1.5 a.u. (*c*). At small q (*a*), the binary peak predicted by theory, along the $\vec{q}$-direction for the FBA (dashed line) and shifted into the forward direction in CDW calculations (full line), is only barely visible in the experiment, whereas a strong new peak emerges pointing exactly in the forward direction. Here, the absolute magnitude is underestimated by a factor of 36–200 by the standard CDW, where the interaction between the nuclei was not considered. Such calculations are just being developed and have not been published yet (Madison *et al* 2003, Fischer *et al* 2003a, b). Increasing the momentum transfer (figures 45(*b*) and (*c*)), the binary peak dominates more and more, yielding increasingly better agreement with theory.

In summary, the few topics mentioned here addressing single ionization by ion impact, namely comprehensive pictures in momentum space including out-of-plane geometries, relativistic effects at large velocities and strongly non-perturbative situations for highly charged ion

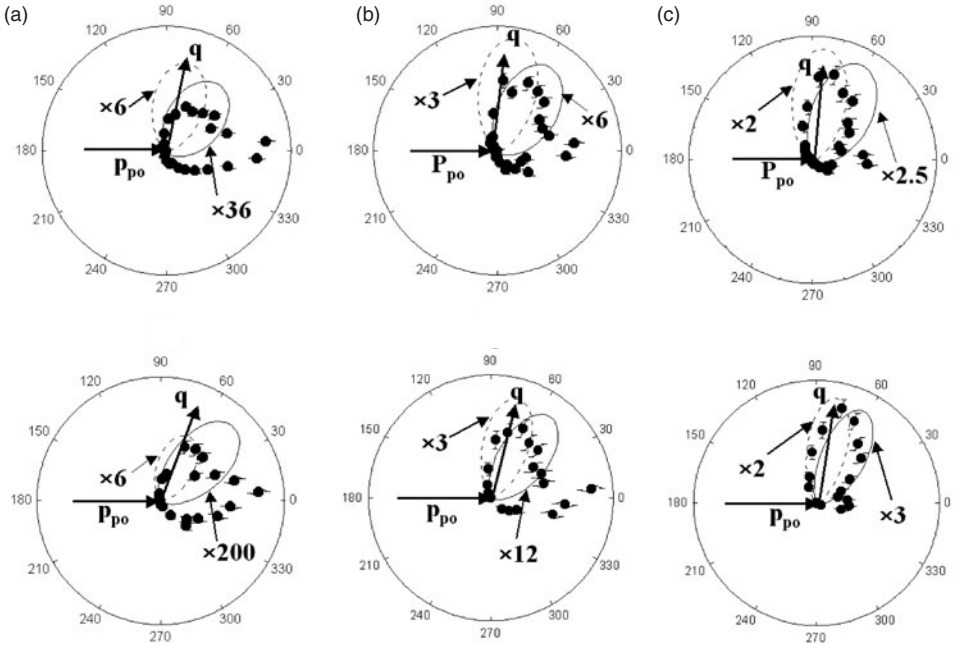

Figure 45. FDCSs as a function of the polar angle for electrons of $E_e = 17.5\,eV$ (top) and $E_e = 55\,eV$ (bottom) emitted in $3.6\,MeV\,u^{-1}$ Au^{53+} on He singly ionizing collisions in co-planar geometry for momentum transfers (left to right) of 0.65, 1.0 and 1.5 a.u.. - - - -: FBA; ——: CDW-EIS (Schulz *et al* 2002).

impact at large velocities, demonstrate in a most impressive way the power of new projection techniques to elucidate many-particle dynamics in situations that have not been accessible with traditional methods. Surprisingly, even after 30 years of research, which, however, was strongly focused on electron impact studies in co-planar geometry, comparison with state-of-the-art theoretical approaches brings to light that even the most simple dynamical situation, the effective three-body Coulomb problem, still seems to be very poorly understood in a general sense.

4.4.4.2. Double ionization at small and large perturbations. Double ionization by ion, photon and electron impact has been extensively discussed in the past (for a review see, e.g. McGuire (1997)). For ion impact, mostly total cross sections were considered (for a review see Cocke and Olson (1991)) until RIMS was developed and singly as well as multiply differential data were reported (for reviews see Dörner *et al* (2000), Ullrich *et al* (1994, 1997)). Starting with a pioneering experiment by Moshammer *et al* (1996), a few kinematically complete experiments for ion as well as for electron impact have been reported using reaction-microscopes. Only recently, experimentalists succeeded in decisively accelerating data capture, essentially by using nanosecond pulsed ion beams, such that highly or even FDCSs could be projected from huge data sets (Fischer *et al* 2003). These comprehensive sets of FDCSs provide the ultimate benchmark for comparison with theory and are exclusively discussed in this paragraph.

In a simplified, though often stressed, illustrative picture based on a perturbation expansion, double ionization by charged particle impact can either occur due to an independent interaction of the projectile field with both target electrons (termed 'two-step-2', TS-2) or, due to a single interaction of the field with the atom, where the second electron is emitted as a result of the electron–electron correlation. In collisions with charged particles, as for photoionization,

the latter process usually is further subdivided in terms of many-body perturbation-theory diagrams: TS-1, a single interaction of the projectile with the target plus a second step, when the emerging first electron interacts with the second one, is distinguished from SO or GS correlation contributions (for diagrams see McGuire (1997)).

At small perturbations TS-1, SO and GS contributions dominate, the interaction of the projectile field with the target can be treated in first order and, consequently, FDCSs should be identical for fast ion and electron impact. Moreover, since the projectile only interacts once with the target atom, transferring a momentum $\vec{q}$, this is the symmetry axis for all differential cross sections. Pioneering experimental and theoretical differential data have been reported for 100 MeV u^{-1} C^{6+} impact, where dynamical mechanisms (Bapat *et al* 1999) as well as signatures of the correlated initial state (Bapat *et al* 2000, Keller *et al* 2000a) were investigated and evidence for SO was provided.

Recently, first FDCSs have been published for 6 MeV proton on He collisions (Fischer *et al* 2003). Seemingly well within the perturbative regime ($Z_P/v_P = 0.06$) for single ionization at least, it has long since been known, however, that the ratio of double to single ionization at this perturbation differs for projectiles with charges of different signs (for reviews see, e.g. Ullrich *et al* (1993), McGuire *et al* (1995), McGuire (1997), Fischer *et al* (2003) and references therein). Whereas the ratio for positively charged particle impact is largely converged to its asymptotic value for $Z_P/v_P \leqslant 0.1$, it is about a factor of two larger for negatively charged projectiles at this perturbation and does not converge until $Z_P/v_P = 0.02$.

Accordingly, as illustrated in figure 46, the FDCSs for co-planar geometry, symmetric energy sharing of the two electrons ($E_{e1} = E_{e2} < 25$ eV) and $q = 0.5$, 1.1 and 1.7, show

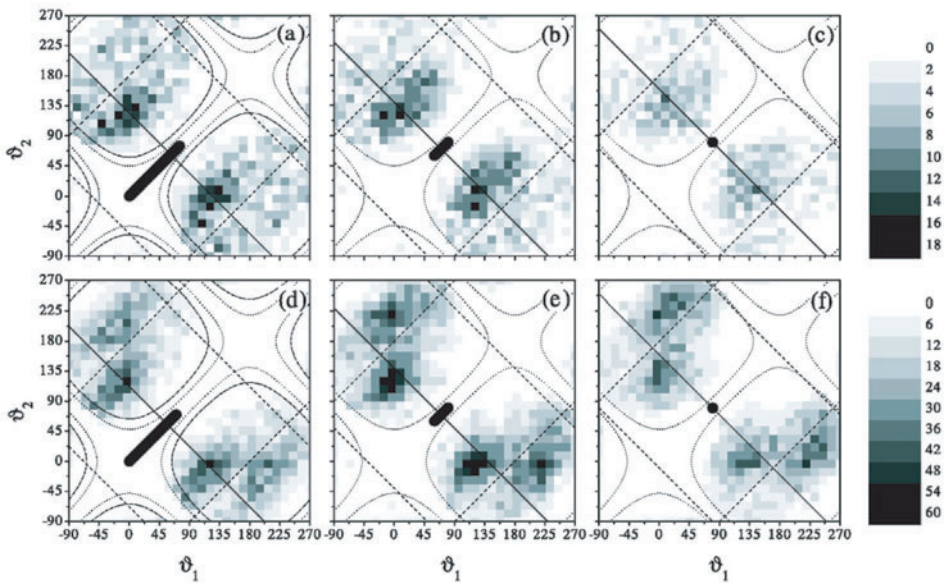

Figure 46. Angular distribution of the two emitted electrons (ϑ_1, ϑ_2: polar angle with respect to the forward beam direction) in co-planar geometry for proton (*a*)–(*c*) and electron (*d*)–(*f*) impact at a momentum transfer of 0.2–0.8 a.u. (*a*) and (*d*), 0.8–1.4 a.u. (*b*) and (*e*), and 1.4–2.0 a.u. (*c*) and (*f*), for $E_{e1} = E_{e2} < 25$ eV symmetric energy sharing. Selected momentum transfer windows are indicated by the black dots or bars. Symmetry axis in the FBA for the centre of gravity of the momentum transfer: black line. Nodes for dipole transitions: dashed lines. Dotted lines encircle regimes with full momentum acceptance (Fischer *et al* 2003).

clear differences for proton (upper row) and electron (lower row) impact, respectively. As general features, in both cases four 'islands' were observed which can be identified to be the binary and the recoil peaks, mirror imaged at the diagonal $\vartheta_{e1} = \vartheta_{e2}$ since the electrons are indistinguishable. Dashed lines indicate kinematical situations which are exactly forbidden in the dipole-approximation (section 4.3). Emission along $\vartheta_{e1} = \vartheta_{e2}$ is prohibited as well, due to the Fermi nature of the electrons. As mentioned, for a first order projectile–target interaction, the patterns have to be symmetric with respect to $\vec{q}$, i.e. point symmetric in the two-dimensional plots with respect to the dots or bars indicated in the figure, representing the finite q-ranges that had to be chosen in the experiment in order to increase statistics.

Two main features were observed by Fischer *et al* (2003): first, proton data are much more symmetric with respect to the momentum transfer direction indicating indeed that they seem to be converged much earlier to the asymptotic limit, even in terms of FDCSs. Higher order contributions, i.e. deviations from the $\vec{q}$-symmetry are clearly identified in the electron data mainly for the 'recoil peak' (see Dorn *et al* (2001, 2003) and section 4.3). Second, the proton impact data show a much less pronounced 'recoil-peak' contribution. It was speculated (Fischer *et al* 2003), that at intermediate impact parameters the positively charged protons tend to pull the electrons away from their parent atom favouring a clean 'binary situation' whereas the electron projectiles tend to push the electron into the atom, causing a stronger recoil-peak (additional interaction with the nucleus) and a more pronounced higher order behaviour.

Clearly, such an interpretation has to await verification by quantum calculations delivering FDCSs, presently underway (Dorn *et al* 2003, Kheifets 2003). Convergence studies of total cross sections (Bronk *et al* 1998) within the multi-cut 'forced impact method' (Ford and Reading 1988, 1990) indicate that positively charged particles do show more 'dynamical' or 'intermediate' correlation than negatively charged ones, in accordance with the above considerations. Since the electrons are mainly pulled towards the proton projectile (enhanced 'binary peak'), they tend to be closer to each other with increased intermediate correlation whereas a negatively charged projectile tends to dilute the two-electron density and, hence, reduces dynamical correlation effects.

At strong perturbations, double ionization is dominated by the TS-2 and higher order diagrams in the Born-series. In TS-2, for example, the ion-induced field independently acts on both target electrons giving rise to their ejection. At present, inspite of a few attempts at electron impact (see, e.g. Dorn *et al* (2003), Mkhanter and Dal Cappello (1998), Grin *et al* (2000)), no quantum mechanical FDCSs are available that consistently include second-order contributions, not to mention higher terms, in the perturbation expansion. Since the electron emission spectra alone, integrated over all projectile scattering angles, have been found to be unaffected by the interaction between the nuclei (Fainstein *et al* 1988) they could be described within the independent particle model (IPM) if correlation between electrons were neglected.

Following these lines, Moshammer *et al* (1997) were able to quantitatively describe single differential cross sections as a function of the energy of one 'typical' electron (integrated over all energies of the second) for double ionization of helium by $1\,\mathrm{GeV\,u^{-1}}$ U^{92+} impact within the dipole approximation. More recently, Kirchner *et al* (2002a) have developed a much more sophisticated IPM model, where the impact parameter dependent effective single-particle ionization probabilities $P_i(b)$ for certain sub-shells i are calculated within the CDW-EIS approach. Using some further approximations ($P_i(b) \equiv 1$ for $P_i(b) > 1$ or using the unitarity prescription by Sidorovich and Nikolaev (1983)), good agreement has been obtained between experimental and theoretical DDCSs for electron emission in neon double ionization. It was concluded that correlation effects between the electrons, which are completely neglected in the IPM, are of minor importance if only a small fraction of all target electrons is emitted, i.e., for low final charge states of the target. For the helium target instead, the IPM was found to

strongly overestimate the experimental DDCSs at all transverse electron energies, indicating that electron correlation cannot be neglected in this case.

The full four-body dynamics has been investigated recently by Perumal *et al* (2002) for double ionization of helium by 3.6 MeV u^{-1} Au^{53+} projectiles. Considering the CM motion of the two emitted electrons by adding their vector momenta, all dynamical features that have been observed for single ionization were rediscovered, showing that the four-body problem could be reduced in good approximation to an effective three-particle problem.

As shown in figures 47(*a*) and (*b*), the recoil-ion was found to essentially compensate the sum momentum of both electrons in the longitudinal (*a*) as well as in the transverse (*b*) directions (the collision geometry is defined as in figure 39), with a strong longitudinal backward–forward asymmetry due to PCI. Transversally (*b*), the projectile deflection was observed to be nearly symmetric around zero, indicating that it is neither dominated by the interaction with the target electrons nor with the nucleus. It has been discussed that these results are surprising at first glance, since the 'two-step two' mechanism was commonly thought of as an independent, binary-like interaction of the projectile with both of the electrons where the projectile transverse momentum would have to be largely balanced by the sum momentum of the electrons. Instead, it was concluded from the data and from calculations (Kirchner *et al* 2002a), that typical impact parameters are so large that the target is 'dissociated' in the strong projectile field, with similar but oppositely directed forces acting on both electrons and on the nucleus, mainly transferring energy to the target in a dipole-like reaction with quite small $\vec{q}$.

Within such a scenario it is not too surprising that the transverse momenta of both individual electrons display a quite similar distribution as shown in figure 47(*d*) in contrast

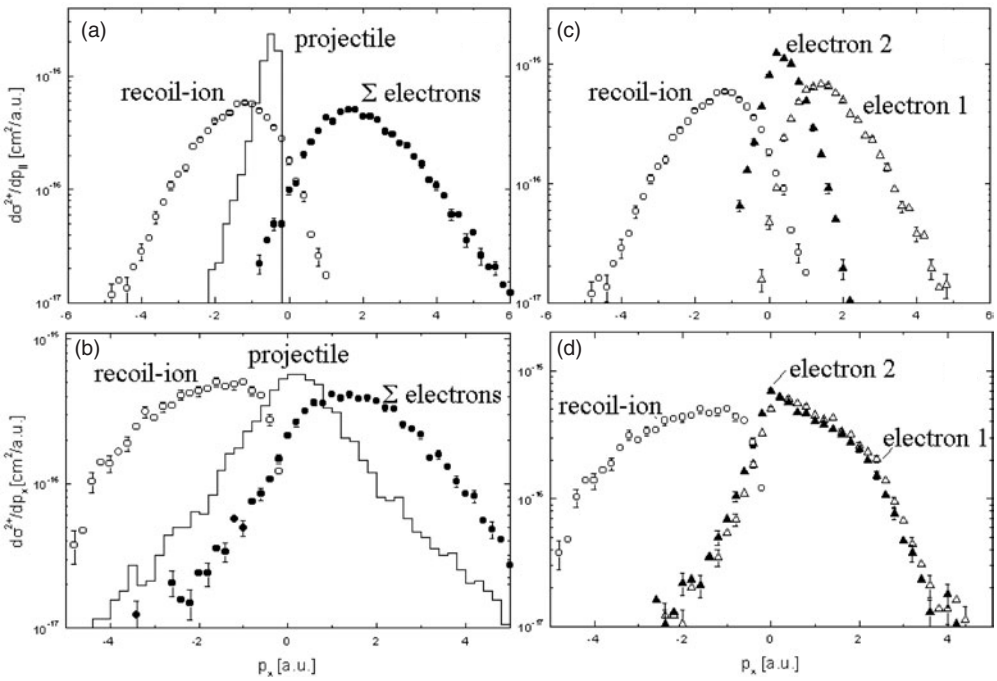

Figure 47. Longitudinal (*a*) and transverse (*b*) momentum distributions for the recoil-ions, the sum of both electrons along with the momentum change of the projectile. In addition, longitudinal (*c*) as well as transverse (*d*) momentum distributions for electron 'one' and 'two' for double ionization of He by 3.6 MeV u^{-1} Au^{53+} (Perumal *et al* 2002).

to the longitudinal ones (figure 47(*c*)), where fast and slow electrons are distinguished by the experiment. This indicates first, that longitudinal and transverse momentum components are independent to a large extent and second, as has been suggested by Perumal *et al* (2002), that a certain realization of the TS-2 mechanism might dominate where the momentum transfer to both target electrons and to the nucleus is not independent in each single collision, but indeed quite similar in magnitude but in opposite directions due to the large impact parameters involved. Then, both electrons would be effectively 'displaced from their nucleus' resulting in a 'Coulomb explosion' of the two electrons with their final state correlation then being intimately connected to their correlated initial state.

Indeed, distinct correlations between the electrons have been found in this experiment as well as in previous measurements for He, Ne double and Ne triple ionization (Moshammer *et al* 1996b). The latter have been discussed and partly explained by classical nCTMC calculations (n-body CTMC, Olson *et al* (1989)) to result from the final state interaction. Moreover, the experiments have triggered calculations within the Weizsäcker-Williams method of equivalent photons (Keller *et al* 1997) for double ionization by $1\,\mathrm{GeV\,u^{-1}}$ U^{92+} impact in the non-perturbative regime (see comments by Voitkiv and Ullrich (2001)). Here, the extremely short, time-dependent electromagnetic pulse created by the projectile is Fourier transformed into the frequency domain and quantized yielding a broad-band virtual photon pulse. Double ionization in a TS-2 like mechanism is then described by the absorption of two virtual photons, one by each of the electrons and, accordingly, would depend sensitively on the correlated GS wave function. Indeed, different wave functions in the calculations resulted in considerably different correlated electron spectra.

Recently, electron correlations have been investigated by inspecting the so-called correlation function R (Schulz *et al* 2000a, 2001a, Gerchikov and Sheinermann 2001, Feuerstein *et al* 2001a, Gerchikov *et al* 2002). Here, the probability of finding two electrons emitted in the same multiple ionization event with a certain momentum difference is compared to the corresponding probability of two independent electrons being emitted in two different collisions. It was demonstrated that the correlation function is neither sensitive to the respective mechanism leading to double ionization (first-order or TS-2) nor to the final-state PCI with the projectile, possibly making R an ideal tool to investigate GS properties of the correlated wave function. This was substantiated by Gerchikov and Sheinermann (2001) who analysed the correlation function R_C for back-to-back emission of electrons with equal energy. It was found, in qualitative agreement with experiment, that the maximum in R_C is very sensitive to the mean initial-state separation between the two electrons and, moreover, its shape strongly depends on the correlated initial-state used in the calculation (see figure 48).

4.4.4.3. Multiple ionization at large perturbations. Up to now, only one kinematically complete experiment on multiple ionization has been performed for $3.6\,\mathrm{MeV\,u^{-1}}$ Au^{53+} impact on neon (Schulz *et al* 2000). For a large number of total, single and doubly differential cross section measurements see the previous reviews (Ullrich *et al* 1994, 1997, Dörner *et al* 2000). In figure 49, the momentum vectors of Ne^{3+} recoil-ions are plotted along with the vector sum-momentum of all three emitted electrons. The collision plane is defined as in figure 39. Not even an attempt has been made up to now to describe the complete five-particle dynamics in a strongly non-perturbative situation within a quantum-mechanical theory. However, classical nCTMC results are at hand for comparison, displayed in the right panel of the figure.

Surprisingly, even for triple ionization the authors found the typical features observed before for single and double electron emission in the non-perturbative regime, namely little net-momentum transfer at considerable energy deposition. As calculations indicate (Kirchner

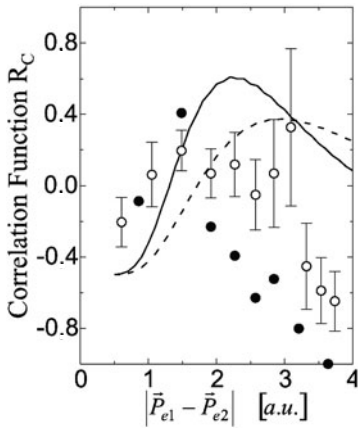

Figure 48. Correlation function R_C for double ionization of He (○) and Ne (●) in collisions with 3.6 MeV u^{-1} Au^{53+} ($v_P = 12$ a.u.) as a function of the electron momentum difference $\Delta P = |\vec{P}_{e1} - \vec{P}_{e2}|$ for back-to-back emitted electrons. ——: correlated 16-term wave function for the He GS. - - - -: 3-term multi-configuration Hartree–Fock wave function (Gerchikov *et al* 2002).

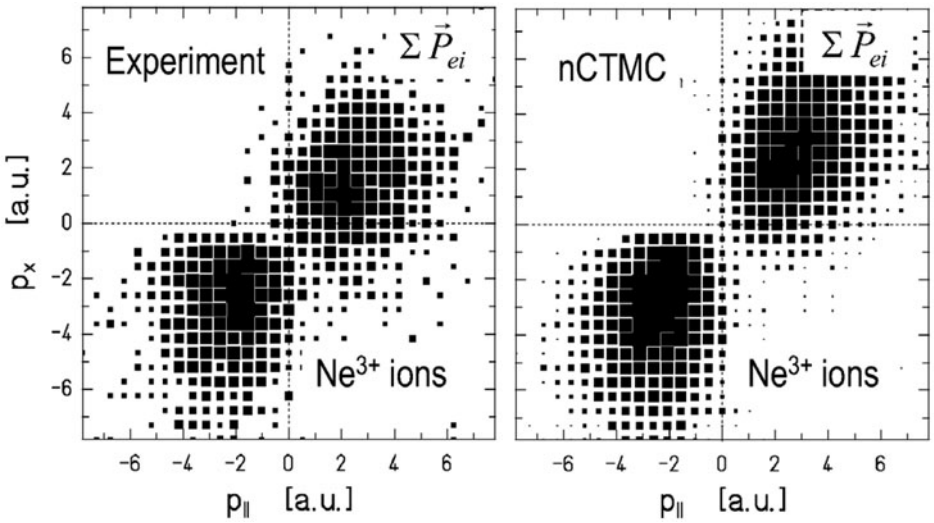

Figure 49. Two-dimensional final state momentum distributions for the Ne^{3+} recoil-ions and the sum-momentum vector of all three emitted electrons for triple ionization of Ne by 3.6 MeV u^{-1} Au^{53+} impact. The collision plane is defined as in figure 39. Left: experiment. Right: nCTMC. Z-scale is logarithmic (Schulz *et al* 2000).

et al 2002a), even for triple ionization the most likely impact parameters are larger than 3 a.u., well outside the target electron cloud again causing a kind of dissociation of the atom in the field. As before, a strong PCI effect was observed, dragging each of the electrons behind but, at the same time, pushing away the Ne^{3+} ions with similar momenta. Implying that all the electrons experience about the same PC force, the authors tried to separate the influence of the PCI from the (correlated) relative motion of the three electrons by a transformation into the three-electron CM co-ordinate frame, where PCI should not be present at all under the given assumptions.

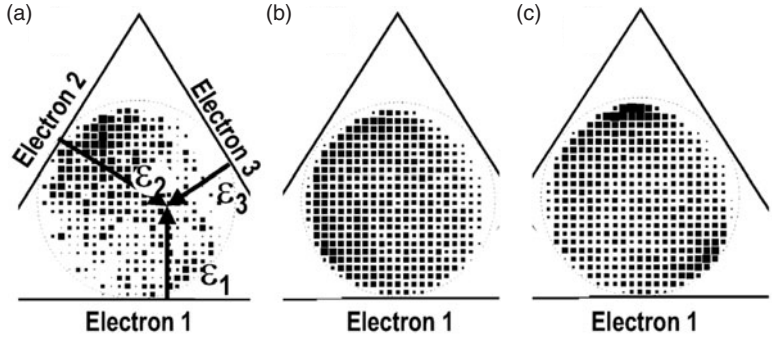

Figure 50. Dalitz-representation (see text) of the energy partitioning of three electrons emitted in triply ionizing 3.6 MeV u^{-1} Au^{53+} on Ne collisions in the electron CM co-ordinate system. ε_i: relative energy of the ith electron in the CM system. Electrons are numbered according to their emission angle with respect to the projectile direction (see text). Left: experiment; middle: nCTMC without electron–electron interaction; right: nCTMC with fully correlated three-electron initial-state (Schulz *et al* 2000).

In figure 50, the relative energies of the three electrons $\varepsilon_{ei} = E_i^{\mathrm{CM}} / \sum E_i^{\mathrm{CM}}$ in the CM system (E_i^{CM}: CM energy of the ith electron) were presented in a modified Dalitz-plot (Dalitz 1953). This is an equilateral triangle where each triple ionization event is represented by one point inside the triangle with its distance from each individual side being proportional to the relative energy of the corresponding electron as indicated in the figure. Only events in the inscribed circle are allowed due to momentum conservation in the CM frame ($\sum \vec{P}_{ei}^{\mathrm{CM}} = 0$). Electrons are numbered such that electron 1 is the one with the smallest angle relative to the projectile propagation direction in each triple ionization event and electron 3 the one with the largest angle.

Obviously, the electron energies are not independent of each other and the many-electron continuum, explored for the first time experimentally, was found to be strongly correlated. There is an increased probability that electrons 1 and 3 have large energies compared to electron two. nCTMC calculations without inclusion of the electron–electron interaction beyond an effective potential in the initial state were not able to reproduce these structures (figure 50(*b*)). Considering the final state interaction between the electrons in a similar way to Moshammer *et al* (1996), led to structures in the Dalitz plot but essentially with the role of electron 'two' and 'three' exchanged. Introducing in addition a completely correlated, three-electron (P-electrons neglecting the spin) classical initial state, where the individual electrons move on Kepler ellipses at equal distances relative to each other on the corners of an equilateral triangle in a plane, with the electron–electron interaction 'switched on' during the entire collision, brought the theoretical results surprisingly close to the experimental data (figure 50(*c*)).

Differential energy loss spectra of the projectile were reported for the same collision system for single to six-fold ionization (Schulz *et al* 1999) surpassing previously achieved resolutions (Schöne *et al* 1995, Schuch *et al* 1988) by an order of magnitude through monitoring all target reaction products up to triple ionization. It was shown, that an 'average electron model', where the energy distribution of a 'typical' electron emitted in an n-fold ionization event was n-times convoluted with itself in order to simulate the total energy loss, was in excellent agreement with the directly measured data for up to triple ionization. Thus, electron spectra measured in coincidence with n-times charged recoil-ions were used to extract absolute energy loss distributions for up to six-fold ionization and reasonable agreement with nCTMC calculations

was observed. Finally, a technique was suggested, to determine the contribution of target excitation to the total energy loss.

4.4.5. A short summary. Essentially within the last five years, momentum spectroscopy of ions and electrons has boosted traditional ion–atom collision physics in a remarkable way. The Q-value resolution in electron capture reactions at low collision velocities has reached a precision in the energy level determination competing with the most accurate spectroscopic techniques and further improvements are expected. Electron capture at high velocities has been explored, partly in a storage ring, giving unique information on second order 'Thomas' contributions. Electron impact ionization of ions has been observed for the first time in fully differential measurements by exploiting inverse kinematics and an event-by-event identification of the (e–e) contribution to projectile ionization in fast ion–atom collisions. Unprecedented impact-parameter dependent ultra-low energy electron spectra have been recorded in slow ion–atom collisions visualizing quasi-molecular orbitals formed during the collision and helping to clarify a long standing debate on 'SP electrons'. Relativistic collisions with light targets started to be explored and relativistic effects have been observed. Three-dimensional imaging of emitted electrons in kinematically complete experiments on single ionization in the perturbative regime revealed surprises for the fundamental three-particle Coulomb system that have never been observed before in three decades of (e,2e) research on electron impact, challenging theory considerably. Non-perturbative situations at large velocities became accessible for swift highly charged ion impact delivering benchmark data for the comparison with the most sophisticated non-perturbative theories. The long-discussed difference in the ratio of double to single ionization cross sections by projectiles with charges of different sign has started to be studied in terms of FDCSs. Triple ionization was explored in kinematically complete measurements observing correlations in the three-electron continuum, the correlation function has been investigated for double as well as triple ionization and energy loss measurements for multiply ionizing ion–atom collisions were reported for up to six-fold ionization on the basis of single collision experiments.

5. A view into the future

Rapid progress in the near future can be expected in all the fields described in this paper and this was partly envisaged at the end of each section. Especially in laser physics, however, where only three groups world-wide have made use of reaction-microscopes until now, a large number of novel investigations might become feasible. Among them are differential (see, e.g. Hasegawa *et al* (2001), Yamanouchi (2002)) kinematically complete measurements on molecules (the first one has been reported recently by Rottke *et al* (2002), see also Staudte *et al* (2002), Alnaser *et al* (2003)), on state-prepared molecular ions or experiments allowing us to extract FDCSs as routinely done for photon, electron or ion impact. Furthermore, investigations using extremely short laser pulses, with two or three optical cycles only (see, e.g. Morgner *et al* (2001)) and fixed phase within the envelope (Baltuska *et al* 2003) or with attosecond higher-harmonic pulses (Drescher *et al* 2001), will certainly be performed. Moreover, pulses will be actively shaped or sequences of pulses will be applied in the future (see, e.g. Wollenhaupt *et al* (2002)) in order to coherently control the electron dynamics so that certain reactions in atoms, molecules or clusters will be either enhanced or suppressed.

A major step forward will be the advent of tuneable high-intensity short-pulse VUV or even x-ray self-amplifying (SASE) free-electron lasers (FEL). Such a machine has been demonstrated recently and first experiments on the fragmentation of clusters have been

performed (Wabnitz *et al* 2002). At the TESLA-Test Facility in Hamburg 150 fs, 10^{17} W cm^{-2} pulses will be available in 2004 at photon energies between 20 and 200 eV, at a bandwidth of 10^{-4}, 70 kHz repetition rate and, if demanded, synchronized with a conventional high-intensity fs Ti : Sa laser. Unique experiments will become feasible with this machine on the non-linear interaction of coherent high-energy light with ions, atoms, molecules, molecular ions, clusters and surfaces. Some of the schemes (Ullrich *et al* 2003a), making use of the optical laser phase synchronized with the FEL pulse, envisage monitoring the time-evolution of correlated atomic and molecular electronic processes on an attosecond timescale, applying methods that have recently been used to characterize attosecond pulses (Drescher *et al* 2002).

Moreover, for ion impact, the first kinematically complete experiments on multiple ionization at high energies, up to 500 MeV u^{-1}, and for projectile charge states between about 30+ and 92+, i.e. at large perturbations Z_P/v_p, will soon be feasible in the experimental storage ring ESR of GSI in Darmstadt. Up to now, only one recoil-ion momentum spectrometer has been implemented into a storage ring, the Stockholm CRYRING. At GSI a reaction-microscope has been developed and will become operational in 2003. Due to the strongly increased luminosity in the ring as compared to single pass experiments we expect considerable, orders-of-magnitude, increased event-rates, so that FDCSs should become measurable for double, triple and even quadruple ionization in attosecond fields.

With the adaptation of the concepts of reaction-microscopes to the imaging of electrons (Moshammer and Ullrich 1998, Hattas *et al* 2003) and ions (Moshammer *et al* 1990, Jalowy *et al* 2002, 2002a, b, 2003, 2003a) emitted from surfaces this successful technique has just entered the field of solid state and surface physics. Here, a similar stormy progress to the one in atomic and molecular physics can be expected for the future. One promising route is to investigate the correlated emission of electrons from solids by single photon, laser or ion impact, analogous to the experiments described in this paper for atomic targets.

The tools described here are ideally suited for the investigation of the orientation dependence and the reaction-pathways of slow molecule–atom collisions. First exploratory experiments (Wu *et al* 1995) have already shown that this technology has the potential to provide substantial contributions to reaction stereochemistry.

Laser-assisted collisions, that have been theoretically explored for a while (see Ehlotsky *et al* (1998) for a recent review and references in section 4.3) will certainly be an upcoming field after the first feasibility demonstration in electron–atom collisions (see section 4.3) using a reaction-microscope along with an intense, ns-pulsed Yag laser. Until now, such studies were only accessible experimentally for elastic and resonant scattering. Unexpectedly, strong coupling of an even weak ($E_0 = 0.005$ a.u.), low-frequency ($\omega_0 = 0.004$ a.u.) electromagnetic radiation field to matter has been recently predicted in laser-assisted collisions, considering a direct encounter of a fast ($v_P = 12$ a.u.) proton with a target electron, so-called BEE (Voitkiv and Ullrich 2001a, b). Although the laser field used in the calculation was far from strong enough to noticeably disturb the hydrogen target-atom GS alone, strong effects occur during the collision in the high-energy BEE emission. Thousands of laser-photons were observed to couple to the system, strongly modifying the energy and angular distribution of the BEE. Moreover, electron transfer reactions in slow ion–atom collisions were calculated to be considerably affected by a laser-field, possibly opening the door for ultra-fast control of electronic motion within one optical half-cycle (Kirchner 2002).

Another interesting situation arises, and might be realized with the PHELIX laser at GSI (PHELIX 2001), if both attosecond ion-induced fields and femtosecond strong laser fields act together. The ion-induced pulse efficiently brings a large number of electrons into the continuum, placing them 'simultaneously', with little energy, into the oscillating field of the laser, which then accelerates this bunch of electrons very effectively in a coherent way, heating

them tremendously. Thus, one might envisage, that the most effective way to transfer energy to matter might be a concerted action between ion-induced and laser fields.

Acknowledgments

We gratefully acknowledge support from the Max-Planck-Society, from the Deutsche Forschungsgemeinschaft DFG within the Leibniz-Programme and several separate proposals, from the Bundesministerium für Forschung und Technologie BMFT, from the Deutscher Akademischer Austauschdienst DAAD and from GSI. Last but not least, we would like to thank numerous students, who have contributed over the years, many colleagues for stimulating discussions and exciting new experimental ideas.

References

Abdallah M, Kravis C D, Cocke C L, Wang Y, Rodriguez V D and Stöckli M 1997 *Phys. Rev.* A **56** 2000
Abdallah M, Cocke C L, Wolff W, Wolf H, Kravis C D, Stöckli M and Kamber E 1998 *Phys. Rev. Lett.* **81** 3627
Abdallah M, Wolff W, Wolff H E, Kamber E Y, Stöckli M and Cocke C L 1998a *Phys. Rev.* A **58** 2911
Abdallah M, Wolff W, Wolff H E, Cocke C L and Stöckli M 1998b *Phys. Rev.* A **58** 3379
Abdallah M, Wolff W, Wolff H E, Cocke C L and Stöckli M 1999 *J. Phys.* B **32** 4237
Achler M, Mergel V, Spielberger L, Azuma Y, Dörner R and Schmidt Böcking H 2001 *J. Phys.* B **34** L965
Adoui L, Caraby C, Cassimi A, Lelièvre D, Grandin J P and Dubois A 1999 *J. Phys.* B **32** 631
Adoui L *et al* 2001 *Phys. Scr.* T **92** 89
Afaneh F, Dörner R, Schmidt L, Weber Th, Stiebing K E, Jagutzki O and Schmidt-Böcking H 2002 *J. Phys.* B **35** L229
Ali R, Frohne V, Cocke C L, Stöckli M, Cheng S and Raphaelian L A 1992 *Phys. Rev. Lett.* **69** 2491
Ali I, DuBois R D, Cocke C L, Hagmann S, Feeler C R and Olson R E 2001 *Phys. Rev.* A **64** 022712
Alnaser A S, Osipov P, Benis E P, Wech A, Cocke C L, Tong X M and Lin C D 2003 *Phys. Rev. Lett.* submitted
Avaldi L, Camilloni R, Multari R, Stefani G, Robaux O, Tweed R J and Vien G N 1998 *J. Phys.* B **31** 2981
Balashov V V and Bodrenko I V 1999 *J. Phys.* B **32** L687
Balashov V V and Bodrenko I V 2000 *J. Phys.* B **33** 1473 (corrigendum)
Baltuska A *et al* 2003 *Nature* **421** 611
Bandarage G and Parson R 1990 *Phys. Rev.* A **41** 5878
Bapat B *et al* 1999 *J. Phys.* B **32** 1859
Bapat B, Keller S, Moshammer R, Mann R and Ullrich J 2000 *J. Phys.* B **33** 1437
Bastos de Jesus V *et al* 2003 *Phys. Rev. Lett.* submitted
Bates D R and Griffing G 1953 *Phys. Soc.* A **66** 961
Bates D R and Griffing G 1954 *Phys. Soc.* A **67** 663
Bates D R and Griffing G 1955 *Phys. Soc.* A **68** 90
Becker A and Faisal F H M 2000 *Phys. Rev. Lett.* **84** 3546
Becker A and Faisal F H M 2002 *Phys. Rev. Lett.* **89** 193003
Bethe H 1930 *Ann. Phys. Lpz.* **5** 325
Berakdar J and Klar H 1992 *Phys. Rev. Lett.* **69** 1175
Berakdar J, Klar H, Huetz A and Selles P 1993 *J. Phys.* B **26** 1463
Berakdar J 1998 *J. Phys.* B **31** 3167
Berakdar J 1999 *J. Phys.* B **32** L25
Berakdar J and Klar H 2001 *Phys. Rep.* **340** 474
Bernardi G C, Suárez S, Fainstein P D, Garibotti C R, Meckbach W and Focke P 1989 *Phys. Rev.* A **40** 6863
Bernardi G, Fainstein P, Garibotti C R and Suarez S 1990 *J. Phys.* B **23** L139
Brabec T and Krausz F 2000 *Rev. Mod. Phys.* **72** 545
Bray I 2002 *Phys. Rev. Lett.* **89** 273201-1
Bräuning H P *et al* 1997 *J. Phys.* B **30** L649
Bräuning H P *et al* 1998 *J. Phys.* B **31** 5149
Briggs J S and Schmidt V 2000 *J. Phys.* B **33** R1
Bronk T, Reading J F and Ford A L 1998 *J. Phys.* B **31** 2477
Buchet-Poulizak M-C, Bogdanovich P O and Knystautas É 2001 *J. Phys.* B **34** 233
Chassid M and Horbatsch M 2002 *Phys. Rev.* A **66** 12714

Cassimi A, Duponchel S, Flechard X, Jardin P, Sortais P, Hennecart D and Olson R E 1996 *Phys. Rev. Lett.* **76** 3697
Chen J *et al* 2000 *Phys. Rev.* **63** 011404R
Chen J and Nam C H 2002 *Phys. Rev.* A **66** 053415
Cherepkov N A, Raseev G, Adachi J, Hikosaka Y, Ito K, Motoki S, Sano M, Soejima K and Yagishita A 2000 *J. Phys.* **33** 4213
Cherepkov N A, Semenov S K, Hikosaka Y, Ito K, Motoki S and Yagishita A 2000a *Phys. Rev. Lett.* **84** 250
Cocke C L and Olson R E 1991 *Phys. Rep.* **205** 155
Choi H C, Rao R M, Mihill A G, Kakar S, Poliakoff E D, Wang K and McKoy V 1994 *Phys. Rev. Lett.* **72** 44
Colgan J, Pindzola M S and Robicheaux F 2001 *J. Phys.* **34** L457
Colgan J and Pindzola M S 2002 *Phys. Rev.* A **65** 032729
Collins S A *et al* 2002 *Phys. Rev.* A **65** 052717
Coplan M A *et al* 1994 *Rev. Mod. Phys.* **66** 985
Corkum B P, Burnett N H and Brunel F 1989 *Phys. Rev. Lett.* **62** 1259
Corkum P 1993 *Phys. Rev. Lett.* **71** 1994
Crothers D S F and McCann J F 1983 *J. Phys.* B **16** 3229
Dalitz R H 1953 *Phil. Mag.* **44** 1068
Davies J A, Continetti R E, Chandler D W and Hayden C C 2000 *Phys. Rev. Lett.* **84** 5983
De Fanis A *et al* 2002 *Phys. Rev. Lett.* **88** 073002
DeHaven W R, Dilley C, Landers A, Kamber E Y and Cocke C L 1998 *Phys. Rev.* A **57** 292
Dehmer J L and Dill D 1976 *J. Chem. Phys.* **65** 5327
Dill D 1976 *J. Chem. Phys.* **65** 1130
Dill D, Swanson J R, Wallace S and Dehmer J L 1980 *Phys. Rev. Lett.* **45** 1393
Delone N B and Krainov V P 1991 *J. Opt. Soc. Am.* B **8** 1207
Delone N B and Krainov V P 1998 *Phys. Usp.* **41** 469
Dietrich P *et al* 1994 *Phys. Rev.* A **50** R3585
DiMauro L and Agostini P 1995 *Advances in Atomic and Molecular Physics* (New York: Academic)
Dogan M and Crowe A 2002 *J. Phys.* B **35** 2773
Dorn A, Moshammer R, Schröter C S, Zouros T J M, Schmitt W, Kollmus H, Mann R and Ullrich J 1999 *Phys. Rev. Lett.* **82** 2496
Dorn A, Kheifets A, Schröter C D, Najjari B, Höhr C, Moshammer R and Ullrich J 2001 *Phys. Rev. Lett.* **86** 3755
Dorn A, Kheifets A, Schröter C D, Najjari B, Höhr C, Moshammer R and Ullrich J 2002 *Phys. Rev.* A **65** 2709
Dorn A, Sakhelashvili G, Höhr C, Kheifets A, Lower J, Najjari B, Schröter C D, Moshammer R and Ullrich J 2002a *Electron and Photon Impact Ionisation and Related Topics 2002: Proc. International Conf. on Electron and Photon Impact Ionisation and Related Topics (Metz, France, 18–20 July 2002)* ed L U Ancarani (Bristol: Institute of Physics Publishing)
Dorn A, Kheifets A, Schröter C D, Höhr C, Sakhelashvili G, Moshammer R, Lower J and Ullrich J 2003 *Phys. Rev.* A at press
Dörner R *et al* 1994 *Phys. Rev. Lett.* **72** 3166
Dörner R, Mergel V, Zhaoyuan L, Ullrich J, Spielberger L, Olson R E and Schmidt-Böcking H 1995 *J. Phys.* B **28** 435
Dörner R *et al* 1996 *Phys. Rev. Lett.* **76** 2654
Dörner R, Khemliche H, Prior M H, Cocke C L, Gary J A, Olson R E, Mergel V, Ullrich J and Schmidt-Böcking H 1996a *Phys. Rev. Lett.* **77** 4520
Dörner R *et al* 1996b *Phys. Rev. Lett.* **77** 1024
Dörner R *et al* 1997 *Phys. Rev. Lett.* **78** 2031 (erratum)
Dörner R *et al* 1997 *Nucl. Instrum. Methods* B **124** 225
Dörner R *et al* 1998 *Phys. Rev.* A **57** 1074
Dörner R *et al* 1998a *Phys. Rev. Lett.* **81** 5776
Dörner R *et al* 1998b Atomic processes in plasmas *AIP Conf. Proc.* vol 443, ed E Oks and M Pindzola
Dörner R, Mergel V, Jagutzki O, Spielberger L, Ullrich J, Moshammer R and Schmidt-Böcking H 2000 *Phys. Rep.* **330** 95
Dörner R, Weber Th, Weckenbrock M, Staudte A, Hattass M, Schmidt-Böcking H, Moshammer R and Ullrich J 2002 *Adv. At. Mol. Opt. Phys.* **48** 1
Drescher M *et al* 2001 *Science* **291** 1923
Drescher M *et al* 2002 *Nature* **419** 803
DuBois R D, Ali I, Cocke C L, Feeler C R and Olson R E 2000 *Phys. Rev.* A **62** 060701
Dupré C, Lahmam-Bennani A, Duguet A, Mota-Furtado F, O'Mahony P F and Capello C D 1992 *J. Phys.* B **25** 259
Edgü-Fry E, Cocke C L, Sidky E, Lin C D and Abdallah M 2002 *J. Phys.* B **35** 2603
Ehrhardt H, Schulz M, Tekaat T and Willmann K 1969 *Phys. Rev. Lett.* **22** 89
Ehlotsky F, Jaron A and Kaminski J Z 1998 *Phys. Rep.* **297** 6

Eichmann U *et al* 2000 *Phys. Rev. Lett.* **84** 3550
Eremina E *et al* 2003 *J. Phys.* B **36** 3269
Fainstein P D, Ponce V H and Rivarola R D 1988 *J. Phys.* B **21** 287
Fainstein P, Gulyás L, Martín F and Salin A 1996 *Phys. Rev.* A **53** 3243
Fainstein P D, Moshammer R and Ullrich J 2001 *Phys. Rev.* A **63** 062720
Faisal F H M 1973 *J. Phys.* B **6** L89
Feagin J M and Briggs J S 1986 *Phys. Rev. Lett.* **57** 984
Feagin J M 1995 *J. Phys.* B **28** 1495
Feagin J M 1996 *J. Phys.* B **29** l551
Feagin J M 1998 *J. Phys.* B **31** L729
Feeler C R and Olson R E 2000 *J. Phys.* B **33** 1997
Feeler C R, Olson R E, DuBois R D, Schlathölter T, Hadjar O, Hoekstra R and Morgenstern R 1999 *Phys. Rev.* A **60** 2112
Feuerstein B, Moshammer R and Ullrich J 2000 *J. Phys.* B **33** L823
Feuerstein B *et al* 2001 *Phys. Rev. Lett.* **87** 043003
Feuerstein B, Schulz M, Moshammer R and Ullrich J 2001a *Phys. Scr.* T **92** 447
Fiol J, Olson R E, Santos A C F, Sigaud G M and Montenegro E C 2001 *J. Phys.* B **34** L503
Fischer D, Feuerstein B, Dubois R D, Moshammer R, Crespo López-Urrutia J R, Draganic I, Lörch H, Perumal A N and Ullrich J 2002 *J. Phys.* B **35** 1369
Fischer D *et al* 2003 *Phys. Rev. Lett.* **90** 243201-1
Fischer D, Moshammer R, Schulz M, Voitkiv A, Madison D H, Foster M and Ullrich J 2003a *J. Phys.* B submitted
Fischer D, Voitkiv A B, Moshammer R and Ullrich J 2003 *Phys. Rev.* A at press
Flechard X, Nguyen H, Wells E, Ben-Itzhak I and DePaola B D 2001 *Phys. Rev. Lett.* **87** 123203
Flechard X, Harel C, Jouin H, Pons B, Adoui L, Fremont F, Cassimi A and Hennecart D 2001a *J. Phys.* B **34** 2759
Fittinghoff D N *et al* 1992 *Phys. Rev. Lett.* **69** 2642
Fittinghoff D N *et al* 1994 *Phys. Rev.* A **49** 2174
Ford A L and Reading J F 1988 *J. Phys.* B **21** L685
Ford A L and Reading J F 1990 *J. Phys.* B **23** 2567
Frémont F *et al* 2002 *Int. J. Mol. Sci.* **3** 115
Fritsch W 1994 *J. Phys.* B **27** 3461
Gay T J, Gealy M W and Rudd M E 1990 *J. Phys.* B **23** L823
Gensmantel A, Ullrich J, Dörner R, Olson R E, Ullmann K, Forberich E, Lencinas S and Schmidt-Böcking H 1992 *Phys. Rev.* A **45** 4572
Gerchikov L G and Sheinermann S A 2001 *J. Phys.* B **34** 647
Gerchikov L G, Sheinermann S A, Schulz M, Moshammer R and Ullrich J 2002 *J. Phys.* B **35** 2783
Gessner O, Hikosaka Y, Zimmermann B, Hempelmann A, Lucchese R, Eland J, Guyon P and Becker U 2002 *Phys. Rev.* **88** 193002
Golovin A V, Heiser F, Quayle C J K, Morin P, Simon M, Gessner O, Guyon P M and Becker U 1997 *Phys. Rev. Lett.* **79** 4554
Goreslavskii S and Popruzhenko S 2001 *Opt. Express* **8** 395
Grin M, Dal Cappello C, Mkhanter R El and Rasch J 2000 *J. Phys.* B **33** 131
Guillemin R, Shigemasa E, Le Guen K, Ceolin D, Miron C, Leclercq N, Morin P and Simon M 2001 *Phys. Rev. Lett.* **87** 203001
Gulyás L, Kirchner T, Shirai T and Horbatsch M 2000 *Phys. Rev.* A **62** 022702
Hasan A A, Emmons E D, Hinojosa G and Ali R 1999 *Phys. Rev. Lett.* **83** 4522
Hasegawa H, Hishikawa A and Yamanouchi K 2001 *Chem. Phys. Lett.* **349** 57
Hattass M 2003 Private communication
Hayes P A and Williams J F 1996 *Phys. Rev. Lett.* **77** 3098
Heiser F, Gessner O, Viefhaus J, Wieliczec K, Hentges R and Becker U 1997 *Phys. Rev. Lett.* **79** 2435
Helm H, Bjerre N, Dyer M J, Huestis D L and Saeed M 1993 *Phys. Rev. Lett.* **70** 3221
Hikosaka Y and Eland J 2000 *J. Phys.* B **33** 3137
Hikosaka Y and Eland J 2000a *Chem. Phys.* **20** 4663
Hikosaka Y, Eland J, Watson T and Powis I 2001 *J. Chem. Phys.* **115** 4593
Hikosaka Y and Eland J 2002 *Chem. Phys.* **277** 53
Hippler R, Datz S, Miller P D, Pepmiller P L and Dittner P F 1987 *Phys. Rev.* A **35** 585
Huetz A, Selles P, Waymel D and Mazeau J 1991 *J. Phys.* B **24** 1917
Huetz A and Mazeau J 2000 *Phys. Rev. Lett.* **85** 530
Illescas C, Rabadán L and Riera A 1998 *Phys. Rev.* A **57** 1809

Irby V D, Gay T J, Edwards J Wm, Hale E B, McKenzie M L and Olson R E 1988 *Rev.* A **37** 3612
Ito K, Adachi J, Hall R, Motoki S, Shigemasa E, Soejima K and Yagishita A 2000 *J. Phys.* **33** 572
Ito K, Adachi J, Hikosaka Y, Motoki S, Soejima K, Yagishita A, Raseev G and Cherepkov N A 2000a *Phys. Rev. Lett.* **85** 46
Jagutzki O, Spielberger L, Dörner R, Nüttgens S, Mergel V, Schmidt-Böcking H, Ullrich J, Olson R E and Buck U 1996 *Z. Phys.* D **36** 5
Jagutzki O, Mergel V, Ullmann-Pfleger K, Spielberger L, Meyer U, Dörner R and Schmidt-Böcking H 1998 *Imaging Spectroscopy IV, Proc. International Symp. on Optical Science Engineering and Instrumentation (Proc. SPIE)* vol 3438, ed M R Descour and S S Shen, pp 322–33
Jagutzki O *et al* 2002 *IEEE Trans. Nucl. Sci.* **49** 2477
Jagutzki O, Lapington J S, Worth L B C, Spillmann U, Mergel V and Schmidt-Böcking H 2002a *Nucl. Instrum. Methods Phys. Res.* A **477** 256
Jagutzki O, Mergel V, Ullmann-Pfleger K, Spielberger L, Spillmann U, Dörner R and Schmidt-Böcking H 2002b *Nucl. Instrum. Methods Phys. Res.* A **477** 244
Jahnke T *et al* 2002 *Phys. Rev. Lett.* **88** 073002
Jahnke T 2003 Private communication
Jalowy T, Neugebauer R, Hattass M, Fiol J, Afaneh F, Pereira J A M, Collado V, da Silveira E F, Schmidt-Böcking H and Groeneveld K O 2002 *Nucl. Instrum. Methods* B **193** 762
Jalowy T, Neugebauer R, Groeneveld K O, Ponciano C R, Farenzena L S and da Silveira E F 2002a *Int. J. Mass Spectrom.* **219** 343
Jalowy T, Neugebauer R, Groeneveld K O, Ponciano C R, Farenzena L S and da Silveira E F 2002b *Rev. Sci. Instrum.* **73** 3187
Jalowy T, Neugebauer R, Farenzena L S, Collado V M, Schmidt-Böcking H, da Silveira E F and Groeneveld K O 2003 *Proc. 17th CAARI Conf. (Denton, USA, 12–16 November 2002)* at press
Jalowy T, Weber Th, Dörner R, Farenzena L S, Collado V M, Schmidt-Böcking H, da Silveira E F and Groeneveld K O 2003a *Int. J. Mass Spectrom.* submitted
Jardin P, Cassimi A, Grandin J P, Rothard H, Lemoigne J P, Hennecart D, Husson X and Lepontre A 1996 *Nucl. Instrum. Methods* B **107** 41
Kamber E Y, Abdallah M A, Cocke C L, Stöckli M, Wang J and Hansen J P 2000 *J. Phys.* B **33** L171
Kazanski A K and Ostrovsky V N 1993 *Phys. Rev.* A **48** R871
Kazanski A K and Ostrovsky V N 1994 *J. Phys.* B **27** 447
Kazanski A K and Ostrovsky V N 1995 *Phys. Rev.* A **51** 3698
Keldysh L V 1964 *Zh. Eksp. Teor. Fiz.* **47** 1945
Keller S, Lüdde H J and Dreizler R M 1997 *Phys. Rev.* A **55** 4215
Keller S 2000 *J. Phys.* B **33** L513
Keller S, Bapat B, Moshammer R, Ullrich J and Dreizler R M 2000a *J. Phys.* B **33** 1447
Khalil D, Maquet A, Taïeb R, Joachain C J and Makhoute A 1997 *Phys. Rev.* A **56** 4918
Khayyat Kh *et al* 1999 *J. Phys.* B **32** L73
Kheifets A and Bray I 1998 *Phys. Rev. Lett.* **81** 4588
Kheifets A and Bray I 1998a *J. Phys.* B **31** L447
Kheifets A S *et al* 1999 *J. Phys.* B **32** 5047
Kheifets A, Bray I, Soejima K, Danjo A, Okuno K and Yagishita A 1999a *J. Phys.* B **32** L501
Kheifets A and Bray I 2000 *Phys. Rev.* A **62** 065402
Kheifets A 2003 Private communication
Kirchner T 2002 *Phys. Rev. Lett.* **89** 093203
Kirchner T, Gulyás L, Schulz M, Moshammer R and Ullrich J 2002a *Phys. Rev.* A **65** 042727
Knapp A *et al* 2002 *Phys. Rev. Lett.* **89** 033004
Knapp A *et al* 2002a *J. Phys.* B **35** L521
Kollmus H, Moshammer R, Olson R E, Hagmann S, Schulz M and Ullrich J 2002 *Phys. Rev. Lett.* **88** 103202-1
Kossmann H, Schwarzkopf O, Kämmerling B and Schmidt V 1989 *Phys. Rev. Lett.* **63** 2040
Krässig B, Dunford R W, Gemmell D S, Hasegawa S, Kanter E P, Schmidt-Böcking H, Schmitt W, Southworth S H, Weber Th and Young L 1999 *Phys. Rev. Lett.* **83** 53
Kravis S D *et al* 1996 *Phys. Rev.* A **54** 1394
Kuchiev M Y 1987 *Sov. Phys.-JET Lett.* **45** 404
Kuznetsov V V and Cherepkov N A 1996 *J. Electron Spectrosc. Relat. Phenom.* **79** 437
Lafosse A, Lebech M, Brenot J C, Guyon P M, Jagutzki O, Spielberger L, Vervloet M, Houver J C and Dowek D 2000 *Phys. Rev. Lett.* **84** 5987
Lafosse A, Brenot J C, Hoejrup K, Guyon P M, Houver J C, Lebech M and Dowek D 2001 *J. Chem. Phys.* **114** 6605

Lafosse A, Brenot J C, Guyon P M, Houver J C, Golovin A V, Lebech M, Dowek D, Lin P and Lucchese R R 2002 *J. Chem. Phys.* **117** 8368
Lahmam–Bennani A, Dupré C and Duguet A 1989 *Phys. Rev. Lett.* **63** 1582
Lahmam-Bennani A 1991 *J. Phys.* B **24** 2401
Lambropoulos P, Maragakis P and Zhang J 1998 *Phys. Rep.* **305** 203
Landers A L *et al* 2001 *Phys. Rev. Lett.* **87** 013002
Larochelle S, Talebpour A and Chin S L 1998 *J. Phys.* B **31** 1201
Lee D H, Zouros T J M, Sanders J M, Richard P, Anthony J M, Wang Y D and McGuire J H 1992 *Phys. Rev.* A **46** 1374
Lee T G, Nguyen H, Flechard X, DePaola B D and Lin C D 2002 *Phys. Rev.* A **66** 042701
Lein M, Gross E and Engel V 2000 *Phys. Rev. Lett.* **85** 4707
Lucey S P, Rasch J, Wheelan C T and Walters H R J 1998 *J. Phys.* B **31** 1237
Macek J and Ovchinnikov S Yu 1998 *Phys. Rev. Lett.* **80** 2298
Madison D, Schulz M, Jones S, Foster M, Moshammer R and Ullrich J 2002 *J. Phys.* B **35** 3297
Madison D H, Fischer D, Foster M, Schulz M, Moshammer R, Jones S and Ullrich J 2003 *Phys. Rev. Lett.* submitted
Makhoute A, Khalil D, Maquet A, Joachain C J and Taieb R 1999 *J. Phys.* B **32** 3255
Makhoute A, Khalil D, Zitane M and Bouzidi M 2002 *J. Phys.* B **35** 957
Malegat L, Selles P and Huetz A 1997 *J. Phys.* B **30** 251
Malegat L, Selles P and Kazansky A K 2000 *Phys. Rev. Lett.* **85** 21
Malegat L, Selles P and Kazansky A K 2002 *Phys. Rev.* A **65** 032711
Martin C, Jelinsky P, Lamton M, Malina R F and Anger H O 1981 *Rev. Sci. Instrum.* **52** 1067
Matthäus R, Moshammer R and Wien K 1991 *NATO ASI Ser.* B **269** 55
Matthäus R, Moshammer R, von Hayn G and Wien K 1993 *Int. J. Mass Spectrom. Ion. Process.* **126** 45
Maulbetsch F and Briggs J S 1995 *J. Phys.* B **28** 551
McCarthy I E and Weigold E 1991 *Rep. Prog. Phys.* **54** 789
McGuire J H, Stolterfoht N and Simony P R 1981 *Phys. Rev.* A **24** 97
McGuire J H, Berrah N, Bartlett R J, Samson J A R, Tanis J A, Cocke C L and Schlachter A S 1995 *J. Phys.* B **28** 913
McGuire J H 1997 Electron correlation dynamics in atomic collisions *Cambridge Monographs on Atomic, Molecular and Chemical Physics* (Cambridge: Cambridge University Press)
Meckbach W, Suárez S, Focke P and Bernardi G 1991 *J. Phys.* B **24** 3763
Mergel V *et al* 1995 *Phys. Rev. Lett.* **74** 2200
Mergel V *et al* 1997 *Phys. Rev. Lett.* **79** 387
Mergel V *et al* 1998 *Phys. Rev. Lett.* **80** 5301
Mergel V, Dörner R, Khayyat Kh, Achler M, Weber T, Jagutzki O, Lüdde H J, Cocke C L and Schmidt-Böcking H 2001 *Phys. Rev. Lett.* **86** 2257
Miller R 1998 *Atomic and Molecular Beam Methods* vol 14, ed G Scoles *et al* (New York: Oxford University Press)
Mkhanter R El and Dal Cappello C 1998 *J. Phys.* B **31** 301
Montenegro E C and Meyerhof W E 1992 *Phys. Rev.* A **46** 5506
Montenegro E C, Melo W S, Meyerhof W E and dePinho A G 1992 *Phys. Rev. Lett.* **69** 3033
Montenegro E C, Belkacem A, Spooner D W, Meyerhof W E and Shah M B 1993 *Phys. Rev.* A **47** 1045
Morgner U *et al* 2001 *Phys. Rev. Lett.* **86** 5462
Moshammer R, Matthäus R, Wien K and Bolbach G 1990 *Proc. 5th Int. Conf. on Ion Formation from Organic Solids (IFOS 5)* ed A Hedin (New York: Wiley) p 17
Moshammer R *et al* 1994 *Phys. Rev. Lett.* **73** 3371
Moshammer R, Unverzagt M, Schmitt W, Ullrich J and Schmidt-Böcking H 1996 *Nucl. Instrum. Methods* B **108** 425
Moshammer R, Ullrich J, Unverzagt M, Schmitt W, Jardin P, Olson R E, Dörner R, Mergel V and Schmidt-Böcking H 1996a *Nucl. Instrum. Methods* B **107** 62
Moshammer R *et al* 1996b *Phys. Rev. Lett.* **77** 1242
Moshammer R *et al* 1997 *Phys. Rev. Lett.* **79** 3621
Moshammer R, Ullrich J, Kollmus H, Schmitt W, Unverzagt M, Schmidt-Böcking H, Wood C J and Olson R E 1997a *Phys. Rev.* A **56** 1351
Moshammer R and Ullrich J 1998 *A Method and Device for Surface Analysis* German Patent No 19803146.7
Moshammer R, Fainstein P D, Schulz M, Schmitt W, Kollmus H, Mann R, Hagmann S and Ullrich J 1999 *Phys. Rev. Lett.* **83** 4721
Moshammer R *et al* 2000 *Phys. Rev. Lett.* **84** 447
Moshammer R, Perumal A, Schulz M, Rodríguez V D, Kollmus H, Mann R, Hagmann S and Ullrich J 2001 *Phys. Rev. Lett.* **87** 223201-1
Moshammer R *et al* 2002 *Phys. Rev.* A **65** 035401

Moshammer R *et al* 2003 *Phys. Rev.* A at press
Moshammer R *et al* 2003a *Phys. Rev. Lett.* at press
Moshammer R, Kollmus H and Fischer D 2003b *Many Particle Quantum Dynamics in Atomic Fragmentation* ed J Ullrich and S Shevelko (Berlin: Springer) at press
Motoki S, Adachi J, Ito K, Ishii K, Soejima K, Yagishita A, Semenov S K and Cherepkov N A 2002 *Phys. Rev. Lett.* **88** 063003
Muramatsu Y *et al* 2002 *Phys. Rev. Lett.* **88** 133002
Niehaus A 1986 *J. Phys.* B **19** 2925
Olson R E 1983 *Phys. Rev.* A **27** 1871
Olson R E 1986 *Phys. Rev.* A **33** 4397
Olson R E, Gay T J, Berry H G, Hale E B and Irby V D 1987 *Phys. Rev. Lett.* **59** 36
Olson R E, Ullrich J and Schmidt-Böcking H 1989 *Phys. Rev.* A **39** 5572
Olson R E, Feeler C R, Wood C J, Cocke C L, Dörner R, Mergel V and Schmidt-Böcking H 1997 *Nucl. Instrum. Methods* B **124** 249
Olson R E, Wood C J, Schmidt-Böcking H, Moshammer R and Ullrich J 1998 *Phys. Rev.* A **58** 270
Olson R E and Fiol J 2001 *J. Phys.* B **34** L625
Olson R E, Fiol J, Moshammer R and Ullrich J 2003 *J. Phys.* B **36** L99
Olson R E and Fiol J 2003 *J. Phys.* B submitted (private communication)
O'Rourke S F C, Moshammer R and Ullrich J 1997 *J. Phys.* B **30** 5281
Osipov T, Cocke C L, Prior M H, Weber T, Jagutzki O, Schmidt L, Schmidt Böcking H, Dörner R and Landers A 2003 *Phys. Rev. Lett.* submitted
Ovchinnikov S Yu and Macek J H 1995 *Phys. Rev. Lett.* **75** 2474
Parker J S *et al* 2001 *J. Phys.* B **34** L691
Pavlychev A A, Fominykh N G, Watanabe N, Soejima K, Shigemasa E and Yagishita A 1998 *Phys. Rev. Lett.* **81** 3623
PHELIX 2001 http://www-aix.gsi.de/∼phelix/
Pieksma M and Ovchinnikov S Yu 1991 *J. Phys.* B **24** 2699
Pieksma M and Ovchinnikov S Yu 1994 *J. Phys.* B **27** 4573
Pieksma M, Ovchinnikov S Y, van Eck J, Westerveld W B and Niehaus A 1994 *Phys. Rev. Lett.* **73** 46
Perumal A N, Moshammer R, Schulz M and Ullrich J 2002 *J. Phys.* B **35** 2133
Pont M and Shakeshaft R 1995 *Phys. Rev.* A **51** R2676
Pont M, Shakeshaft R, Maulbetsch F and Briggs J S 1996 *Phys. Rev.* A **53** 3671
Pont M and Shakeshaft R 1996a *Phys. Rev.* A **54** 1448
Poon H C and Tong S Y 1984 *Phys. Rev.* B **30** 6211
Protopapas M, Keitel C and Knight P 1997 *Phys. Rep.* **60** 389
Reddish T J, Wightman J P, MacDonald M A and Cvejanovic S 1997 *Phys. Rev. Lett.* **79** 2438
Reddish T J and Feagin J 1998 *J. Phys.* B **32** 2473
Reiss H R 1980 *Phys. Rev.* A **22** 1786
Reiss H R 1987 *J. Phys.* B **20** L79
Rescigno T N *et al* 1999 *Science* **286** 2474
Rottke H *et al* 2002 *Phys. Rev. Lett.* **89** 013001-1
Rudd M E, Kim Y-K, Madison D H and Gay T J 1992 *Rev. Mod. Phys.* **64** 441
Saito N *et al* 2003 *J. Phys.* B **36** L24
Samson J A R, He Z X, Bartlett R J and Sagurton M 1994 *Phys. Rev. Lett.* **72** 3329
Schmidt-Böcking H *et al* 2002 *AIP Conf. Proc.* vol 604, ed D H Madison and M Schulz, p 120
Schmidt-Böcking H, Dörner R and Ullrich J 2002a *Europhys. News* **6** 210
Schmidt-Böcking H *et al* 2003 *Europhys. Lett.* **62** 477
Schmidt-Böcking H, Mergel V, Dörner R, Schmidt L, Weber T, Weigold E and Kheifets A S 2003a *Many-Particle Quantum Dynamics in Atomic and Molecular Fragmentation* ed J Ullrich and V P Shevelko (Berlin: Springer) at press
Schmidt H T *et al* 2002 *Phys. Rev. Lett.* **89** 163201-1
Schmidt L 2000 *PhD Thesis* Johann-Wolfgang-Goethe Universität Frankfurt
Schmidt W, Moshammer R, O'Rourke F S C, Kollmus H, Sarkadi L, Mann R, Hagmann S, Olson R E and Ullrich J 1998 *Phys. Rev. Lett.* **81** 4337
Schöne H, Schuch R, Datz S, Schulz M, Dittner P F, Giese J P, Kessel Q C, Krause H F, Miller P D and Vane C R 1995 *Phys. Rev.* A **51** 324
Schwarzkopf O, Krässig B, Elmiger J and Schmidt V 1993 *Phys. Rev. Lett.* **70** 3008
Schwarzkopf O and Schmidt V 1995 *J. Phys.* B **28** 2847
Schuch R, Schöne H, Miller P D, Krause H F, Dittner P F, Datz S and Olson R E 1988 *Phys. Rev. Lett.* **60** 925

Schultz D R, Reinhold C O, Krstic P S and Strayer M R 2002 *Phys. Rev.* A **65** 52722
Schulz M, Moshammer R, Schmitt W, Kollmus H, Mann R, Hagmann S, Olson R E and Ullrich J 1999 *J. Phys.* B **32** L557
Schulz M, Moshammer R, Schmitt W, Kollmus H, Mann R, Hagmann S, Olson R E and Ullrich J 2000 *Phys. Rev.* A **61** 022703
Schulz M, Moshammer R, Schmitt W, Kollmus H, Feuerstein B, Mann R, Hagmann S and Ullrich J 2000a *Phys. Rev. Lett.* **84** 863
Schulz M *et al* 2001 *J. Phys.* B **34** L305
Schulz M, Moshammer R, Gerchikov L G, Sheinermann S A and Ullrich J 2001a *J. Phys.* B **34** L795
Schulz M, Moshammer R, Perumal A N and Ullrich J 2002 *J. Phys.* B **35** L161
Schulz M, Moshammer R, Fischer D, Kollmus H, Madison D H, Jones S and Ullrich J 2003 *Nature* **422** 48
Selles P, Malegat L and Kazansky A K 2002 *Phys. Rev.* A **65** 032711
Sheehy B *et al* 1998 *Phys. Rev.* A **58** 3942
Shigemasa E, Adachi J, Oura M and Yagishita A 1995 *Phys. Rev. Lett.* **74** 359
Shigemasa E, Adachi J, Soejima K, Watanabe N, Yagishita A and Cherepkov N A 1998 *Phys. Rev. Lett.* **80** 1622
Sidky E Y and Lin C D 1998 *J. Phys.* B **31** 2949
Sidky E Y and Lin C D 1999 *Phys. Rev.* A **60** 377
Sidky E Y, Illescas C and Lin C D 2000 *Phys. Rev. Lett.* **85** 1634
Sidky E Y and Lin C D 2001 *Phys. Rev.* A **65** 012711
Sidorovich V A and Nikolaev V S 1983 *J. Phys.* B **16** 3243
Sobottka S E and Williams M B 1988 *IEEE Trans. Nucl. Sci.* **35** 348
Soejima K, Danjo A, Okuno K and Yagishita A 1999 *Phys. Rev. Lett.* **83** 1546
Solov'ev E A 1986 *Sov. Phys. JETP* **63** 678
Spielberger L *et al* 1995 *Phys. Rev. Lett.* **74** 4615
Spielberger L *et al* 1996 *Phys. Rev. Lett.* **76** 4685
Spielberger L *et al* 1999 *Phys. Rev.* A **59** 371
Staudte A, Cocke C L, Prior M H, Belcacem A, Ray C, Chong H W, Glover T E, Schoenlein R W and Saalmann U 2002 *Phys. Rev.* A **65** 020703(R)
Stefani G, Avaldi L and Camilloni R 1990 *J. Phys.* B **23** L227
Stolterfoht N, Havener C C, Phaneuf R A, Swenson J K, Shafroth S M and Meyer F W 1986 *Phys. Rev. Lett.* **57** 74
Stolterfoht N, DuBois R D and Rivarola R D 1994 *Electron Emission in Heavy Ion–Atom Collisions* (Berlin: Springer)
Stolterfoht N *et al* 1999 *Phys. Rev.* A **59** 1262
Taouil I, Lahmam-Bennani A, Duguet A and Avaldi L 1998 *Phys. Rev. Lett.* **81** 4600
Tarisien M *et al* 2000 *J. Phys.* B **33** L11
Thomas L H 1927 *Proc. R. Soc.* A **114** 561
Teng Z J and Shakeshaft R 1994 *Phys. Rev.* A **49** 3597
Turkstra J W, Hoekstra R, Knoop S, Meyer D, Morgenstern R and Olson R E 2001 *Phys. Rev. Lett.* **87** 123202
Ueda K *et al* 2003 *Chem. Phys.* **289** 135
Ullrich J 1987 *PhD Thesis* Johann-Wolfgang-Goethe Universität Frankfurt
Ullrich J and Schmidt-Böcking H 1987 *Phys. Lett.* A **125** 193
Ullrich J, Horbatsch M, Dangendorf V, Kelbch S and Schmidt-Böcking H 1988 *J. Phys.* B **21** 611
Ullrich J, Schmidt-Böcking H and Kelbch C 1988a *Nucl. Instrum. Methods* A **268** 216
Ullrich J, Olson R E, Dörner R, Kelbch S, Berg H and Schmidt-Böcking H 1989 *J. Phys.* B **22** 627
Ullrich J *et al* 1993 *Phys. Rev. Lett.* **71** 1697
Ullrich J, Dörner R, Mergel V, Jagutzki O, Spielberger L and Schmidt-Böcking H 1994 *Comments At. Mol. Phys.* **30** 285
Ullrich J 1994 Habilitationsschrift, Universität Frankfurt *GSI Report* (1994)-08, ISSN 0171-4546
Ullrich J, Moshammer R, Unverzagt M, Schmitt W, Jardin P, Olson R E, Dörner R, Mergel V and Schmidt-Böcking H 1995 *Nucl. Instrum. Methods* B **98** 375
Ullrich J, Moshammer R, Dörner R, Jagutzki O, Mergel V, Schmidt-Böcking H and Spielberger L 1997 *J. Phys.* B **30** 2917 (Topical Review)
Ullrich J, Bapat B, Dorn A, Keller S, Kollmus H, Mann R, Moshammer R, Olson R E, Schmitt W and Schulz M 2000 *X-Ray and Inner Shell Processes* ed R W Dunford *et al* pp 403–17
Ullrich J and Voitkiv A 2002 *Strong Field Laser Physics* ed Th Brabec and H Kapteyn (Berlin: Springer) at press
Ullrich J and Shevelko S 2003 *Many Particle Quantum Dynamics in Atomic Fragmentation, Springer Series: Atomic, Optical and Plasma Physics* vol 35 ed Ullrich J and Shevelko S (Berlin: Springer)
Ullrich J, Dörner R, Moshammer R, Rottke H, Sandner W 2003a *Proc. 18th International Conf. on Atomic Physics* ed H R Sadeghpour *et al* (Singapore: World Scientific) p 219

Unverzagt M, Moshammer R, Schmitt W, Olson R E, Jardin P, Mergel V, Ullrich J and Schmidt-Böcking H 1996 *Phys. Rev. Lett.* **76** 1043
Van der Poel M, Nielsen C V, Gearba M A and Andersen N 2001 *Phys. Rev. Lett.* **87** 123201
Viefhaus J *et al* 1996 *Phys. Rev. Lett.* **77** 3975
Voitkiv A B 1996 *J. Phys.* B **29** 5433
Voitkiv A B, Grün N and Scheid W 1999 *J. Phys.* B **32** 3929
Voitkiv A B and Ullrich J 2001 *J. Phys.* B **34** 4513
Voitkiv A B and Ullrich J 2001a *J. Phys.* B **34** 1673
Voitkiv A B and Ullrich J 2001b *J. Phys.* B **34** 4383
Voitkiv A B, Najjari B, Moshammer R and Ullrich J 2002 *Phys. Rev.* A **65** 032707-1
Voitkiv A B, Najjari B, Moshammer R and Ullrich J 2002a *J. Phys.* B **65** 032707
Voitkiv A B, Najjari B and Ullrich J 2003 *Phys. Rev.* A submitted
Wabnitz H *et al* 2002 *Nature* **420** 482
Walker B *et al* 1996 *Phys. Rev. Lett.* **77** 5031
Walter M and Briggs J S 1999 *J. Phys.* B **32** 2487
Walter M and Briggs J S 2000 *Phys. Rev. Lett.* **85** 1630
Wannier G H 1953 *Phys. Rev.* **90** 817
Watanabe N, Adachi J, Soejima K, Shigemasa E and Yagishita A 1997 *Phys. Rev. Lett.* **78** 4910
Weber T 1998 *Diploma Thesis* Universität Frankfurt, unpublished http://hsbpc1.ikf.physik.uni-frankfurt.de/publications/files/ThorstenWeber-1999, 2nd Edition.pdf
Weber T *et al* 2000 *Phys. Rev. Lett.* **84** 443
Weber T, Weckenbrock M, Staudte A, Spielberger L, Jagutzki O, Mergel V, Urbasch G, Vollmer M, Giessen H and Dörner R 2000a *J. Phys.* B **33** L127
Weber T, Weckenbrock M, Staudte A, Spielberger L, Jagutzki O, Mergel V, Urbasch G, Vollmer M, Giessen H and Dörner R 2000b *Nature* **405** 658
Weber Th *et al* 2000c *J. Phys.* B **33** 3331
Weber Th *et al* 2001 *Phys. Rev. Lett.* **86** 224
Weber Th *et al* 2001a *J. Phys.* B **34** 3669
Weber Th *et al* 2001b *Opt. Express* **8** 368
Weber Th *et al* 2003 *Phys. Rev. Lett.* **90** 153003
Weber Th 2003 *PhD Thesis* Johann-Wolfgang-Goethe Universität Frankfurt
Weckenbrock M, Hattass M, Czasch A, Jagutzki O, Schmidt l, Weber T, Roskos H, Löffler H, Thomson M and Dörner R 2001 *J. Phys.* B **34** L449
Weckenbrock M, Becker A, Staudte A, Kammer S, Smolarski M, Bhardwaj V R, Rayner D, Villeneuve D M, Corkum P B and Dörner R 2003 *Phys. Rev. Lett.* submitted
Whelan C T, Allan R J, Walters H R J and Zhang X 1993 (e, $2e$) *& Related Processes* ed C T Whelan *et al* (Dordrecht: Kluwer) pp 1–32
Winter T G and Lin C D 1984 *Phys. Rev.* A **29** 3071
Wolf S and Helm H 2000 *Phys. Rev.* A **62** 043408
Wolff W, Ben-Itzhak I, Wolf H E, Cocke C L, Abdallah M A and Stöckli M 2002 *Phys. Rev.* A **65** 042710
Wollenhaupt M *et al* 2002 *Phys. Rev. Lett.* **89** 173001-1
Wood C J, Olson R E, Schmitt W, Moshammer R and Ullrich J 1997 *Phys. Rev.* A **56** 3746
Wood C J and Olson R E 1999 *Phys. Rev.* A **59** 1317
Wu W *et al* 1994 *Phys. Rev. Lett.* **72** 3170
Wu W, Wong K L, Cocke C L, Giese J P and Montenegro E C 1995 *Phys. Rev.* A **51** 3718
Yamanouchi K 2002 *Science* **295** 1659
Zähringer K, Meyer H D and Cerderbaum L S 1992 *Phys. Rev.* A **46** 5643
Zare R N 1972 *Mol. Photochem.* **4** 1
Zhang H, Fléchard X, Cassimi A, Adoui L, Cremer G, Frémont F and Hennecart D 2001 *Phys. Rev.* A **64** 012715
Zouros T J M 1996 *Comments At. Mol. Phys.* **32** 291